UNIVERSITÀ DEGLI STUDI DI MILANO
Facoltà di Scienze Matematiche Fisiche e Naturali
Dottorato di Ricerca in Scienze Chimiche, XXIV Ciclo

Reactions at surfaces: beyond the static surface approach in quantum dynamics

Tesi di Dottorato di Ricerca di
Matteo Bonfanti

Tutor: Prof. Gian Franco Tantardini
Co-tutor: Dott. Rocco Martinazzo
Prof. Geert-Jan Kroes

A.A. 2010-2011

Abstract

Thanks to the peculiar electronic properties of gas-solid interfaces, surfaces play an important role in many chemical processes. In my thesis, I considered few different reactions at surfaces and addressed the problem of their description by means of quantum dynamical methods. In particular, the focus of the work is on the inclusion of surface motion in the dynamical models. This problem is very challenging for state-of-art quantum methods, due to the unfavorable scaling with the number of degrees of freedom. To avoid this computational limit a variety of methods were adopted, ranging from a static approach in a low dimensional Time Dependent Wave Packet (TDWP) calculations to a full dynamical description of dissipation in the framework of Multi-Configuration Time-Dependent Hartree method (MCTDH).

I considered three different physical problems. The first one is the exothermic, collinearly-dominated Eley-Rideal H_2 formation on graphite. In particular, I focused on the importance of the model used to describe the graphitic substrate, in light of the marked discrepancies present in available literature results. To this end, I considered the collinear reaction and computed the Potential Energy Surface (PES) for a number of different graphitic surface models using Density Functional Theory (DFT) for different dynamical regimes. I performed quantum dynamics with wave-packet techniques down to the cold collision energies relevant for the chemistry of the interstellar medium. Results show that the reactivity at moderate-to-high collision energies sensitively depends on the shape of the PES in the entrance channel, which in turn is related to the adopted surface model. At low energies I ruled out the presence of any barrier to reaction, thereby highlighting the importance of quantum reflection in limiting the reaction efficiency.

In a second part of my work, I studied the effect of lattice displacement on the interaction of H_2 with the Cu(111) surface using the Specific Reaction Parameter (SRP) approach to DFT. I systematically investigated how the motion of the surface atoms affects some features of the PES, such as the dissociation barrier height and the barrier geometry corresponding to some representative reaction pathways, and the anisotropy of the potential at these geometries. This analysis allowed the identification of the surface degrees of freedom that are likely to be most relevant for H_2 dissociation. In particular, I found that the lattice coordinate displacements that have the largest effect on the H_2/Cu(111) DFT-SRP barrier heights and locations concern the motion of the 1^{st} layer and 2^{nd} layer Cu atoms in the Z direction, and motion of the 1^{st} layer atoms in the directions parallel to the surface. Whereas the first degree of freedom mostly affects the barrier geometry, the second and third motions can lower or raise the barrier height. The latter effect cannot be described with the usual surface oscillator dynamical models employed in the past to include surface motion, and its dynamical influence on the dissociative adsorption needs to be further investigated.

In the third part of the thesis I addressed the problem of including dissipative effects in the reaction dynamics of hydrogen sticking and scattering on surfaces. I considered dissipative baths with different spectral properties and represented them with a linear chain of coupled harmonic oscillators, exploiting an equivalent effective-mode representation that has recently been developed. I studied the system dynamics with MCTDH, aiming on one hand to an accurate description of dissipation at a short time scale, and on the other hand to a simplified but qualitatively correct behavior of the long time dynamics. In this framework, I found a very useful scheme to represent the long time dynamics of the system without incurring in unwanted Poincaré's recurrences. I used this method to obtain the sticking probability of one hydrogen atom scattered by a simple one dimensional Morse potential. The methodology developed in this work is going to be extended to the more realistic problem of hydrogen sticking on graphitic surfaces.

Contents

Chapter 1

Introduction

Surfaces play a key role in many fields, ranging from traditional catalysis to photocatalysis and electrochemistry. During the last decades, important goals have been achieved in the understanding of the basic phenomena occurring at gas-solid interfaces. This was made possible by the development of increasingly more advanced experimental techniques from one side and by the possibility of studying realistic theoretical models on the other. Among the major achievements of the field, it is worth to mention the complete microscopic characterization of the mechanism of Haber-Bosch ammonia synthesis, for which Gerhard Ertl was awarded with the 2007 Nobel Prize in Chemistry.

However, fundamental questions are still open in the field of surface science. One of the most challenging problems related to the modeling of dynamical phenomena is the inclusion of electronic and nuclear degrees of freedom of the atoms of the solid. Both experimental and theoretical evidence suggests that in some systems phonon coupling or non-adiabatic effects might be crucial in the correct description of phenomena occurring at surfaces.

In my thesis I focus on three different gas-surface systems: H_2 formation on graphite through the Eley-Rideal mechanism, H_2 dissociative adsorption on Cu(111) and, from a more general point of view, the vibrational relaxation and the sticking of H atoms on surfaces. For all the problems considered, the focus is on the development of a theoretical model with a correct description

of the surface, possibly including those effects induced by the surface atoms motion.

In this introduction I present some key concepts about the interaction, the dynamics and the reactions at surfaces. These general ideas constitute the background of the problems considered in the thesis.

1.1 Interaction with surfaces

From the energetics point of view, the interaction of a molecule or an atom with a surface presents the same features of a typical intermolecular potential energy curve. As a function of the distance of the molecule from the surface, the potential shows a repulsive wall at short distances and possibly one or two attractive wells, that allow the existence of stable bound states. When the system is in such bound state, we say that the atom or molecule (the *adsorbate*) is *adsorbed* on the surface.

Adsorption properties, such as energy and geometry, may vary in a wide range, depending on the substrate and the adsorbate itself. Generally, we can distinguish two kinds of adsorption: the physical adsorption or *physisorption*, which is due to weak dispersive forces, and the chemical adsorption or *chemisorption*, which consists in a true chemical bond between the adsorbate and the surface.

1.1.1 Physisorption

Physisorption is due to Van der Waals interactions between the molecule and the surface, and - although weak - is present in any kind of system. It is characterized by a long interaction distance (few Å), energy of the order of 10 meV and no significant relaxation in the structure, either of the surface or of the adsorbate.

The long range dependence of the physisorption potential in case of a dispersive interaction can be easily derived from the well known R^{-6} expression

for the London force [1]. The potential energy for the interaction between two fragments A and B is

$$E_{AB} \propto -\frac{\alpha_A \alpha_B}{R^6} \tag{1.1}$$

where R is the distance between the two interacting fragments, and α_A and α_B are their polarizabilities. Even if this formula is often described as the classical interaction between "instantaneous dipoles" in the electrostatic distribution of the electronic charge, the proper quantum derivation of the formula is based on second-order perturbation theory (see ref. [2] for details).

In the limit of a large surface-adsorbate distance, we can assume atom-atom dispersive forces to be additive. Neglecting three and higher body terms, we can obtain the interaction energy as a sum of two-body terms involving the adsorbate and each atom of the lattice

$$E_{phys} \propto -\sum_i \frac{1}{|\mathbf{R}_{AS_i}|^6}$$

where the sum runs over all the lattice atoms S_i. If we further assume the surface to be a continuous charge distribution, we can convert the sum to an integral $\sum_S \rightarrow \iiint_S \rho dR$

$$E_{phys} \propto -\iiint_S d\mathbf{R} \frac{1}{|\mathbf{R}|^6}$$

where $\mathbf{R}$ is now the distance between the adsorbate and a point of the volume S occupied by the solid. We can perform the integration in cylindrical coordinates

$$\iiint_S d\mathbf{R} \frac{1}{|\mathbf{R}|^6} = \int_d^\infty dz \int_0^{2\pi} d\vartheta \int_0^{+\infty} dr \, \frac{r}{\left(\sqrt{z^2+r^2}\right)^6}$$

where the limit of integration d is the distance between the adsorbate and the surface. Integrating on ϑ and r we get

$$\iiint_S d\mathbf{R} \frac{1}{|\mathbf{R}|^6} = \frac{\pi}{2} \int_d^\infty dz \frac{1}{z^4}$$

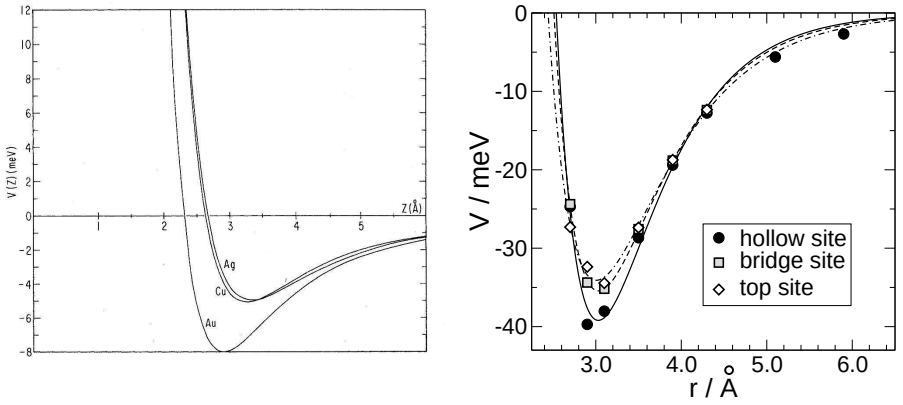

Figure 1.1: Examples of physisorption potentials. Left: adsorption potential of He on noble metals, as a function of the distance of the atom from the metal surface. The picture - taken from ref. [3] - shows results computed by Zaremba and Kohn with the physisorption model described therein. Right: physisorption potential for H on graphite as a function of the distance of the adsorbate from the surface. For each of the high symmetry sites of the graphitic surface, data were obtained with highly correlated wave-function calculation and fitted with a Morse potential [4].

Further integrating on z, we get the d^{-3} long range dependence of the adsorption potential

$$E_{phys} \propto -\frac{1}{d^3} \tag{1.2}$$

Note that to derive this result, we assumed that the molecule is adsorbed on a three dimensional solid, and therefore we included all the bulk atoms in the summation. If we consider adsorption on a single layer (as in the case of graphene, one of the system considered in this thesis as model for a graphitic surface), we omit the integration in z and we get

$$E_{phys} \propto -\frac{1}{d^4} \tag{1.3}$$

Since it is the results of the adding up of weak interactions, physisorption is present in a large variety of systems, irrespective of the nature of both the adsorbate and the surface. As an example, Fig. 1.1 reports the potential energy curves for the physisorption of He on noble metals and of H on graphite are reported. It is interesting to note that the physisorption energy of H on

graphite shows very small changes with respect to the site occupied by the adsorbate. This general property of physisorption is related to the so called *corrugation* of the electronic density, that is small at large distances from the surface.

1.1.2 Chemisorption

When an atom or a molecule is chemisorbed, a true covalent bond is established between the adsorbate and the surface. As for common chemical bonds, chemisorption is characterized by energies of the order of 1 eV and distances of 1-2 Å. This kind of interaction is very sensitive to geometry and orientation, and may require a surface reconstruction. As an example, the chemisorption of atomic hydrogen on graphite requires the atom to be on top of a carbon atom. In addition, the interaction is stable only if the surface relaxes in the so-called *puckered* geometry, *i.e.* the carbon atom beneath moves outside the surface plane by about 0.35 Å [5].

The electronic structure of a chemisorbed atom or molecule is deeply changed by the interaction with the surface electronic states. A simplified description of the physics of chemisorption is given by a model that was developed by Newns [6], on the basis of a method developed by Anderson [7] for the description of bulk impurities. In this qualitative picture, chemisorption is described through the interaction of a single valence state ϕ_a for the adsorbate and a quasi-continuum of Bloch state ϕ_k $(k \in \mathbb{Z})$ for the surface. To treat electron-electron repulsion in an effective one-electron model, Hartree-Fock approximation is applied. In this way, the *Newns-Anderson Hamiltonian* may be written in second-quantized form as

$$H = \varepsilon_a \hat{n}_a + \sum_k \varepsilon_k \hat{n}_k + \sum_k \left(V_{ak} \hat{b_a}^\dagger \hat{b_k} + V_{ka} \hat{b_k}^\dagger \hat{b_a} \right) \tag{1.4}$$

where $\hat{b_i}^\dagger$ and $\hat{b_i}$ are the creation and annihilation operators in the state ϕ_i (with on-site energy ε_i), $\hat{n}_i$ are the corresponding number operators, V_{ak} is the hopping energy between the states ϕ_a and ϕ_k.

Within this model, some interesting results are obtained by means of *Green's operator* techniques. The Green's function $G(\varepsilon)$ for the Newns-Anderson Hamiltonian, formally defined as the resolvent operator

$$[\varepsilon - H]\, G(\varepsilon) = 1 \tag{1.5}$$

is projected on the "unperturbed" state of the adsorbate, giving the Green's function $G_{aa}(\varepsilon)$

$$G_{aa}(\varepsilon) = [\varepsilon - \varepsilon_a - \Sigma(\varepsilon)]^{-1} = \frac{1}{\varepsilon - \varepsilon_a - \Lambda(\varepsilon) + \imath\Delta(\varepsilon)} \tag{1.6}$$

where the self-energy $\Sigma(\varepsilon)$ (that represents the contribution to the state energy due to interactions between the adsorbate and the band) has imaginary part

$$\mathrm{Im}\,\Sigma(\varepsilon) = -\Delta(\varepsilon) = -\pi \sum_k |V_{ak}|^2\, \delta(\varepsilon - \varepsilon_k) \tag{1.7}$$

and real part given by the Hilbert transform of $\Delta(\varepsilon)$

$$\mathrm{Re}\,\Sigma(\varepsilon) = \Lambda(\varepsilon) = \frac{1}{\pi}\,\mathrm{Pr} \int_{-\infty}^{+\infty} \frac{\Delta(\varepsilon')}{\varepsilon - \varepsilon'} d\varepsilon' \tag{1.8}$$

Note that the function $\Delta(\varepsilon)$ is nothing but a weighted density of states, the weights being the matrix elements $|V_{ak}|^2$. In this sense $\Delta(\varepsilon)$ represents the surface density of states "seen" by the adsorbate atom.

The Green's function contains the information about the perturbed state of the Hamiltonian, projected on the adsorbate unperturbed orbital. It is simply related to the projected density of states (PDOS) $n_a(\varepsilon)$, representing the contribution of the state ϕ_a to the full density of states in the interacting system[1]. In particular, it can be shown that

$$n_a(\varepsilon) = -\frac{1}{\pi}\mathrm{Im}\, G_{aa}(\varepsilon) = \frac{1}{\pi} \frac{\Delta(\varepsilon)}{(\varepsilon - \varepsilon_a - \Lambda(\varepsilon))^2 + \Delta^2(\varepsilon)} \tag{1.9}$$

From its definition, we see that the Green's function $G_{aa}(\varepsilon)$ has poles in the eigenvalues of the model Hamiltonian. Since we are interested in states

[1] More correctly, the PDOS is the projection of the density of states on an atomic or molecular orbital, in this case chosen as the valence state of the adsorbate ϕ_a

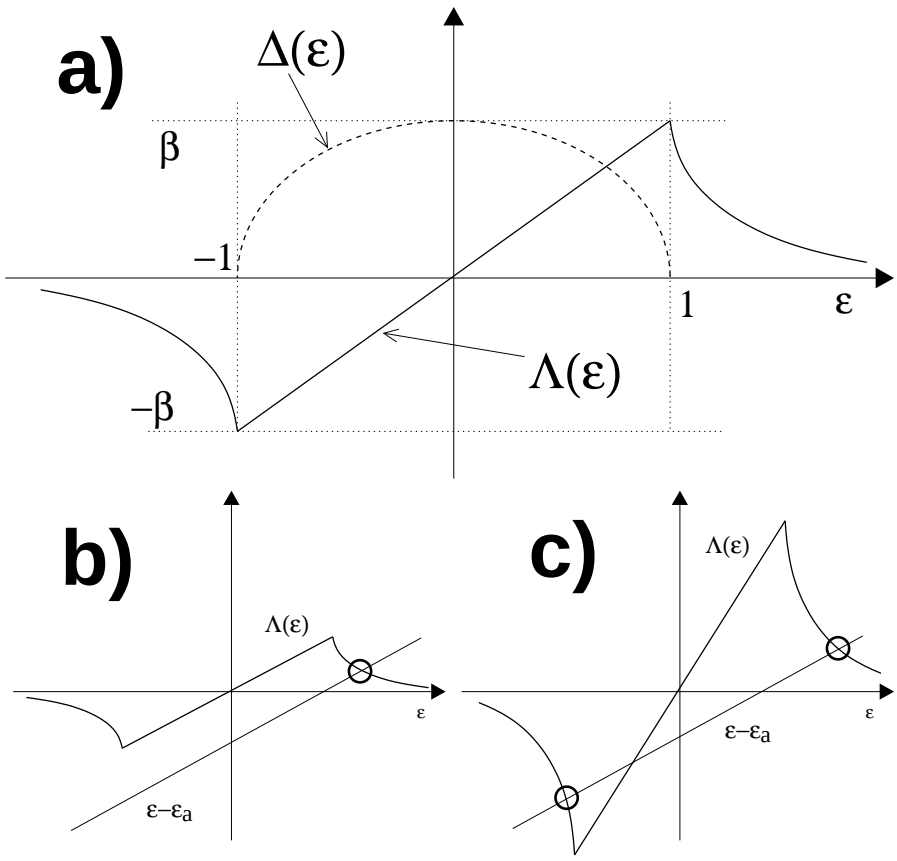

Figure 1.2: Hilbert transform and perturbed localized solutions for a semi-elliptical Δ function. In (a), a semi-elliptical Δ function is depicted, along with the corresponding Λ function. Panels (b) and (c) show the localized solution of Newns-Anderson model in the weak chemisorption and strong chemisorption case, respectively.

which mostly "resemble" the state of the adsorbate and do not belong to the surface, we focus our attention to those eigenvalues that lie outside the band energy interval. Such eigenvalues ε_l, corresponds to a null band density of states $\Delta(\varepsilon_l) = 0$. Hence, from Eq. 1.6, they can be obtained as solution of the equation

$$\varepsilon - \varepsilon_a = \Lambda(\varepsilon) \tag{1.10}$$

To proceed, we need to assume a reasonable functional form for the function $\Lambda(\epsilon)$. Following the discussion of Newns [6], we can choose a semi-

elliptical $\Delta(\varepsilon)$

$$\Delta(\varepsilon) = \begin{cases} \beta\,(1-\varepsilon^2)^{1/2} & |\varepsilon| < 1 \\ 0 & |\varepsilon| > 1 \end{cases} \tag{1.11}$$

and compute its Hilbert transform

$$\Lambda(\varepsilon) = \frac{\beta}{\pi}\,\mathrm{Pr}\int_{-1}^{+1} \frac{(1-\varepsilon'^2)^{1/2}}{\varepsilon-\varepsilon'}d\varepsilon' = \begin{cases} \beta\left(\varepsilon+\sqrt{\varepsilon^2-1}\right) & \varepsilon < -1 \\ \beta\varepsilon & |\varepsilon| < 1 \\ \beta\left(\varepsilon-\sqrt{\varepsilon^2-1}\right) & \varepsilon > 1 \end{cases} \tag{1.12}$$

The shape of such Λ function is reported in Panel (a) of Fig. 1.2.

The equations above can be used to discuss two very interesting limiting cases. In the *weak chemisorption regime*, the interaction between the adsorbate and the surface is small. Consequently, Δ and Λ are slowly varying functions in the scale of the bandwidth. As depicted in Panel (b) of Fig. 1.2, there is just one solution of Eq. 1.10, which differs little from ε_a, the energy of the unperturbed state. In addition, substituting $\Delta \approx \textit{constant}$ and $\Lambda \approx 0$ in Eq. 1.9, we find that the PDOS has a Lorentzian peak centered around this energy value:

$$n_a(\varepsilon) = \frac{1}{\pi}\frac{\Delta}{(\varepsilon-\varepsilon_a)^2+\Delta^2} \tag{1.13}$$

In conclusion, in the weak interaction regime the adsorbate state contribute to the density of states with an approximately Lorentzian peak near the energy level of the unperturbed valence state itself. With regards to this point, we note that if we imagine to switch the interaction off and let $\Delta \to 0$, the Lorentzian density of states tends to a Dirac delta centered around the value ε_a. In this limit, the perturbed localized state properly becomes the unperturbed adsorbate state.

The opposite limiting case is the strong chemisorption regime. In this case a substantial interaction is established between the adsorbate and the surface electron band. As schematically pictured in Panel (c) of Fig. 1.2, the Hamiltonian admits two localized solutions, one above and one below the solid band. In analogy with ordinary molecular orbital theory, the valence state of the adsorbate give raise to a bonding and an anti-bonding peak in the density of states.

1.2 Dynamics at surfaces

In this section, we want to schematically define the fundamental dynamical phenomena that may take place when an atoms or a molecule collides with a surface. We imagine that a beam of atoms or molecules is directed to the surface and describe the possible events that may follow. This kind of experiment has a great fundamental interest in surface science, since it gives the possibility of a direct comparison between theory and experiments. Indeed, experiments of this kind have been realized for a variety of systems, thanks to technological developments, such as molecular beams, ultra-high vacuum, laser spectroscopy.

1.2.1 Atomic and molecular scattering

The simplest event that may take place after the collision with the surface is *scattering*: the atom or molecules is reflected back to the gas-phase (possibly in a different rovibrational state, if any internal degree of freedom is present).

In scattering, the 2D discrete periodicity of the interaction causes the well known quantum phenomenon of *diffraction*, *i.e.* the fact that momentum is exchanged only in discrete quantities. In this case the Hamiltonian H - depending on the center of mass of the atom - is composed by the kinetic energy term, which is symmetric under continuous 3D translations, and the potential energy term, which shows the 2D discrete translational properties of the surface. Hence the Hamiltonian commutes with the 2D discrete group of the translations of the surface, that we label with two indices m, n

$$[H, T_{mn}] = 0 \qquad \forall\, m, n \in \mathbb{Z} \tag{1.14}$$

Since the time evolution operator U_t is function of the Hamiltonian, the same commutator expression applies for U_t

$$[U_t, T_{mn}] = 0 \qquad \forall\, m, n \in \mathbb{Z} \tag{1.15}$$

We assume that the system is initially in a state with specific parallel momentum $\mathbf{k}_{\parallel}$. We want to find the probability for the system to be scattered in

a state with different momentum $\mathbf{k}'_{\parallel}$. Computing the expectation value of the commutator of Eq. 1.14 between the initial and final momentum states, we find

$$\left\langle \mathbf{k}_{\parallel} \right| U_t T_{mn} - T_{mn} U_t \left| \mathbf{k}'_{\parallel} \right\rangle = 0$$

The plane waves $\left|\mathbf{k}'_{\parallel}\right\rangle$ and $\left|\mathbf{k}_{\parallel}\right\rangle$ are eigenvectors of the translation operators:

$$T_{mn} \left|\mathbf{k}_{\parallel}\right\rangle = e^{-\imath \mathbf{k}_{\parallel} \mathbf{t}_{mn}} \left|\mathbf{k}_{\parallel}\right\rangle$$

$$T_{mn} \left|\mathbf{k}'_{\parallel}\right\rangle = e^{-\imath \mathbf{k}'_{\parallel} \mathbf{t}_{mn}} \left|\mathbf{k}'_{\parallel}\right\rangle$$

where $\mathbf{t}_{mn}$ is the vector of the translation labelled by m, n. For the reader familiar with the theory of group representation, we can equivalently say that $\left|\mathbf{k}'_{\parallel}\right\rangle$ and $\left|\mathbf{k}_{\parallel}\right\rangle$ span two one dimensional representations of the 2D discrete group of the translations.

Letting $\mathcal{T}_{mn}$ act on the state $\left|\mathbf{k}'_{\parallel}\right\rangle$ and $\left|\mathbf{k}_{\parallel}\right\rangle$, the commutator expectation becomes

$$\left(e^{-\imath \mathbf{k}'_{\parallel} \mathbf{t}_{mn}} - e^{-\imath \mathbf{k}_{\parallel} \mathbf{t}_{mn}} \right) \left\langle \mathbf{k}_{\parallel} \right| U_t \left| \mathbf{k}'_{\parallel} \right\rangle = 0 \tag{1.16}$$

This equality holds if

$$e^{-\imath \mathbf{k}'_{\parallel} \mathbf{t}_{mn}} = e^{-\imath \mathbf{k}_{\parallel} \mathbf{t}_{mn}} \qquad \forall m, n \in \mathbb{Z}$$

$$e^{-\imath \left(\mathbf{k}'_{\parallel} - \mathbf{k}_{\parallel} \right) \mathbf{t}_{mn}} = 1 \qquad \forall m, n \in \mathbb{Z}$$

Comparing last equality with the definition of reciprocal lattice (see *e.g.* [8]), we realize that $\mathbf{k}'_{\parallel} - \mathbf{k}_{\parallel}$ has to be a vector of the reciprocal lattice. Otherwise, the condition expressed by Eq. 1.16 forces us to conclude that

$$\left\langle \mathbf{k}_{\parallel} \right| U_t \left| \mathbf{k}'_{\parallel} \right\rangle = 0$$

In other words, no transition is possible between the states $\left|\mathbf{k}'_{\parallel}\right\rangle$ and $\left|\mathbf{k}_{\parallel}\right\rangle$.

In conclusion, the periodicity of the interaction determines a strict constraint on the momentum exchanged in atomic scattering. The momentum difference has to be a vector of the reciprocal lattice corresponding to the 2D

translations of the surface. For conservation of energy, if we assume the surface to be static, the change in parallel momentum has to be compensated by the change in the perpendicular momentum of the scattered atom. This gives raise to the typical diffraction pattern which is found in electron or atomic scattering on surfaces.

When a molecule is scattered, diffraction takes place as well. In this case, however, the scattered species has internal degrees of freedom which might be coupled to the translational coordinates *via* the interaction with the surface. This may lead to energy conversion between translational and internal degrees of freedom. The diffraction pattern hence is much more structured than the one resulting from atomic scattering. In this case, the scattering is said to be *elastic* when the final rovibrational state of the molecule is the same as the initial one. On the other hand, scattering is *inelastic* when the final states differs from the initial one.

1.2.2 Sticking

So far, we have assumed that after the interaction with the surface, the atom or the molecule is reflected back to the gas phase. However, in appropriate conditions *sticking* can also take place. The sticking probability is defined as the fraction of atoms or molecules impinging on the surface which are not scattered back and remain on the surface. From a microscopic point of view, sticking requires that most of the translational energy is transferred to other degrees of freedom, so that the atom or the molecule is trapped in an adsorption well of the interaction potential.

In the case of atomic scattering (or even molecular sticking in which the molecule stays intact on the surface), no internal degree of freedom can accommodate the translational energy. Hence in this kind of process *dissipation* plays a fundamental role: during the collision mechanical coupling with phonons or non adiabatic coupling with electrons could transfer energy to the lattice. If the energy loss is high enough, the atom can be trapped in the adsorption well.

A very crude model for the description of atomic sticking is the so-called hard-cube model [9]. In this model the surface is thought as a cube of effective mass M_C moving with an appropriate velocity distribution. The atom or molecule colliding with the surface transfers to the cube an amount of energy which can be found imposing energy and momentum conservation. The impinging species is trapped if the energy after the collision is smaller than the adsorption well depth.

Within this simple analytical model, a particle of mass m and initial velocity v_g colliding with a surface in a square adsorption well of depth E_{ad} gets trapped if the hard cube is moving with a velocity that is less than a limit velocity v_{lim}

$$v_c < v_{lim} = \frac{1+\mu}{2}\sqrt{\frac{2E_{ad}}{m}} - \frac{1-\mu}{2}\sqrt{v_g^2 + \frac{2E_{ad}}{m}} \tag{1.17}$$

where μ is the mass ratio m/M_c. As expected, it is more likely that the atom gets trapped when the energy transfer is maximum and when $v_g \ll \frac{2E_{ad}}{m}$, since for such parameters, the limit velocity is higher. Integrating a Maxwell distribution for the hard-cube velocity up to v_{lim}, we get the trapping probability of a particle

$$P_{trap}(v_g) = \frac{1}{2} + \frac{1}{2}\mathrm{erf}\left[\alpha v_{lim}\right] - \frac{\exp\left[-\alpha^2 v_{lim}^2\right]}{2\sqrt{\pi}\alpha\sqrt{v_g^2 + \frac{2E_{ad}}{m}}} \tag{1.18}$$

where α is a parameter describing the width of the hard cube velocity distribution (hence connected to the surface temperature, $\alpha^2 \propto 1/T_S$).

The hard-cube model explains many trends of atomic sticking that are effectively found in real systems, like scattering of rare gas atoms on metal surfaces (see Fig. 1.3). First, the sticking probability decreases with increasing kinetic energy of the projectile atom. This is due to the fact that at higher kinetic energy, the incoming particle has to lose more energy to be trapped in the adsorption well, and at the same time the energy transfer becomes less efficient. Furthermore, the model shows the well-known effect of the particle mismatch: when the ratio between the particle mass and the effective mass

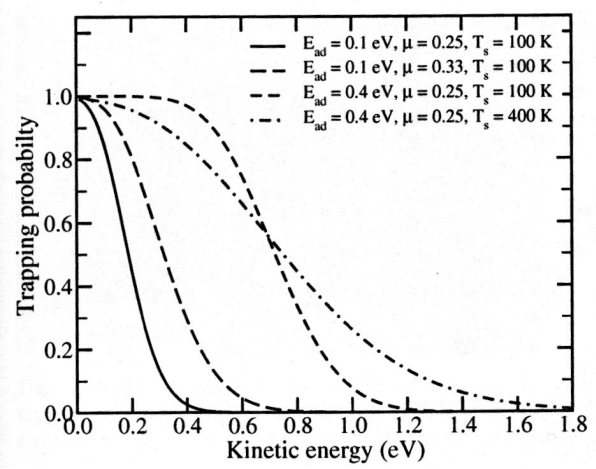

Figure 1.3: Sticking probability as a function of the kinetic energy of the incident atom, computed according to the hard-cube model (Eq. 1.18) for different values of the adsorption energy E_{ad}, of the mass ratio μ and of the surface temperature T_S. The picture is taken from Ref. [2].

of the cube increases, more energy is transferred to the surface and the trapping probability increases. Finally, increasing the surface temperature leads to another well known effect: averaging over a broader range of surface atom velocities leads to a broader sticking probability curve [2].

As can be seen in Fig. 1.3, in the hard-cube model the sticking probability tends to 1.0 for vanishing kinetic energy of the projectile. However, this holds only for a classical projectile and non-activated sticking. The presence of a barrier, not taken into account in the simple model we discussed, may prevents sticking at low kinetic energy. As an example, H (or D) chemisorption on graphite requires an electronic structure reconstruction that results in a 0.3 eV barrier. Hence the projectile needs a high translational energy to get into the adsorption well and to possibly be trapped there. In this case the sticking probability tends to 0 at small incident energy and has the shape shown in Fig. 1.4.

Generally speaking, quantum effects may act in two different directions. On one hand, in systems with activated absorption, *tunnelling* may increase the sticking probability for incident energies that are lower than the height

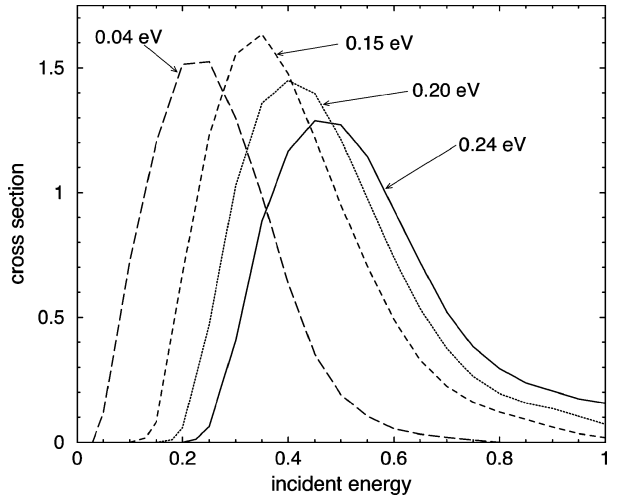

Figure 1.4: The trapping cross section (in $Å^2$) as a function of the incident energy, for D normally incident on a 150 K graphite surface. Results are shown for model potential with barriers of 0.24, 0.20, 0.15 and 0.04 eV, as indicated. The picture is taken from Ref. [10].

of the barrier. On the other hand, *quantum reflection* leads to a lower sticking probability at 0 K, even in the case of non-activated adsorption.

1.2.3 Dissociative adsorption

In the case of molecules, sticking may take place with the conversion of translational energy to internal degrees of freedom. Such is the case of many diatomic molecules that are adsorbed on transition metals surfaces with dissociation of the molecule itself. Well known is the case of *dissociative chemisorption* of H_2 on metals, like Cu and Pt, which is relevant for many industrial catalytic processes.

For a hydrogen molecule impinging on a metal surfaces, the high mass mismatch essentially prevents non-dissociative sticking. In this kind of systems, dissociative adsorption has a much higher probability. The feasibility of the dissociation of the H-H bond (energetically much more expensive in gas-phase) is explained by a model due to Hammer and Nørskov including both the bonding σ and the anti-bonding $\sigma^\star$ orbital of the molecule, and the

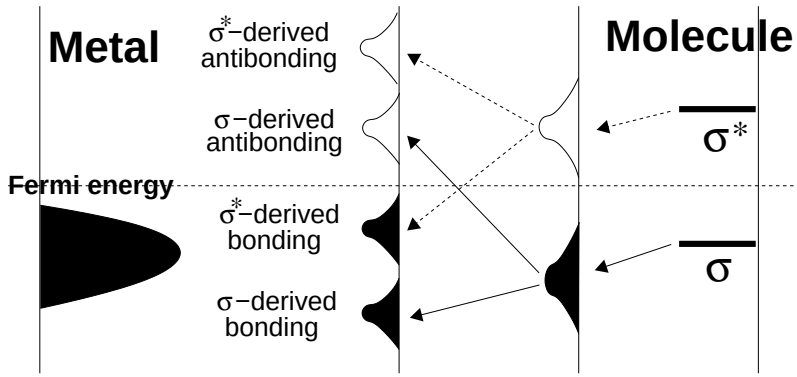

Figure 1.5: Electronic structure in dissociative chemisorption

sp and *d* bands of the metal [11]. The interaction with the *sp* band cause a Lorentzian enlargement and a shift of both levels in the density of states, in accordance with the Newns-Anderson weak chemisorption picture. This effect is not enough to determine the dissociation of H-H bond, as shown in the case of *sp*-metals (like Al) that cannot dissociatively adsorb hydrogen.

In transition metals, the further strong interaction with the *d* electrons leads to a splitting of both bonding and anti-bonding levels, as predicted for strong chemisorption in the Newns-Anderson model (see Section 1.1.2). Hence four bands are formed, two coming from the splitting of the σ state and two from the $\sigma^\star$ state. Depending on the strength of the interaction and the position of the Fermi level, it is possible that one $\sigma^\star$ band is lower in energy than a σ band, as schematically represented in fig. 1.5. This results in a weakening of the molecule bond that allows the dissociation of the molecule.

The sticking probabilities for H_2 on transition metals have been extensively studied, both theoretically and experimentally. H_2 on Cu is the typical example of activated chemisorption, in which the dissociation requires overcoming a high barrier (of the order of 1.0 eV). H_2 on Pt, on the other hand, is the benchmark system for non-activated dissociative adsorption. This opposite behaviour can be explained by the model described above, and relies on the different coupling between the states of the molecule and the *d*-band of the metal. The larger spatial extension of the *d* orbitals of Pt leads to a stronger

interaction, causing an additional stabilization of the dissociating molecule [11].

1.3 Reactions at Surfaces

Many reactions are made possible by the interaction with a surface, that acts as a catalyst by increasing the rate of a step which is inhibited in the gas-phase. Among these catalytic reactions, there are processes of great industrial relevance, such as the synthesis of ammonia or the catalytic hydrogenation of unsaturated hydrocarbons [12].

As an example, in the gas phase the thermodynamically favoured synthesis of ammonia from H_2 and N_2 is prevented by a very slow kinetics, due to the high energy barrier in the dissociation of the N-N triple bond. The iron catalyst surface dissociatively adsorbs nitrogen with a much smaller reaction barrier. At the same conditions, H_2 is dissociated and chemisorbed to the surface, too. Step by step, the diffusing N atoms can bind three H atoms and then desorb to the gas-phase.

Similarly, hydrogenation reactions are not feasible in the gas-phase due to the dissociation barrier of the hydrogen molecule. As discussed in the previous section, transition metals like Pt and Pd may dissociate H_2, even without any barrier to reaction. The H atoms formed by dissociative adsorption can diffuse and react with an adsorbed hydrocarbon molecule. Different H atoms bind to an unsaturated $C-C$ bond and then the hydrogenated hydrocarbon leaves the surface.

From a general point of view, a complex reaction can be described in a schematic way with one of three possible mechanisms.

The most common in ordinary condition is the *Langmuir-Hinshelwood* (LH) mechanism, which is involved in both the reaction described above. In this case the reaction takes place between two fragments which have been both adsorbed on the surface of the catalyst. These two fragments are trapped long enough to reach thermal equilibrium with the surface. When they get close

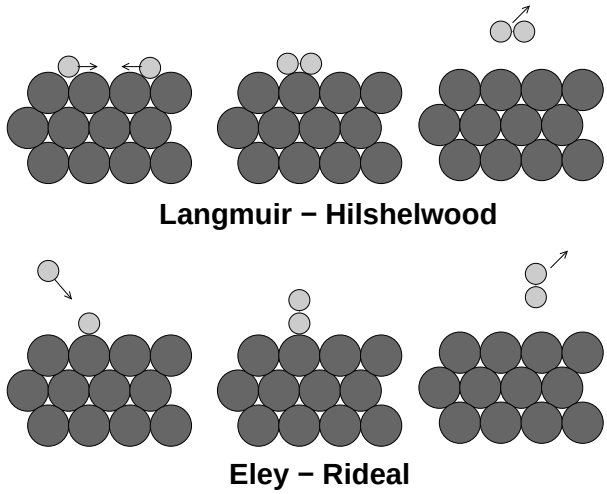

Figure 1.6: Reaction mechanism at surfaces: schematic representations of the Langmuir-Hinshelwood (top) and Eley-Rideal (bottom) mechanisms

one to each other by thermal diffusion, they recombine giving the product that may further react or desorb to the gas phase.

In the *Eley-Rideal* (ER) mechanism, on the contrary, just one of the two reacting species is adsorbed on the surface. An atom or a molecule coming from the gas-phase directly collides with the adsorbed fragment and forms the reaction product. This mechanism is important in extreme conditions - *e.g.* in very low temperature regimes - when the diffusion of adsorbed species is slow and the collision with a gas-phase species becomes more likely than the reaction of two adsorbed reactants.

The *Hot-Atoms* (HA) mechanism is intermediate between LH and ER. In this case one of the the reacting species is a so-called Hot Atom, *i.e.* an atom which has been captured by the surface but has not completely dissipated its kinetic energy, yet. Unlike the reactants of LH mechanism, which are in thermal equilibrium, the hot atoms move in a super-diffusive regime.

Each of the mechanism described above involves many surface elementary steps, *e.g.* dissociative or non-dissociative sticking, diffusion, desorption. From a theoretical point of view, each step can be independently modeled to get information on the energetics and the dynamics. As in any complex reac-

tion mechanism, the step which is slower than the others is the rate limiting step, *i.e.* the step that determines the overall kinetics of the reaction.

1.4 Thesis overview

In the present thesis, three different fundamental surface processes will be considered. All the problems will be discussed from a theoretical point of view, with a particular interest in the inclusion of effects related to the surface description and lattice atoms motion.

In chapter 3, I will consider the non activated Eley-Rideal recombination of H_2 on graphitic surfaces. Previous theoretical simulations adopted different dynamical and energetics models for the surface carbon atoms, and lead to inconsistent results. In this part of the thesis, I systematically investigate under simplified conditions how the model choice influences the reaction probability. Quantum dynamics is studied in an extremely low energy range, highlighting the strong dependence of quantum reflection on the adopted surface model.

In chapter 4, I will focus on the dissociative sticking of H_2 on the Cu(111) surface. For this reaction, theoretical results have been recently obtained in very good agreement with most available experiments. However, for some experiments there is still a large discrepancy which is likely to be due to the effect of the surface phonons on the reaction. The results presented in the chapter try to establish a relation between the surface atoms motion and the reaction barrier, with the aim of showing which surface coordinates are likely to be the most important for the description on hydrogen dissociative adsorption.

In chapter 5, vibrational energy relaxation and sticking of an adsorbate on a surface will be considered from a methodological point of view, with the aim of developing a technique that could be effectively applied to realistic problems, such as the sticking of H on graphite. The problem is addressed in the framework of system-bath quantum dynamics: the interesting dynamical system can exchange energy with the environment, considered as a huge set

of harmonic degrees of freedom in thermal equilibrium. In particular, it will be proposed an approximation scheme that can be consistently applied and gives excellent results at a much cheaper computational cost than the standard approach followed until now.

Although different systems are considered, in all the problems addressed in this thesis a particular role is played by the description and the motion of the surface. In particular, we can schematically identify two different effects: an *active role* and a *passive role* of the lattice atoms.

In the first two problems the lattice atoms have an active role, since they are considered for the direct effect that they might have on the course of the reaction. Different surface description (for H+H / Graphite) or slightly displaced surface atom positions (for H_2/ Cu(111)) can induce changes in the reaction potential properties, like the barrier height or the curvature of the potential. From a dynamical point of view, the inclusion of such effect requires a small number of additional degree of freedom. Furthermore, in many cases the description can be simplified by means of an appropriate (sudden or adiabatic) approximation, in which the additional degrees of freedom is only effectively included in the system.

In the case of sticking or vibrational relaxation, addressed in chapter 5, the lattice plays the passive role of a thermal reservoir exchanging energy with the reacting system. In addition to the direct effects described above, the coupling to a thermal bath determines energy dissipation, energy fluctuations and coherence loss. To properly take into account all these effects in a realistic dynamical model, a large number of degrees of freedom needs to be explicitly included in the description. This presents a a serious challenge for quantum dynamics, due to its well known unfavourable scaling with the number of degrees of freedom. For this reason, the development of a realistic model for an atom-surface process would be impossible without an approximation on the quantum dynamical description, like the one proposed in this thesis.

Bibliography

[1] H. Ibach, *Physics of surfaces and interfaces*, Springer (2006).

[2] A. Gross, *Theoretical surface science: a microscopic perspective*, Advanced texts in physics, Springer (2003).

[3] E. Zaremba and W. Kohn, *Phys. Rev. B* **15**, 1769 (1977).

[4] M. Bonfanti, R. Martinazzo, G. F. Tantardini and A. Ponti, *J. Phys. Chem. C* **111**, 5825 (2007).

[5] X. Sha and B. Jackson, *Surf. Sci.* **496**, 318 (2002).

[6] D. M. Newns, *Phys. Rev.* **178**, 1123 (1969).

[7] P. W. Anderson, *Phys. Rev.* **124**, 41 (1961).

[8] N. Ashcroft and N. Mermin, *Solid state physics*, Science: Physics, Saunders College (1976).

[9] E. K. Grimmelmann, J. C. Tully and M. J. Cardillo, *J. Chem. Phys.* **72**, 1039 (1980).

[10] J. Kerwin and B. Jackson, *J. Chem. Phys.* **128**, 084702 (2008).

[11] B. Hammer and J. Nørskov, *Surf. Sci.* **343**, 211 (1995).

[12] G. Somorjai and Y. Li, *Introduction to Surface Chemistry and Catalysis*, Wiley (2010).

Chapter 2

Method

In this section the general methods for the quantum simulation of an atom/molecule scattering on surfaces will be presented. The starting point of the discussion is the *Born-Oppenheimer separation* of electronic and nuclear motion. We consider the evolution of a nuclear wavefunction

$$H_{ion}\Phi(\mathbf{R},t) = \imath\hbar\frac{\partial}{\partial t}\Phi(\mathbf{R},t) \qquad H_{ion} = -\frac{\hbar^2}{2M}\nabla^2_{\mathbf{R}} + V(\mathbf{R}) \tag{2.1}$$

with an interaction potential which is solution of the the electronic problem

$$H_e\Psi(\mathbf{r};\mathbf{R}) = V(\mathbf{R})\Psi(\mathbf{r};\mathbf{R}) \tag{2.2}$$

parametrically dependent on the geometrical arrangement of the nuclei.

The full quantum dynamical solution of a scattering problem requires (1) the computation of the *Potential Energy Surface* (PES) $V(r)$, (2) its representation by means of an interpolation or fitting procedure with a convenient functional form and (3) the solution of the time evolution equation for the nuclei.

A common method adopted to compute the electronic energy is Density Functional Theory (DFT), that is briefly discussed in Section 2.1. In our work, DFT techniques have indeed been adopted for addressing H_2 formation on graphite and H_2 dissociation on Cu(111). For the H scattering problem, on the contrary, a Morse model potential was used to describe atom-surface interaction.

In Section 2.2, the Time-Dependent Wave-Packet approach to the solution of the nuclear quantum dynamical equation will be presented. In particular, the focus will be on the exact wavepacket technique adopted for the H_2/Graphite calculations and on the Multi-Configuration Time-Dependent Hartree (MCTDH) approach, followed for H scattering and vibrational relaxation.

2.1 Density Functional Theory

The key result of *Density Functional Theory* (DFT) is a theorem proved by Hohenberg and Kohn in 1964 [1]. They showed the existence of a one-to-one correspondence between the ground state solution of the electronic problem and the *electron density*, a much simpler function defined as

$$\rho(\mathbf{r}) = N \int_{-\infty}^{+\infty} d\mathbf{r}_2 \dots \int_{-\infty}^{+\infty} d\mathbf{r}_N \, |\Psi(\mathbf{r}, \mathbf{r}_2, \dots \mathbf{r}_N)|^2 \tag{2.3}$$

As a consequence, in principle the ground state energy can be written a unique functional of the ground state energy. The great advantage of such idea is the replacement of the many-body wavefunction $\Psi(\mathbf{r}_1 ... \mathbf{r}_N)$, depending on $3N$ spatial variables, with the electron density $\rho(\mathbf{r})$, which is function of just 3 variables.

Difficulties in the actual implementation of DFT methodologies arise from the fact that an explicit analytical expression of the density functional is not known. To solve this problem, Kohn and Sham proposed an approach based on a mapping of the actual system to a fictitious non interacting system with the same electron density [2]. With this expedient, the solution of the electronic problem can be equivalently found as a non interacting electron density

$$\rho(\mathbf{r}) = \sum_{i=1}^{N} |\chi_i(\mathbf{r})|^2 \tag{2.4}$$

which is sum of the densities of the Kohn-Sham orbitals, solutions of the single particle *Kohn-Sham equation*

$$\left[-\frac{\hbar^2}{2m} \nabla^2 + v_{\text{ext}}(\mathbf{r}) + e^2 \int \frac{\rho(\mathbf{r}')}{|\mathbf{r} - \mathbf{r}'|} d\mathbf{r}' + v_{XC}(\mathbf{r}) \right] \chi_i(\mathbf{r}) = \varepsilon_i \chi_i(\mathbf{r}) \tag{2.5}$$

where $v_{\text{ext}}(\mathbf{r})$ is the ion external potential and $v_{XC}(\mathbf{r})$ is the so-called *exchange-correlation potential*, accounting for the energy terms that are not analytically known and for which further approximations are required. Kohn-Sham equation can be solved iteratively at a computational cost that is comparable with Hartree-Fock methods (or even smaller, if a local exchange-correlation functional is chosen).

A large number of functional forms for the exchange-correlation potential have been suggested since the work of Kohn and Sham. However, most of them belong to three main categories: *Local Density Approximation* (LDA), *Generalized Gradient Approximation* (GGA) and *hybrid* functionals.

In the Local Density Approximation , the exchange-correlation functional is computed as

$$E_{XC}^{LDA}[\rho] = \int \rho(\mathbf{r})\varepsilon_{XC}\left(\rho(\mathbf{r})\right)\, d\mathbf{r} \tag{2.6}$$

where $\varepsilon_{XC}(\rho)$ is the exchange-correlation energy computed for a system with uniform electron density ρ [3]. The LDA approximation, although very crude, gives already a good description of systems with a smoothly varying electron density, such as alkali metals.

To improve the results, many Generalized Gradient Approximation functionals have been proposed. In this case, the exchange-correlation energy is written as a functional of the electron density and its gradient

$$E_{XC}^{GGA}[\rho] = \int \rho(\mathbf{r})\varepsilon_{XC}\left(\rho(\mathbf{r}), \nabla\rho(\mathbf{r})\right)\, d\mathbf{r} \tag{2.7}$$

GGA functionals have been successfully used for electronic structure calculations of adsorbate on transitions metals. Among the large number of different GGA functionals available, the ones adopted in this work are the Perdew-Burke-Ernzerhof (PBE) functional [4], the revised Perdew-Burke-Ernzerhof (RPBE) functional [5] and the Perdew-Wang 1991 (PW91) functional [6].

A third class of approximations consists in the so-called hybrid functionals. In this case the exchange-correlation energy functional mix a portion of exact exchange from Hartree-Fock theory with exchange and correlation from other sources (such as other GGA or LDA functionals) [7]. One of the most

commonly used hybrid functionals is the Becke 3-Parameter Lee-Yang-Parr (B3LYP) functional. This approximation scheme was proposed to improve the results in the case of molecular properties, which tends to be poorly described by the other methods that are mostly suited for electrons in metals.

2.2 Time-Dependent Wavepacket methods

In the framework of *Time-Dependent Wavepacket* (TDWP) methods, the solution of a time-dependent Schrödinger equation

$$H\Phi(\mathbf{R},t) = \imath\hbar\frac{\partial}{\partial t}\Phi(\mathbf{R},t) \tag{2.8}$$

is found by representing the wavefunction on a finite basis and by evolving the system in time with convenient operator techniques. In the following I will just address in general terms these two problems, the representation and the evolution of the wavefunction. I will not give a detailed description of all the technical aspects of a TDWP implementation, which are largely dependent on the specific problem considered. At the end of the section, an approximate time dependent approach will be discussed, *i.e.* the Multi-Configuration Time-Dependent Hartree (MCTDH) method.

Further technical aspects connected to quantum scattering theory are presented in Appendix A.

2.2.1 Representation of the wavefunction

The standard TDWP methodology described above assumes an expansion of the wavefunction into a direct-product basis

$$\Phi(r_1 ... r_f, t) = \sum_{j_1}^{N_1} \dots \sum_{j_f}^{N_f} C_{j_1 \dots j_f}(t)\ |j_1\rangle \dots |j_f\rangle \tag{2.9}$$

where a set of N_i basis functions $|j_i\rangle$ is chosen for each of the f degrees of freedom [8].

Very often the basis functions are built with the *Discrete Variables Representation* (DVR) technique [9–11], that is briefly outlined in the following,

within the theoretical framework introduced by R. G. Littlejohn and M. Cargo [12, 13].

Let $\mathcal{H}$ be the Hilbert space of functions on the configuration space $\mathbb{M}$, defined by the coordinates of the nuclei. We choose a grid $\{x_a\}$ of points in $\mathbb{M}$ and a projector P in $\mathcal{H}$. We suppose that our wavefunction belongs to the range of the projector. In the applications, this generally does not hold and the representation becomes approximated. We define a set of functions projecting the Dirac delta states corresponding to the chosen grid points

$$|\alpha\rangle = \frac{1}{\sqrt{N_\alpha}} \mathcal{P} |x_\alpha\rangle \tag{2.10}$$

where N_α is a normalization factor. If the $|\alpha\rangle$ states form an orthonormal set

$$\langle\alpha|\beta\rangle = \delta_{\alpha\beta} \tag{2.11}$$

they are a convenient basis for the representation of the system, since they satisfy the interpolation property

$$\langle\alpha \mid \psi\rangle = \frac{1}{\sqrt{N_\alpha}} \psi(x_\alpha) \tag{2.12}$$

From the interpolation property we find that the coefficients for the expansion of $|\psi\rangle$ on the basis $|\alpha\rangle$ are just the values of the wavefunction on the grid (except for a normalization factor)

$$|\psi\rangle = \sum_\alpha |\alpha\rangle \langle\alpha \mid \psi\rangle = \sum_\alpha \frac{1}{\sqrt{N_\alpha}} \psi(x_\alpha) |\alpha\rangle$$

The coefficients $\frac{1}{\sqrt{N_\alpha}} \psi(x_\alpha)$ are the Discrete Variable Representation of the function $|\psi\rangle$.

A common way to define the projector P is to built it from an orthonormal set of function $|n\rangle$ as

$$P = \sum_n |n\rangle \langle n| \tag{2.13}$$

In this case, we can also expand the function $|\psi\rangle$ on the basis $|n\rangle$

$$|\psi\rangle = \sum_n |n\rangle \langle n \mid \psi\rangle = \sum_n c_n |n\rangle \tag{2.14}$$

The coefficients $c_n = \langle n \mid \psi \rangle$ are the Finite Basis Representation of the function $|\psi\rangle$. The two representation are obviously related by a similarity transform, whose matrix element is

$$U_{\alpha n} = \langle \alpha \mid n \rangle = \frac{1}{\sqrt{N_\alpha}} \phi_n(x_\alpha) \tag{2.15}$$

The main advantage of representing the wavefunction with a DVR basis set is the possibility of computing the action of the potential operator (or any operator that is local in the configuration space) with a simple multiplicative operation:

$$\langle \phi \mid V|\psi\rangle = \sum_\alpha \frac{1}{N_\alpha} \phi(x_\alpha)^\star V(x_\alpha) \psi(x_\alpha) \tag{2.16}$$

Different type of DVR are possible and the choice has to be done in accordance with the properties of each degree of freedom. Representations based on orthogonal polynomials are particularly convenient when those polynomials are eigenvectors of a part of the Hamiltonian: *e.g.* Hermite polynomials (the *Gauss-Hermite DVR* [14]) for vibrational degrees of freedom, spherical harmonics (the *Gauss-Legendre DVR* [15]) for rotational degrees of freedom. In case of scattering coordinates, on the other hand, a convenient choice is the DVR based on a finite and discrete set of plane waves [13].

2.2.2 Time evolution

Given an initial wavefunction $\Phi_0(\mathbf{R}) = \Phi(\mathbf{R}, t)$, Time-Dependent Schrödinger Equation can be integrated and gives

$$\Phi(\mathbf{R}, t) = \exp(-\frac{\imath}{\hbar} H t) \Phi_0(\mathbf{R}) \tag{2.17}$$

so to fully describe the evolution of the system, it is necessary to compute the time evolution operator, *i.e.* the exponential $\exp(-\frac{\imath}{\hbar} H t)$ [8].

The time evolution operator can be computed by direct diagonalization of the Hamiltonian just for very small systems, hence approximations techniques are necessary. One of the most common is the so-called *Split Operator* (SPO) method, based on the *Trotter expansion* of the time evolution operator.

When an operator can be written as a sum of non commuting operators, its exponential can be expanded as

$$e^{(A+B)t} = \lim_{n\to\infty} \left(e^{A\Delta t} e^{B\Delta t}\right)^n \qquad \Delta t = \frac{t}{n} \tag{2.18}$$

The last formula can be used in our case to split the kinetic and the potential part of the operator. We divide the time evolution from 0 to t in small Δt steps, and, at each steps, apply the following time evolution operator [16]

$$\exp(-\frac{\imath}{\hbar} H\Delta t) \approx \exp(-\frac{\imath}{\hbar} K\frac{\Delta t}{2}) \exp(-\frac{\imath}{\hbar} V\Delta t) \exp(-\frac{\imath}{\hbar} K\frac{\Delta t}{2}) + O(\Delta t^3) \tag{2.19}$$

This approximation simplify the problem of the evolution, since it allows to take advantage of the properties of each operator that compose the Hamiltonian. As an example, the potential part of the evolution can be applied as a local operator, when a DVR basis set is employed.

Generally, in a TDWP calculation we start from an initial state representing our initial conditions, usually a wavefunction that is product of a Gaussian wavepacket for the scattering coordinate and of appropriate eigenfunctions for the other coordinates. With one of the techniques that have been developed to compute the time evolution operator, such as the SPO approximation, we propagate the system in time up to the desired time. We then extract the results we are interested in, such as the probability for the process we want to study. The reader interested in a more detailed description of the analysis methodology, should refer to Appendix A.

2.2.3 Multi-Configuration Time-Dependent Hartree

The main drawback of standard TDWP technique is the strong exponential increase with the number of DOFs of both the computation time and the memory requirements. With today's computer, it is difficult to go beyond systems of more than 6 degrees of freedom.

In the past, different wavefunction expansions have been proposed to avoid this exponential scaling. One of the most successful method, the *Multi-Configuration Time-Dependent Hartree*, has been proposed in 1990 by Meyer, Manthe and Cederbaum [17–19].

The basis of this method is a different wavefunction expansion:

$$\Phi(r_1 \dots r_f, t) = \sum_{j_1}^{N_1} \dots \sum_{j_f}^{N_f} A_{j_1 \dots j_f}(t)\, \phi_{j_1}^{(1)}(r_1, t) \dots \phi_{j_f}^{(f)}(r_f, t) \tag{2.20}$$

This wavefunction *ansatz* is a direct-product expansion of f sets of orthonormal time-dependent basis function $\left\{\phi_j^{(K)}(r,t)\right\}_j^{N_K}$, that are referred as *single-particle functions* (SPFs). The expansion is similar to the standard TDWP expansion (Eq. 2.9) except for the time dependence of the SPFs. This generalization allows to describe the evolution of the wavefunction with a much more compact expansion, thereby reducing the computation cost of the calculation.

The time evolution equations for the coefficients and the SPFs are usually derived using the Dirac-Frenkel variational principle. In particular, the working MCTDH equations are obtained with additional constraints in order to remove the ambiguity coming from the fact that both the expansion coefficients and the basis functions depend on time.

The advantage of MCTDH calculations is the possibility of adjusting the degree of correlation that is required in the description of the system. If we take just one SPF per degree of freedom, we obtain the *Time-Dependent Self-Consistent-Field* (TD-SCF) approximation, in which the wavefunction is approximated by a single Hartree product. In contrast to electronic structure calculation, TD-SCF usually gives results that are too poor even for a zero-th order description of the dynamics.

On the other hand, the increase of the number of SPFs per degree of freedom can lead us to the opposite limit, standard TDWP. Hence with MCTDH we can almost continuously switch from a very cheap but poor description to a highly accurate but expensive one.

Bibliography

[1] P. Hohenberg and W. Kohn, *Phys. Rev.* **136**, B864 (1964).

[2] W. Kohn and L. J. Sham, *Phys. Rev.* **140**, A1133 (1965).

[3] S. H. Vosko, L. Wilk and M. Nusair, *Can. J. Phys.* **58**, 1200 (1980).

[4] J. P. Perdew, K. Burke and M. Ernzerhof, *Phys. Rev. Lett.* **77**, 3865 (1996).

[5] B. Hammer, L. B. Hansen and J. K. Nørskov, *Phys. Rev. B* **59**, 7413 (1999).

[6] J. P. Perdew, J. A. Chevary, S. H. Vosko, K. A. Jackson, M. R. Pederson, D. J. Singh and C. Fiolhais, *Phys. Rev. B* **46**, 6671 (1992).

[7] A. D. Becke, *J. Chem. Phys.* **98**, 1372 (1993).

[8] R. Kosloff, *J. Phys. Chem.* **92**, 2087 (1988).

[9] D. O. Harris, G. G. Engerholm and W. D. Gwinn, *J. Chem. Phys.* **43**, 1515 (1965).

[10] A. S. Dickinson and P. R. Certain, *J. Chem. Phys.* **49**, 4209 (1968).

[11] J. C. Light, I. P. Hamilton and J. V. Lill, *J. Chem. Phys.* **82**, 1400 (1985).

[12] R. G. Littlejohn, M. Cargo, T. Carrington Jr., K. A. Mitchell and B. Poirier, *J. Chem. Phys.* **116**, 8691 (2002).

[13] R. G. Littlejohn and M. Cargo, *J. Chem. Phys.* **116**, 7350 (2002).

[14] D. Baye and P.-H. Heenen, *J. Phys. A - Math. Gen.* **19**, 2041 (1986).

[15] G. C. Corey and D. Lemoine, *J. Chem. Phys.* **97**, 4115 (1992).

[16] M. Feit, J. Fleck Jr. and A. Steiger, *J. Comput. Phys.* **47**, 412 (1982).

[17] H.-D. Meyer, U. Manthe and L. S. Cederbaum, *Chem. Phys. Lett.* **165**, 73 (1990).

[18] M. H. Beck, A. Jäckle, G. A. Worth and H.-D. Meyer, *Phys. Rep.* **324**, 1 (2000).

[19] H.-D. Meyer, F. Gatti and G. A. Worth, editors, *Multidimensional Quantum Dynamics: MCTDH Theory and Applications*, Wiley-VCH, Weinheim (2009).

Chapter 3

Eley-Rideal formation of H_2 on graphitic surfaces

3.1 Introduction

Hydrogen is the most abundant molecule detected in the interstellar medium (ISM), *e.g.* in dense and diffuse clouds and in photon-dominated regions, despite hydrogen molecules are continuously dissociated by stellar UV radiation and cosmic rays. An efficient catalytic route for the recombination of atomic hydrogen might take place on the surface of interstellar dust grains, an ensemble of very small particles of different sizes and nature [1–3]. In diffuse clouds, where the intense stellar radiation heats the gas, the largest particles are composed of a silicate core covered by an "organic refractory mantle", whereas smaller particles are entirely carbonaceous, being even simple Polycyclic Aromatic Hydrocarbons [4–6]. Hydrogen formation in these regions of interstellar space may thus occur on graphitic surfaces, and hydrogen-graphite has become the prototypical system for studying hydrogen formation in the ISM. Depending on the physical conditions of interest and on the actual morphology of the surface, a number of formation processes are possible, and only an accurate knowledge of adsorption, diffusion, and recombinative elementary acts allows one to investigate the role of each given pathway and to estimate the corresponding rate constant.

Hydrogen atoms may adsorb on graphitic surfaces either chemically or physically. Physisorbed atoms can only be found in cold environments, since they already desorb at few tens of Kelvins ($T_{des} \sim$ 30-40 K). Tunneling phenomena guarantee a high mobility of H atoms down to vanishing temperatures [7] and, generally, allow hydrogen molecules to form either through a Langmuir-Hinshelwood, or an Eley-Rideal, or a Hot-Atom mechanism, or a combination of them [8–10].

The chemisorption process is limited by a significant energy barrier to the sticking process [11–19]. In order to form a covalent bond between the approaching hydrogen atom and a carbon atom of the graphite (0001) surface, it is required that the carbon's sp^2 orbitals rehybridize to a tetrahedral sp^3 state. This process introduces a substantial lattice reconstruction, with one carbon atom moving out of the surface plane by about 0.35 Å, thereby causing a surface "puckering". As a consequence, a barrier to chemisorption $\sim$0.15 eV (1700 K) high appears, and essentially prevents (direct) hydrogen sticking in the chemisorption well at temperatures typical of the ISM (T = 10-100 K in diffuse clouds). For this reason, direct chemisorption of H atoms is expected to take place only in photon dominated or shocked regions where the temperature is high enough (T$\sim 200 - 1000$ K). Nevertheless, chemisorbed H atoms are required in order to explain the observed abundances and have been considered in many reaction mechanisms for hydrogen formation in the ISM.

Recent studies have shown that, due to the peculiar electronic structure of graphitic surfaces [20], H atoms tend to cluster already at very low coverages ($\leq$1%) [21–24]. Molecular formation at high temperatures may thus follow direct recombination of atoms within the clusters (in particular of hydrogen pairs lying in *para* position of an hexagonal ring [21]) and direct (Eley-Rideal) abstraction may occur on isolated atoms as well as on dimers [25]. In principle, chemisorbed hydrogen atoms can act as catalysts even at low temperature, *e.g. via* the barrierless adsorption of H atoms at their *para* position, followed by direct Eley-Rideal recombination of the latter [22, 25]. Langmuir-Hinshelwood reactions, however, are prevented by the lack of mobility of H

atoms chemically bound to the surface.

In this work, we focus on the H_2-forming, Eley-Rideal reaction involving a chemisorbed atom and for collision energies which reach the *cold* regime ($\sim 1 - 100$ K) where much of the chemistry of the ISM takes place. Many different methodologies and models have been developed to compute the cross section for this process [26–39] but a direct comparison between these studies is hard to perform since different researchers adopted different potential and/or dynamical models. Global differences are, however, already evident under simplified conditions and persist at any level of description. One of them is the behavior of the reaction probability in the collinear geometry when the substrate is kept rigid. As discussed in Ref. [39], some Potential Energy Surfaces (PES) give rise to a sizable reaction probability and to a resonant behavior in the whole energy range 0-0.5 eV [33], whereas others give rise to a smooth (almost free of resonances) decreasing probability as the energy decreases in the same range [39]. In addition, some authors found a tiny barrier ($\sim$ 10 meV or, equivalently, $\sim$ 100 K) in the entrance channel of the reaction and others do not. The existence of such a barrier, of course, has a deep impact on the reaction probability in the astrophysically relevant collision energy regime.

The aim of the present work is to systematically study how the reaction dynamics depends on the model adopted for the graphitic surface. We focus on the collinear reaction and consider how the Potential Energy Surfaces (PES) resulting from different substrate model give rise to different reaction probabilities. Clearly, such reduced dynamical models can only have limited value for the correct description of the title process (and many results concerning these models have been well-known since the birth of the chemical reaction dynamics), but the main focus here is on how the choice of the substrate affects the dynamics. An extension of the model is of course possible but for the present purposes it would be limited by the PES construction. We performed the simulations with quantum dynamical methods, since in the *low* energy regime typical of interstellar conditions the quantum behavior of

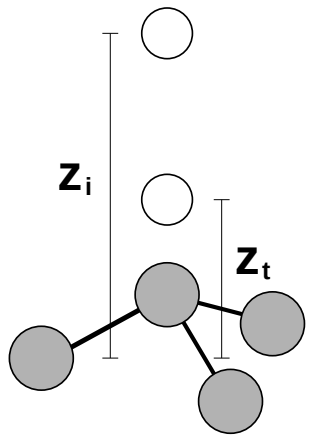

Figure 3.1: Coordinate system: z_i and z_t are the distances of the incident and target H atoms from the surface. The z coordinate of the nearest carbon atom $C_1$is either fixed in the puckered geometry ("sudden" model) or optimized at each position of the H atoms ("adiabatic" model).

H atoms cannot be neglected [39]. In addition we perform extensive *first-principles* calculations of the reaction energetics at different theory level, and definitely rule out the presence of any barrier in the entrance channel of the reaction.

This chapter is organized as follows: theoretical methods are presented in Section 3.2, results are given in Section 3.3, and conclusions in Section 3.4.

3.2 Methodology

The adopted dynamical model is a rigid surface model [40, 41] in the collinear geometry, in which the two H atoms lie along a line perpendicular to the surface. The last assumption does not allow us to determine the cross section, which is the relevant observable for the process. However, the reaction is essentially collinear dominated, and the computed collinear reaction probability can be used to get a clear indication on the reaction cross-sections at different collision energies of the incident H atom. The aim of this investigation is to see whether and how the adopted surface model impacts on the dynamical behavior of the system.

To describe the interaction of the two H atoms with the graphitic surface, we performed Density Functional Theory calculations with different models of the surface. First, we considered a cluster model of graphite (coronene molecule, $C_{24}H_{12}$), a Polycyclic Aromatic Hydrocarbon commonly used for this purpose [7, 15]. We computed the interaction energy with the Perdew-Burke-Ernzerhof (PBE) functional [42, 43] and Dunning's correlation consistent double ζ basis set (cc-pVDZ) [44], as implemented in GAUSSIAN code [45]. Second, we considered two different periodic models. In this case the graphitic surface is described with a 2x2 or 3x3 graphene supercell; inclusion of additional layers in a slab model does not modify the results significantly, as expected from the large interlayer separation in graphite ($\sim$ 3.4 Å). The total energy was computed with the PBE functional with the help of the VASP code [46] using a plane waves basis set (with a 500 eV cutoff) and a projector augmented wave (PAW) pseudopotential for core electrons [47, 48]. A vacuum space of 20 Å was placed between graphene layers in order to avoid periodic boundary conditions artifacts and a 15x15x1 Monkhorst-Pack grid of Γ-centered $\mathbf{k}$-points has been used to sample the Brillouin zone.

For each surface model, we considered two limiting dynamical regimes which try to include the lattice motion in the rigid setting [16, 33]. In the *sudden model* the position of the carbon atom involved in the C-H bond was kept fixed in the puckered geometry; in the (surface) *adiabatic model* the geometry of the carbon atom was optimized for each position of the two reacting H atoms. The first limit is appropriate in the high energy regime, where the reaction is faster than the lattice relaxation, whereas the latter is more adequate at low energies. It should be noticed, though, that neither model can fully take into account the effect of the carbon atom motion, that seems to actively promote the reaction [33].

For each of the six models described above (coronene cluster, 2x2 and 3x3 periodic supercell in the sudden and in the adiabatic regime) we computed 324 points of the PES as a function of the distances of the two H atoms from

the surface, z_i and z_t (Fig. 3.1), and used 2D splines to have continuous representations of the functions. We used the slope of the *ab-initio* data at the edge of the grid to fix the derivatives of the splines, and introduced continuously a long-range tail to the potential of the form $\sim z^{-4}$. The interpolation removes any ambiguity in the dynamics which might result from the choice of a fitting function and from the quality of the fitting, leaving us solely with the problem of the grid density, here chosen to be reasonable high for our purposes.

In the high energy range, we performed the dynamical simulation with a standard Time Dependent Wavepacket (TDWP) technique [36–38], whereas for the low energy regime we employed a novel two-wavepacket method [49], which has been recently implemented and tested in our group in 3D calculations of the reaction dynamics [39]. The latter method is designed to handle the dynamics at low energies, where the usual assumption of an initial wavepacket with only incoming momentum components breaks down. Briefly, in this approach two linearly independent, zero-momentum centered wavepackets are propagated in independent runs and the reaction probabilities are computed by properly combining the reaction amplitudes [49]. The latter are obtained by applying absorbing boundary conditions at the grid edges [50, 51] (*i.e.* at large z_i and z_t), here imposed by means of the transmission-free absorbing potentials of Manolopoulos [52].

With the present models, a time-*independent* quantum dynamical approach would be more convenient, especially at low energy, where such an approach proved indeed to be superior in efficiency and accuracy. However, in further developments of this work we aim at extending the dynamical model to include more degrees of freedom, up to eventually those of the lattice, and for such high-dimensional quantum problems (either exact or approximate) time-*dependent* wavepacket approaches are the only viable alternative.

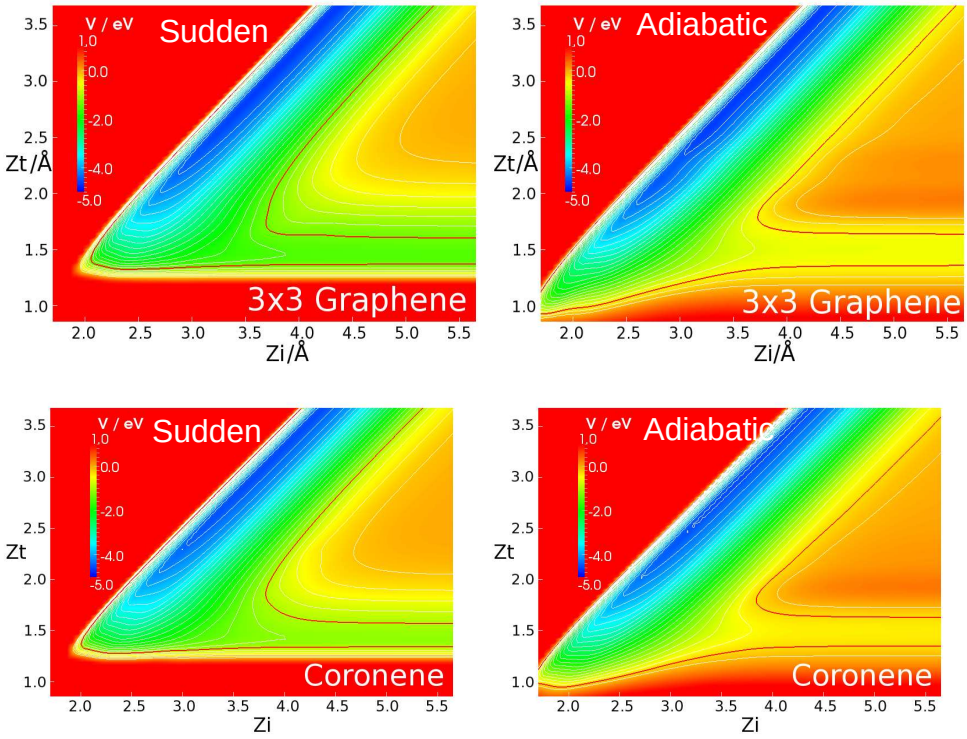

Figure 3.2: Contour plots of the 3x3 periodic (top) and coronene (bottom) PES for the sudden (left) and the adiabatic (right) regimes. Potential is shown as a function of the height of the incident (z_i) and target (z_t) H atoms. The thick red line marks the energy of the vibrational ground state of the target H atom. Other contour lines have been plot every 0.2 eV with respect to this vibrational energy. The zero of the energy corresponds to both the H atoms in the gas phase.

3.3 Results and Discussion

3.3.1 Potential energy surfaces

Our potential energy surfaces (see Fig. 3.2 for an overview) show that H_2 Eley-Rideal formation is a *non-activated*, exothermic reaction. No barrier could be found along the minimum energy path in any of the models considered in this work, at variance with previous cluster calculations with a coronene model which reported a barrier 10 meV high in the entrance channel [10, 33]. We systematically analyzed if such a tiny barrier could arise by using differ-

ent functionals or basis sets, investigating the same coronene model in both dynamical regimes (sudden and adiabatic). In addition to the PBE functional adopted for the dynamics, we used the Perdew-Wang 1991 functional (PW91) used in Ref. [33], both in conjunction with several Dunning's correlation-consistent basis-sets, up to quadruple-ζ. The results are reported in Fig. 3.3 as functions of the distance of the incident H atom from the surface, in the region where the barrier is expected. It is evident from the graph that the energy monotonically decreases from the asymptotic to the interaction region, leaving no room for a barrier at increasing basis-set level. Similarly, we exclude the presence of the barrier in the periodic models.

Apart from the barrier, the computed PES agrees well with those computed by other authors. In both the adiabatic and the sudden models the entrance channel goes smoothly into the deep exit channel where the H_2 molecule forms. However, there are differences between the two dynamical regimes. First of all, the adiabatic reaction is more exothermic than the other, since the puckering energy is released as the H_2 molecule leaves the surface. Secondly, in the adiabatic model the target H atom is allowed to get nearer to the surface, since the position of the carbon atom beneath is relaxed at each geometry. This determines a different *curvature* of the elbow potential which, as we will see in the following, plays a major role in determining the reaction dynamics. On the other hand, within the same dynamical regime, we hardly see any difference - at least at the energy scale of Fig. 3.2- between the surface models adopted; in particular, at this same scale, the results for the 2x2 periodic model (not reported) cannot be distinguished from those of the 3x3 periodic model. Differences only appear in the dynamical results.

3.3.2 Quantum dynamical results

Sudden models. Fig. 3.4 shows the results of the quantum dynamical calculations for the three sudden models. In this calculation the H target atom is initially in the vibrational ground state, the only one accessible in the relevant astrophysical conditions. Though the results for the low and high energy

regimes are shown on different scales, there is a perfect matching between the curves where both results - ordinary wavepacket and two-wavepacket ones - are available.

In addition to the dynamical results obtained with the PES described above, we have reported previous results obtained with the London-Eyring-Polanyi-Sato (LEPS) potential fitted by Sha et al. to DFT periodic calculations on the 2x2 unit cell of graphene [16]. The calculations based on this LEPS potential describe the overall trend of the reaction probability but completely miss the fine structure that can be found in each of our calculations. This particular feature, already reported in the collinear calculations by Morisset et al. [33], is due to Feshbach resonances, *i.e.* the formation of short lived vibrationally-excited species in asymptotically closed vibrational levels that become open at low energies.

This is supported by the comparison of the results for different vibrational states. The reaction probability for different initial states of the target H atom

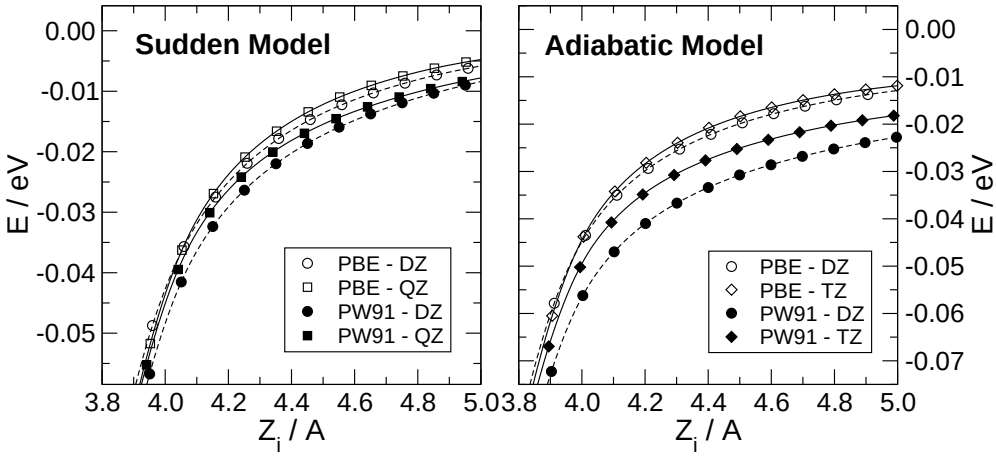

Figure 3.3: Minimum energy path as a function of the height of the incident H atom, in the region where the presence of a barrier has been reported. We computed the energy with PW91 (solid symbols) and PBE functionals (empty symbols), for different Dunning's basis sets and both the dynamical regimes (sudden in the left panel and adiabatic in the right panel). We took as reference the energy of one H atom adsorbed on the surface and the other at infinite distance.

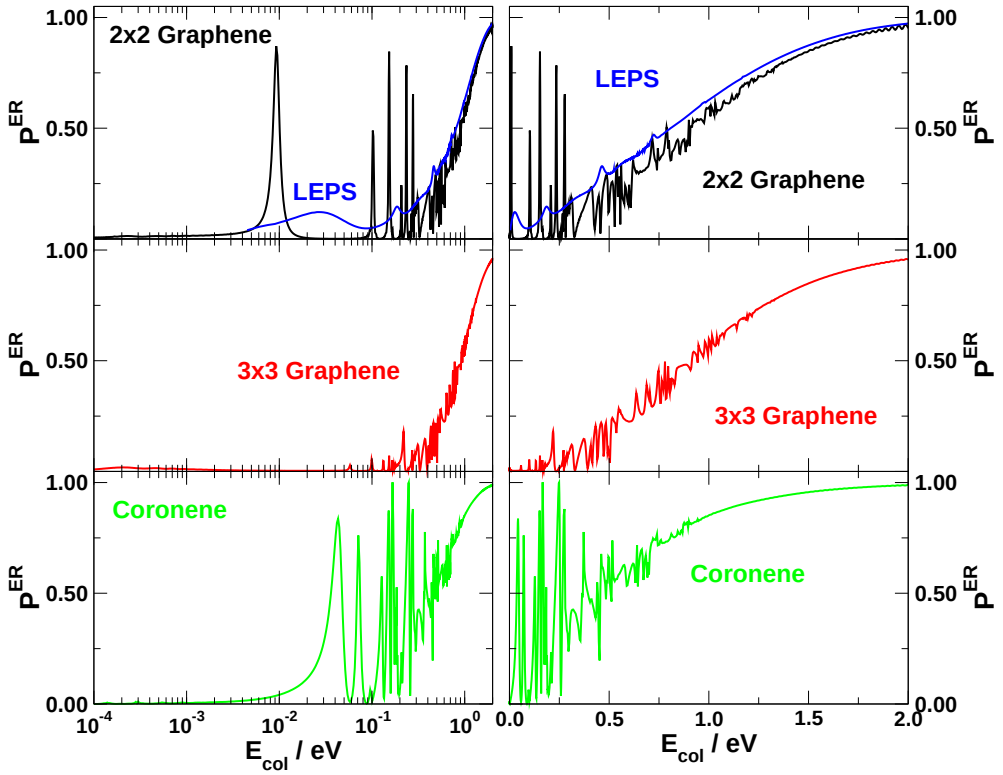

Figure 3.4: Eley-Rideal, quantum reaction probability for the three sudden models with the reagents in the lowest vibrational state, for low energies (left panels, logarithmic scale from $10^{-4}eV \approx 1K$ to $1eV \approx 10,000K$) and at high energy on a linear scale (right panels). Green line for coronene, red for 3x3 graphene, black for 2x2 graphene, and blue for the LEPS PES of Sha *et al.* [16].

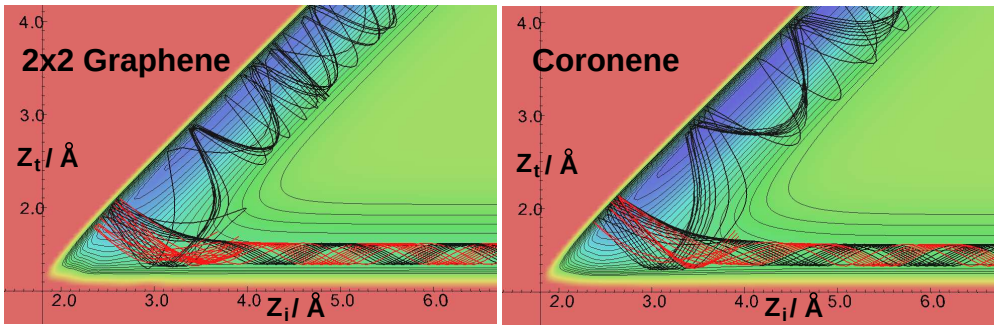

Figure 3.5: Reactive (black) and non reactive (red) classical trajectories for the 2x2 graphene and coronene sudden models are shown as a function of the incident (z_i) and target (z_t) heights from the surface.

is plotted in Fig. 3.6 as a function of the total energy of the system, for the Coronene and the 2x2 periodic models. The fine structures of the curves are similar: even if the peaks have different intensities, they are located at the same total energy values, corresponding to the energies of the resonant states. This structure is connected in a complex way to the vibrational states of the reaction channels and the peaks cluster near the energies of the vibrational levels of both the products and the reagents.

For each of the model potentials we considered, the reaction probability decreases with the collision energy, in agreement with previous calculations [33, 37, 39]. None of the PES gives rise to a substantial reaction probability in the astrophysically relevant energy range ($10^{-3} - 10^{-2}$ eV) - except for a sharp resonance peak for the coronene PES located at 10^{-2} eV. As previously discussed, all the potential energy surfaces considered in the present study do not include any barrier in the entrance channel. Hence the results show that the low energy behavior is entirely due to quantum reflection.

In the high energy regime, the reaction probability for periodic and cluster models has a similar behavior, but the coronene potential gives a consistently higher reaction probability than the periodic ones, as evidenced by a comparison between the (smoothed) probability curves shown in Fig. 3.7 (upper panel) over a broad energy interval. Here smoothing has been accomplished by averaging each computed data in a narrow energy range to highlight the global behaviour which is masked by the resonance structure. The differences are due to a simple classical effect connected to the shape of the elbow in an otherwise simple, exoergic process. To investigate this point, we computed a set of classical trajectories, which are reported in Fig. 3.5. These classical calculations were performed for the same sudden model, for coronene and the 2x2 periodic lattice models. At the beginning of these trajectories, the target H atom oscillates with an energy corresponding to its quantum ground state energy whereas the incident H atom approaches the surface with a kinetic energy of 0.5 eV in the collinear geometry. We sampled uniformly the initial position of the target atom to get insights into the reaction dynamics, as

shown by plotting the reactive trajectories. No attempt was made to compute reaction probabilities from QCT calculations, since the reliability of classical dynamics was already considered in our previous works [36, 37, 39].

Most reactive trajectories share the very same "two bounce" mechanism. First the incident H atom collides with the target H atom and is pushed back. This corresponds to the first bounce of the trajectory, that is reflected by the H-H repulsion. In this first collision, some momentum is transferred between the two hydrogen atoms and the target atom moves towards the surface. Then the target atom collides with the surface which triggers the system to the products channel, where the two H atoms leave the surface in a highly excited vibrational state.

From the graph of Fig. 3.5 it is clear that in all the reactive trajectories the phase of the vibration of the target atom is similar. This suggests that the reaction mechanism is possible just for a particular interval of vibrational phases. For these vibrational phases, the system is reflected in the way described above by the two repulsive walls and driven to the products channel. In light of this, the difference between the periodic and the cluster models is that the phase interval of the reactive trajectories is broader for the coronene than the periodic model, suggesting the the former potential drives the hydrogen atoms towards the products in a more effective way.

Adiabatic models. The reaction probability for the different surface model in the adiabatic case are represented in Fig. 3.8 as functions of the kinetic energy of the incident atom, in the low and high energy regimes. As for the sudden case, the high energy results have been obtained with ordinary wavepacket techniques, whereas the low energy curves were computed with the two-wavepacket approach. Also in this case, the target H atom is initially in the vibrational ground state.

Apart from the missing resonance structure, in this case the LEPS potential model fails to reproduce the overall trend of the curve and it highly underestimates the reaction probability for collision energy lower than 1.0 eV, thereby

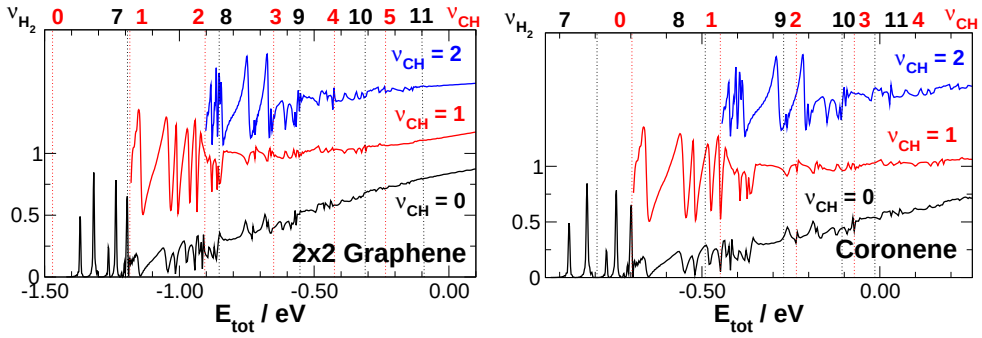

Figure 3.6: Analysis of the resonance structure of the reaction probability for the 2x2 periodic and cluster sudden models. Reaction probabilities for different initial vibrational state ν of the target H atom are reported as functions of the total energy. For convenience the curves for $\nu = 1, 2$ have been shifted along the y axis . Dotted vertical lines mark the energies of the vibrational states of the reacting C-H bond (red) and product H_2 molecule (black). The energies of the first two vibrational quanta of the C-H bond are: 0.29 eV and 0.56 eV (for the 2x2 graphene), 0.28 eV and 0.53 eV (for the coronene).

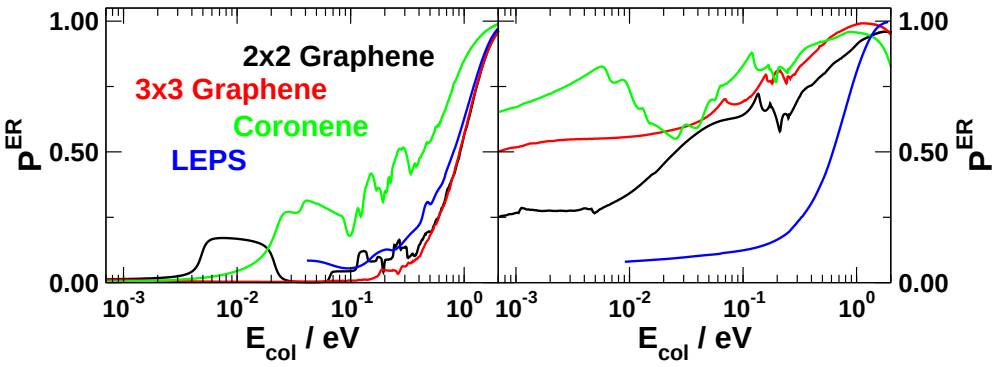

Figure 3.7: Comparison between reaction probability, properly smoothed as described in the main text. Left and right panels for the sudden and adiabatic models.

showing that the LEPS form is not flexible enough to fully describe the interaction potential in the adiabatic case.

In the high energy regime, all our surface models predict the reaction probability with a reasonable qualitative agreement. For collision energy below 0.5 eV, all the curves show sharp resonance peaks, that are particularly similar for the periodic models. In this energy range the reaction probability for coronene is higher than for the 3x3 graphene, that in turn is higher than for the 2x2 graphene, as evidenced in the smoothed data shown in the right panel of Fig. 3.7.

In any case, the reaction probability increases up to 1.0 eV and then starts to decrease, due to the competing Collision Induced Desorption (CID) process [37, 38]. In the energy range considered in this work, the CID channel is closed for the sudden model, but open for adiabatic models. In the latter case, in fact, the puckering energy is implicitly released during the dissociation of the target atom. The adiabatic models are approximately 0.9 eV more exothermic than the corresponding sudden ones and the CID channel for the adiabatic PES opens at lower collision energies.

Comparing the graphs in Fig. 3.4 and Fig. 3.8, we see that before saturation is reached, the reaction probability is much higher in the adiabatic limit than in the sudden one. This can be simply explained by computing some classical trajectories with the same initial conditions described above. The reactive trajectories for a collision energy of 0.5 eV in the case of the adiabatic 2x2 graphene PES are reported in Fig. 3.9. As can be seen, a similar "two-bounce" mechanism as the one described above is operating here. The difference here is the curvature of the surface-target atom repulsive wall that drives more effectively the system towards the products channel. Hence the implicit model of surface motion statically affects the reaction by changing the PES shape and making H_2 formation easier.

In the low energy regime the reaction probability decreases with decreasing collision energy as in the sudden model. However, the reaction probability is different from zero in the astrophysically relevant low energy range.

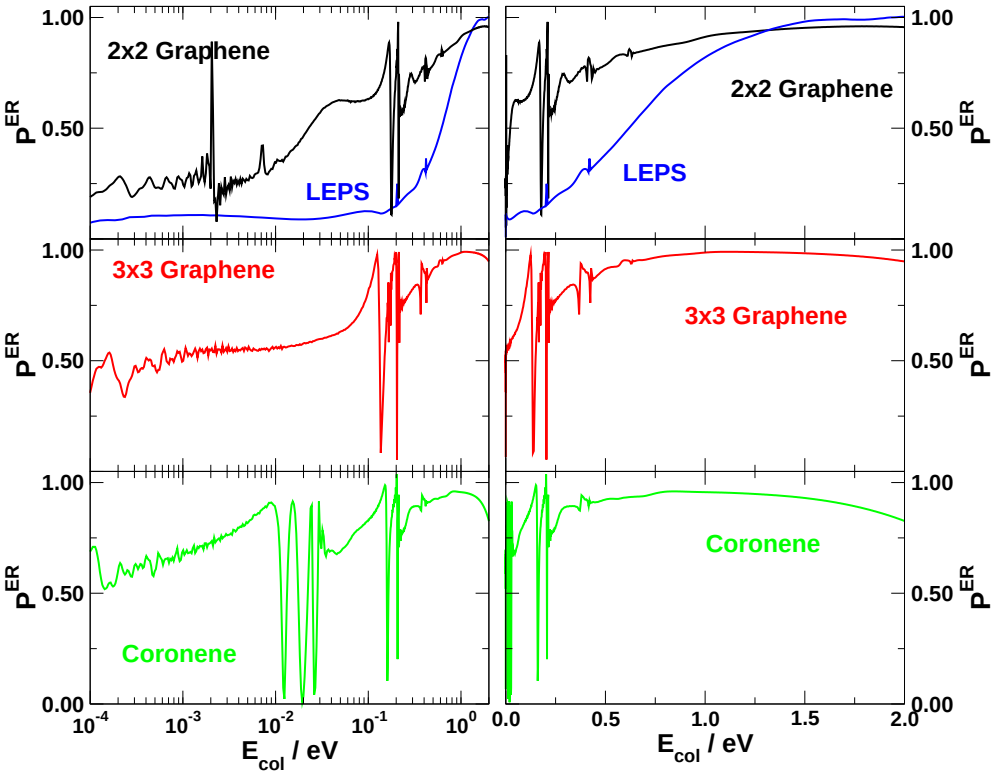

Figure 3.8: Eley-Rideal, quantum reaction probability for the three adiabatic models with the reagents in the lowest vibrational state, for low energies (left panels, logarithmic scale from $10^{-4}eV \approx 1K$ to $1eV \approx 10,000K$) and at high energy on a linear scale (right panels). Green line for coronene, red for 3x3 graphene, black for 2x2 graphene, and blue for the LEPS PES of Sha *et al.* [16].

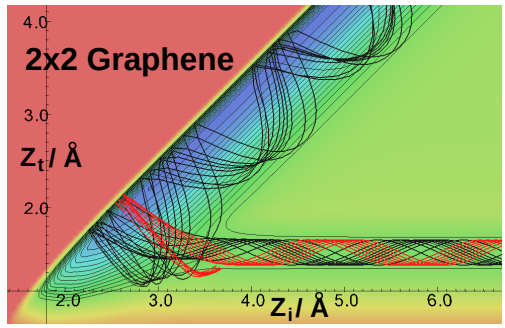

Figure 3.9: Reactive (black) and non reactive (red) classical trajectories for the 2x2 graphene adiabatic models are shown as a function of the incident (z_i) and target (z_t) heights from the surface.

As for the high energy results, the reaction probability for coronene is higher than the probability for graphene, while among the periodic models, the 3x3 surface is more reactive than the 2x2 one. [Notice here that undulating features in the curve appear because of the presence of very sharp (long-lived) resonances which would require extremely long propagation times to be resolved]. In this energy range, the reflected fraction of the wavepackets is much smaller in the adiabatic regime than in the sudden one. This marked difference in the quantum behaviour of the system is probably related to the curvature of the entrance channel: in the adiabatic models the potential changes smoothly from the entrance to the exit channel, whereas in the sudden case this transition is steeper and this increases the chance that the wavepacket is reflected back.

3.4 Conclusions

In the work presented in this chapter, we computed quantum reaction probability for the collinear Eley-Rideal formation of H_2 over a broad range of collision energies, including the low energy regime relevant for the chemistry of the interstellar medium. In particular we investigated whether and how the dynamics of the system depends on the model adopted for the description of the surface. In light of this, we also addressed the problem of the presence of a tiny energy barrier in the entrance channel which was found by different authors [10, 33]. We found that the minimum energy path is monotonically decreasing at any level of theory (in particular, basis-set size), and this strongly suggests that the title reaction is *barrierless*.

Concerning the dynamical results, we found that the results markedly depends on the choice of the model. While this is expected in the low energy regime, where the dynamics is very sensitive to the details of the potential, we found it to be true also at high collision energies. Under such circumstances, we found that when the same limiting approach is followed to describe the motion of the carbon atom - sudden or adiabatic - the results are qualitatively

consistent but on quantitative grounds differences appear, the reaction probability being higher for the cluster model than for the periodic models. This is particularly true for the sudden models, but also holds to some extent for the adiabatic models. The reason of this discrepancy is the different shape of the entrance channel, that seems to play a major role in determining the reaction probability. Even a slight modification in the interaction potential - such as the difference between the 3x3 and coronene PESs - might drive the system more effectively towards the products, resulting in a higher reaction probability, see Fig. 3.7.

In agreement with previous studies, in the low energy regime we found that for all the models considered the reaction probability tends to zero with decreasing collision energy. This limiting behaviour can only be due to quantum reflection since, as stated above, our potential energy surfaces turn out to be barrierless. The efficiency of quantum reflection, on the other hand, is strongly dependent on the choice of the model, too. In the sudden regime, the whole wavepacket is reflected back to the entrance channel for any energy lower than $10^{-2}\,eV$ (100 K). If this were the case, we could reasonably assume that no reaction would take place in the astrophysical conditions. On the other hand, in the adiabatic regime, the probability vanishes only at much lower energies, thereby leaving open the possibility that a model including *dynamically* the motion of the carbon atom might give a reasonably sized probability in this energy regime. Also in this case, differences are found from model to model; for instance, the reaction probability for 2x2 graphene is 2-3 times higher than for 3x3 graphene in the $10^{-4} - 10^{-2}$ eV range, see Fig. 3.7. From such discrepancy, we expect a similar factor for the corresponding reaction cross sections, when we move to three dimensional models.

In conclusion, moving to a less simplified and more realistic higher dimensional dynamical approach does require a careful choice of the substrate model used to build the PES. If the aim is to obtain the probabilities (cross-sections) for the reaction on graphite, then a large supercell approach seems to be necessary (maybe even larger than 3x3), especially in the limit where

the carbon atom follows adiabatically the hydrogen evolution. In this respect, the above results suggest that modeling graphite (graphene) with a coronene molecule, despite many appealing features, is inadequate for investigating the present process. To this we add that while some features of the rigid-flat surface approximation are appropriate for this system (*e.g.* the rotational invariance of the interaction) the motion of the carbon atom needs likely to be explicitly included in the dynamical treatment (see also Ref. [33]). This defines a "minimal" 4D (quantum) model, and a corresponding interaction potential at the level outlined above. Work is currently in progress in order to set up such a model.

The results presented in this chapter are reported in the following publication:

M. Bonfanti, S. Casolo, G. F. Tantardini and R. Martinazzo,
"Surface models and reaction barrier in Eley-Rideal formation of H_2 on graphitic surfaces"
Phys. Chem. Chem. Phys., **13**, 16680-16688 (2011)

Bibliography

[1] R. J. Gould and E. E. Salpeter, *Astrophys. J.* **138**, 393 (1963).

[2] D. Hollenbach and E. E. Salpeter, *J. Chem. Phys.* **53**, 79 (1970).

[3] D. Hollenbach and E. E. Salpeter, *Astrophys. J.* **163**, 155 (1971).

[4] J. M. Greenberg, *Surf. Sci.* **500**, 793 (2002).

[5] D. A. Williams and E. Herbst, *Surf. Sci.* **500**, 823 (2002).

[6] B. T. Draine, *Annu. Rev. Astron. Astrophys.* **41**, 241 (2003).

[7] M. Bonfanti, R. Martinazzo, G. F. Tantardini and A. Ponti, *J. Phys. Chem. C* **111**, 5825 (2007).

[8] S. Morisset, F. Aguillon, M. Sizun and V. Sidis, *J. Chem. Phys.* **121**, 6493 (2004).

[9] S. Morisset, F. Aguillon, M. Sizun and V. Sidis, *J. Chem. Phys.* **122**, 194702 (2005).

[10] D. Bachellerie, M. Sizun, F. Aguillon and V. Sidis, *J. Phys. Chem. A* **113**, 108 (2009).

[11] T. Zecho, A. Güttler, X. Sha, B. Jackson and J. Küppers, *J. Chem. Phys.* **117**, 8486 (2002).

[12] A. Güttler, T. Zecho and J. Küppers, *Chem. Phys. Lett.* **395**, 171 (2004).

[13] A. Güttler, T. Zecho and J. Küppers, *Surf. Sci.* **570**, 218 (2004).

[14] T. Zecho, A. Güttler and J. Küppers, *Carbon* **42**, 609 (2004).

[15] L. Jeloaica and V. Sidis, *Chem. Phys. Lett.* **300**, 157 (1999).

[16] X. Sha and B. Jackson, *Surf. Sci.* **496**, 318 (2002).

[17] J. Kerwin, X. Sha and B. Jackson, *J. Phys. Chem. B* **110**, 18811 (2006), pMID: 16986871.

[18] Y. Ferro, F. Marinelli and A. Allouche, *Chem. Phys. Lett.* **368**, 609 (2003).

[19] J. Kerwin and B. Jackson, *J. Chem. Phys.* **128**, 084702 (2008).

[20] S. Casolo, O. M. Lovvik, R. Martinazzo and G. F. Tantardini, *J. Chem. Phys.* **130**, 054704 (2009).

[21] L. Hornekær, Ž. Šljivančanin, W. Xu, R. Otero, E. Rauls, I. Stensgaard, E. Lægsgaard, B. Hammer and F. Besenbacher, *Phys. Rev. Lett.* **96**, 156104 (2006).

[22] L. Hornekær, E. Rauls, W. Xu, Ž. Šljivančanin, R. Otero, I. Stensgaard, E. Lægsgaard, B. Hammer and F. Besenbacher, *Phys. Rev. Lett.* **97**, 186102 (2006).

[23] L. Hornekær, W. Xu, R. Otero, E. Lægsgaard and F. Besenbacher, *Chem. Phys. Lett.* **446**, 237 (2007).

[24] A. Andree, M. L. Lay, T. Zecho and J. Küppers, *Chem. Phys. Lett.* **425**, 99 (2006).

[25] N. Rougeau, D. Teillet-Billy and V. Sidis, *Chem. Phys. Lett.* **431**, 135 (2006).

[26] A. J. H. M. Meijer, A. J. Farebrother, D. C. Clary and A. J. Fisher, *J. Phys. Chem. A* **105**, 2173 (2001).

[27] A. J. H. M. Meijer, A. J. Farebrother and D. C. Clary, *J. Phys. Chem. A* **106**, 8996 (2002).

[28] A. J. H. M. Meijer, A. J. Fisher and D. C. Clary, *J. Phys. Chem. A* **107**, 10862 (2003).

[29] M. Rutigliano, M. Cacciatore and G. D. Billing, *Chem. Phys. Lett.* **340**, 13 (2001).

[30] M. Rutigliano and M. Cacciatore, *ChemPhysChem* **9**, 171 (2008).

[31] B. Jackson and D. Lemoine, *J. Chem. Phys.* **114**, 474 (2001).

[32] S. Morisset, F. Aguillon, M. Sizun and V. Sidis, *Phys. Chem. Chem. Phys.* **5**, 506 (2003).

[33] S. Morisset, F. Aguillon, M. Sizun and V. Sidis, *J. Phys. Chem. A* **108**, 8571 (2004).

[34] D. Bachellerie, M. Sizun, F. Aguillon, D. Teillet-Billy, N. Rougeau and V. Sidis, *Phys. Chem. Chem. Phys.* **11**, 2715 (2009).

[35] M. Sizun, D. Bachellerie, F. Aguillon and V. Sidis, *Chem. Phys. Lett.* **498**, 32 (2010).

[36] R. Martinazzo and G. F. Tantardini, *J. Phys. Chem. A* **109**, 9379 (2005).

[37] R. Martinazzo and G. F. Tantardini, *J. Chem. Phys.* **124**, 124702 (2006).

[38] R. Martinazzo and G. F. Tantardini, *J. Chem. Phys.* **124**, 124703 (2006).

[39] S. Casolo, R. Martinazzo, M. Bonfanti and G. F. Tantardini, *J. Phys. Chem. A* **113**, 14545 (2009).

[40] M. Persson and B. Jackson, *J. Chem. Phys.* **102**, 1078 (1995).

[41] D. Lemoine and B. Jackson, *Comput. Phys. Commun.* **137**, 415 (2001).

[42] J. P. Perdew, K. Burke and M. Ernzerhof, *Phys. Rev. Lett.* **77**, 3865 (1996).

[43] J. P. Perdew, K. Burke and M. Ernzerhof, *Phys. Rev. Lett.* **78**, 1396 (1997).

[44] T. H. Dunning, *J. Chem. Phys.* **90**, 1007 (1989).

[45] M. J. Frisch, G. W. Trucks, H. B. Schlegel, G. E. Scuseria, M. A. Robb, J. R. Cheeseman, J. J. A. Montgomery, T. Vreven, K. N. Kudin, J. C. Burant, J. M. Millam, S. S. Iyengar, J. Tomasi, V. Barone, B. Mennucci, M. Cossi, G. Scalmani, N. Rega, G. A. Petersson, H. Nakatsuji, M. Hada, M. Ehara, K. Toyota, R. Fukuda, J. Hasegawa, M. Ishida, T. Nakajima, Y. Honda, O. Kitao, H. Nakai, M. Klene, X. Li, J. E. Knox, H. P. Hratchian, J. B. Cross, V. Bakken, C. Adamo, J. Jaramillo, R. Gomperts, R. E. Stratmann, O. Yazyev, A. J. Austin, R. Cammi, C. Pomelli, J. W. Ochterski, P. Y. Ayala, K. Morokuma, G. A. Voth, P. Salvador, J. J. Dannenberg, V. G. Zakrzewski, S. Dapprich, A. D. Daniels, M. C. Strain, O. Farkas, D. K. Malick, A. D. Rabuck, K. Raghavachari, J. B. Foresman, J. V. Ortiz, Q. Cui, A. G. Baboul, S. Clifford, J. Cioslowski, B. B. Stefanov, G. Liu, A. Liashenko, P. Piskorz, I. Komaromi, R. L. Martin, D. J. Fox, T. Keith, M. A. Al-Laham, C. Y. Peng, A. Nanayakkara, M. Challacombe, P. M. W. Gill, B. Johnson, W. Chen, M. W. Wong, C. Gonzalez and J. A. Pople, 'Gaussian 03, Revision C.02,' (2004), Gaussian, Inc., Wallingford, CT.

[46] G. Kresse and J. Furthmüller, *Comput. Mat. Sci.* **6**, 15 (1996).

[47] P. E. Blöchl, *Phys. Rev. B* **50**, 17953 (1994).

[48] G. Kresse and D. Joubert, *Phys. Rev. B* **59**, 1758 (1999).

[49] R. Martinazzo and G. F. Tantardini, *J. Chem. Phys.* **122**, 094109 (2005).

[50] D. Neuhasuer and M. Baer, *J. Chem. Phys.* **90**, 4351 (1989).

[51] D. Neuhauser and M. Baer, *J. Chem. Phys.* **91**, 4651 (1989).

[52] D. E. Manolopoulos, *J. Chem. Phys.* **117**, 9552 (2002).

Chapter 4

H_2 dissociation on Cu(111)

4.1 Introduction

The correct prediction of elementary processes occurring when H_2 scatters from a metal surface is one of the main challenges in the field of heterogeneous catalysis. The reactive scattering of H_2 from Cu(111) has often been used as prototype system. This is because of three reasons. First, a wide range of experimental results is available for this system [1–11]. Second, many theoretical studies modeling a limited number of H_2 degrees of freedom have been performed with the aim of clarifying the mechanisms underlying the reactive scattering [12–19]. Third, quantum dynamics calculations on reactive scattering modeling all degrees of freedom are possible [20, 21], and have been used to achieve qualitative [21–24] and quantitative [25–27] comparisons with experiments on H_2 + Cu(111), based on DFT potential energy surfaces [25, 28, 29].

Recently six dimensional quantum dynamical calculations [25, 26] have reproduced reaction probabilities measured in molecular beam experiments [1, 3, 7], initial-state resolved dissociation probabilities inferred from associative desorption experiments [5, 7], and data on rotationally inelastic scattering [10] with chemical accuracy. The key idea of this work was to compute the interaction of $H_2(D_2)$ with Cu(111) using the Specific Reaction Parameter (SRP) approach to DFT [30]. In the implementation of the SRP-DFT method

used, the exchange-correlation functional is computed as a weighted average of suitable GGA functionals. Adjusting the mixing coefficient to reproduce D_2/ Cu(111) molecular beam experiments on the dependence of reaction on incidence energy [3], a reliable 6D Potential Energy Surface (PES) was obtained.

As most of the dynamical simulations of H_2-metal surface scattering so far, the work assumed a static surface and no electron-hole pair excitation. The calculations suggest [26] that some refinements of the dynamical model are still needed to get a proper description of the rotational quadrupole alignment parameter of reacting D_2 [9], and of vibrationally inelastic scattering of H_2 [6]. For these two observables, quantitative agreement with experiment has not yet been obtained. However, the rotational quadrupole alignment parameter has been measured at high surface temperature (T_S= 925 K), and it is not yet known how this parameter depends on T_S. Furthermore, there is some evidence that vibrationally inelastic scattering could be promoted by the exchange of energy with the surface in a way that depends on T_S [26, 31], and the height of the "vibrational excitation peak" in the time-of-flight experiments of Ref. [6] depends on the amount of energy lost to the surface by H_2 [26]. These considerations suggest that for these scattering phenomena a better agreement can perhaps be achieved by including some lattice degrees of freedom in the dynamical model.

In the past, experimental studies have proved that the sticking probability has a characteristic dependence on the surface temperature [2, 11]. In particular it has been shown that the effective barrier E_0 is, to a good approximation, independent of T_S, whereas the width parameter W that determines the steepness of the curve increases with T_S. Quantum dynamical simulations [31–33] have shown that this behavior is qualitatively consistent with a thermal population of a surface vibrational degree of freedom.

The inclusion of substrate atom motion in gas-surface dynamics is not a trivial task. Various models have been developed to introduce these effects at least at a qualitative level. The most popular of these models is the Surface

Oscillator (SO) model, originally proposed by Hand and Harris [34]. In this simple one dimensional description of the surface, an oscillator is coupled to the molecular coordinates to describe the mechanical recoil of the surface atoms due to the collision with the incoming particle. This model and some related variants have been applied to a variety of systems: H_2 and D_2 on Cu or other transition metals [31–36], N_2 on Fe [34], CH_4 on Ni and Pt [37–39].

The inclusion of a surface degree of freedom in the SO model broadens the reaction probability curve and shifts its midpoint (E_0) to a slightly higher energy. This shift is strongly dependent on the mass of the incident particle. In particular, the effect is very small for scattering and dissociative chemisorption of H_2 [33]. In D_2 / Cu(111) reactive scattering, Díaz et al. [26] have applied an appropriate correction based on the SO model and found a small decrease of the rotational quadrupole alignment parameter. Even if this adjustment improves the agreement with the experiment, it is not sufficient to get the desired quantitative accuracy. The inclusion of the lattice motion based on an improved model seems therefore worthy of exploration.

Another model was proposed in the past by Dohle and Saalfrank [33], who developed the Modified Surface Oscillator (MSO) model, which tries to capture effects which are not reproduced by the SO model. In the MSO model the barrier along the reaction path may become larger or smaller depending on the phonon coordinate. The inclusion of this model also leads to a broadening and a shift of the reaction probability curve. Unlike the SO model, however, in the MSO model the curve is shifted to lower energies.

More recently Jackson and co-workers [39, 40] have extensively studied the PES for CH_4 / Ni and CH_4 / Pt with Density Functional Theory (DFT), displaying the dependence of the features of the PES - dissociation barrier geometry and height - on the motion of the nearest metal atom. Dynamics calculations performed by them showed that both the change in barrier height and the displacement of the barrier affect the reaction probabilities, but only the latter can be reproduced by the SO model. Tiwari et al. [40] showed that in the case of CH_4 / Ni a Sudden Approximation works well. The idea of

this approach is to compute the scattering probability as an average of the probabilities computed by fixing the lattice atom in different positions. This accounts for the "static" effect of the surface displacement, without allowing any exchange of energy between the molecule and the surface.

Another very interesting approach to include the vibrations of the lattice in the dynamical simulations was developed by Billing and Adhikari [41–43]. In this semiclassical method, the effect of the phonons is modeled through an effective "mean-field" potential added to the Hamiltonian. In this way, it is possible to include many possible effects of the phonons, as long as the dependence of the potential on the lattice degrees of freedom is known.

The goal of the work presented in this chapter is to make a systematic analysis of the direct influence of the motion of the lattice atoms on the interaction of $H_2(D_2)$ with Cu(111). To have an idea of the possible effects on the reactive scattering, we also compare our results to some simple available models for the coupling of the lattice to the molecular coordinates. Our purpose is to identify how the reaction coordinate for H_2 dissociation is coupled to the lattice vibrations. This preliminary picture will give us some criteria to predict which lattice degrees of freedom are likely to play a major role in the reaction dynamics. The actual quantification of these effects through dynamics studies will be possibly addressed in future work.

This chapter is subdivided as follows. In section 4.2 we describe the theoretical methods used in the present work. The results are shown and discussed in section 4.3. Finally, conclusions are presented in section 4.4.

4.2 Methodology

Our approach has been to analyze how the motion of different surface Cu atoms of Cu(111) affects the H_2 dissociation barrier geometry and the barrier height. To represent the motion of the surface, we chose a few localized surface degrees of freedom: the displacement of a 1^{st} layer copper atom in the direction perpendicular to the surface ($Q_1^{\perp}$) and parallel to the surface ($Q_1^{\parallel}$),

the displacement of a 2^{nd} layer Cu atom in both the perpendicular and parallel direction ($Q_2^{\perp}$ and $Q_2^{\parallel}$), and the perpendicular displacement of a 3^{rd} layer Cu atom ($Q_3^{\perp}$). When H_2 is near the surface, in each layer it is possible to choose different Cu atoms. The criterion followed in this case was to displace the Cu atom (or one of the Cu atoms) which is nearest to the H_2 center of mass.

With respect to the hydrogen molecule's position, we considered a set of barriers in the (r, Z, ϑ) coordinates, each corresponding to a representative (X, Y, φ) configuration of H_2 (Fig. 4.1). In each of these configurations the H_2 center of mass is above one of the high symmetry points of the (111) surface: top, bridge, hcp (hollow, above a 2^{nd} layer Cu), fcc (hollow, above a 3^{rd} layer Cu), t2h (halfway between top and hcp) or t2f (halfway between top and fcc). In each case, the angular coordinate φ was chosen to get the lowest barrier for the ideal frozen surface. In some interesting cases the angular dependence of the barrier was also studied.

The set of dissociation geometries investigated is schematically depicted in Fig. 4.1. We identify them in two different ways. For some barrier geometries (e.g. BtH "bridge to hollow") we use a three letter abbreviation, the first capital letter indicating the position of the center of mass and the second the surface high symmetry points towards which the H-H bond is oriented. In other cases (e.g. t2h(120°)), we use the name of the high symmetry impact site and we specify the orientation by the φ angle in parentheses.

For each (X, Y, φ) configuration, the dissociation geometry (Z_b, r_b, ϑ_b) and the height of the barrier E_b were computed by locating the transition state for that fixed configuration. Fixing X, Y, φ and a surface geometry, DFT was employed to compute the electronic energy on a (r, Z, ϑ) grid. These points were interpolated with a 3D spline function and the transition state was located with a Newton-Raphson optimization technique based on numerical gradients and hessians.

DFT calculations were carried out with DACAPO [44]. To accurately reproduce the energetics of the H_2 / Cu(111) interaction the SRP-DFT method

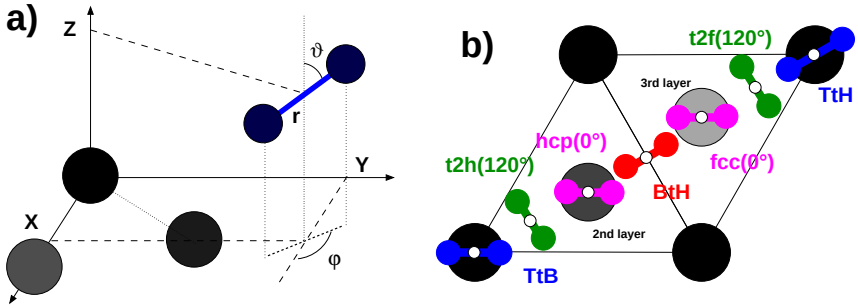

Figure 4.1: a) The coordinate system used to define the position and the orientation of H_2 on the Cu(111) surface. b) Schematic representation of the (X,Y,φ) geometries considered.

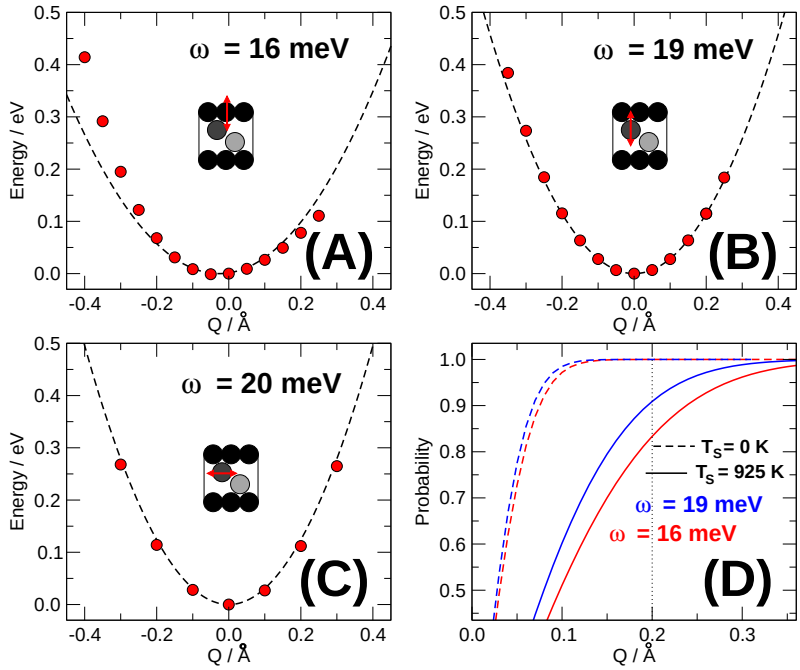

Figure 4.2: The dependence of potential energy curves on different lattice coordinates in the bare Cu(111) surface: $Q_1^{\perp}$ (A), $Q_2^{\perp}$ (B) and $Q_2^{\parallel}$ (C). The potential has been fitted to an harmonic model (the frequency ω is reported in the graph). Panel (D) reports the probability to find the atom within a distance Q from the equilibrium position computed integrating the probability distribution of Eq. 4.1, for ω=19 meV (blue) and ω = 16 meV (red), at surface temperatures T_S= 0 K (dashed lines) and T_S= 925 K (solid lines).

implemented in Ref. [25, 26] was applied. In this approach the exchange-correlation energy is computed as a weighted average of two GGA functionals, the Revised Perdew-Burke-Ernzerhof (RPBE) functional [45] and the Perdew-Wang 1991 (PW91) functional [46]:

$$E_{xc}^{SRP} = x\, E_{xc}^{RPBE} + (1-x)\, E_{xc}^{PW91}$$

Here, the mixing parameter value $x = 0.43$ has been chosen semi-empirically to reproduce the reaction probabilities measured in D_2 / Cu(111) molecular beam experiments [3].

As in Ref. [25, 26], the Cu surface is described with a supercell using four layers of metal atoms, employing a 2x2 hexagonal surface unit cell. A vacuum space of 13.0 Å is placed between the four-layer slabs to avoid artifacts due to the use of periodic boundary conditions in the direction perpendicular to the slab. The first Brillouin zone is sampled with a 8x8x1 Monkhorst-Pack grid of **k**-points. A plane wave basis set with an energy cutoff of 350 eV is used in the calculations. Further details can be found in Ref. [27].

In the following we will describe the effect of the Cu motion on the barriers with two quantities: the displacement of the barrier geometry in the (r, Z, ϑ) space and the change in the barrier height. For small displacements of the Cu atoms, both effects are roughly linear in the surface coordinate. Following Ref. [39], we define two linear parameters α and β by

$$\Delta Z_b = \alpha Q$$

$$\Delta E_b = -\beta Q$$

The parameter α accounts for the barrier displacement in the Z direction. Its maximum value may be presumed to be 1, corresponding to the SO model. The parameter β, on the other hand, describes the change in barrier height due to the motion of the lattice atom.

4.3 Results and discussion

Fig. 4.2 shows the dependence of the SRP-DFT energy of the bare surface on the $Q_1^{\perp}$, $Q_2^{\perp}$ and $Q_2^{\parallel}$ degrees of freedom. The dependence on $Q_3^{\perp}$ is not reported, since in a four layer slab the 2^{nd} and the 3^{rd} layers are equivalent in the absence of H_2.

From these potential curves we can get a picture of the motion of the Cu atoms. Treating the oscillations in the harmonic approximation, the vibrational period is in the range 200-260 fs. For the $Q_1^{\perp}$ coordinate, a better fit can presumably be obtained with a Morse function, describing the anharmonicity of the potential. However this is not important for the goals of the present work, and this direction will not be pursued.

Assuming a thermal population of the vibrational harmonic states, the probability distribution of the copper atom position is given by

$$p(Q;T) = \sum_{\nu} p_{\nu}(T)\,|\phi_{\nu}(Q)|^2 \tag{4.1}$$

where $\phi_{\nu}(Q)$ is the ν-th harmonic oscillator eigenstate and $p_{\nu}(T)$ is the corresponding Boltzmann weight. With this simple model, for the 2^{nd} layer Cu atom at T_S = 925 K the probability to find the atom with a ΔZ displacement greater than 0.2 is 4.5%. In light of this, in our analysis we will focus on a Q interval of a few tenths of Å.

It should be kept in mind that our way of modeling phonon motion is approximate. Apart from the already mentioned assumptions - harmonic approximation and equilibrium thermal distribution - the Cu atom degrees of freedom we are considering are not phonons by themselves, hence their coupling is not negligible and they cannot be treated independently of one another.

The dependence of the barrier properties on $Q_1^{\perp}$ is reported in Table 4.1 and Fig. 4.3. The changes in barrier heights for $Q_1^{\perp} = \pm 0.2$ Å are at most 21 meV, a value which is small compared to the barrier energy itself, which ranges from 0.63 eV to 1.02 eV for $Q_1^{\perp}$= 0. For t2h(120°), TtB and hcp(0°), in

Barrier config.	Surface $Q_1^{\perp}$(Å)	ϑ (°)	Geometry Δr (Å)	ΔZ (Å)	Barrier Height ΔE (meV)
BtH	- 0.2	90.	0.01	-0.06	21.
	+ 0.2	90.	0.01	0.07	-20.
t2h	- 0.2	90.	-0.04	-0.14	-1
($\varphi = 120°$)	+ 0.2	90.	0.06	0.15	21.
TtB	- 0.2	90.	-0.04	-0.16	-2
	+ 0.2	90.	0.06	0.17	18.
hcp	- 0.2	83.	-0.04	-0.09	-21.
($\varphi = 0°$)	+ 0.2	96.	0.06	0.09	10.

Table 4.1: Effects of the perpendicular motion of the 1^{st} layer Cu atom $Q_1^{\perp}$ on some relevant dissociation geometries and the associated barrier heights.

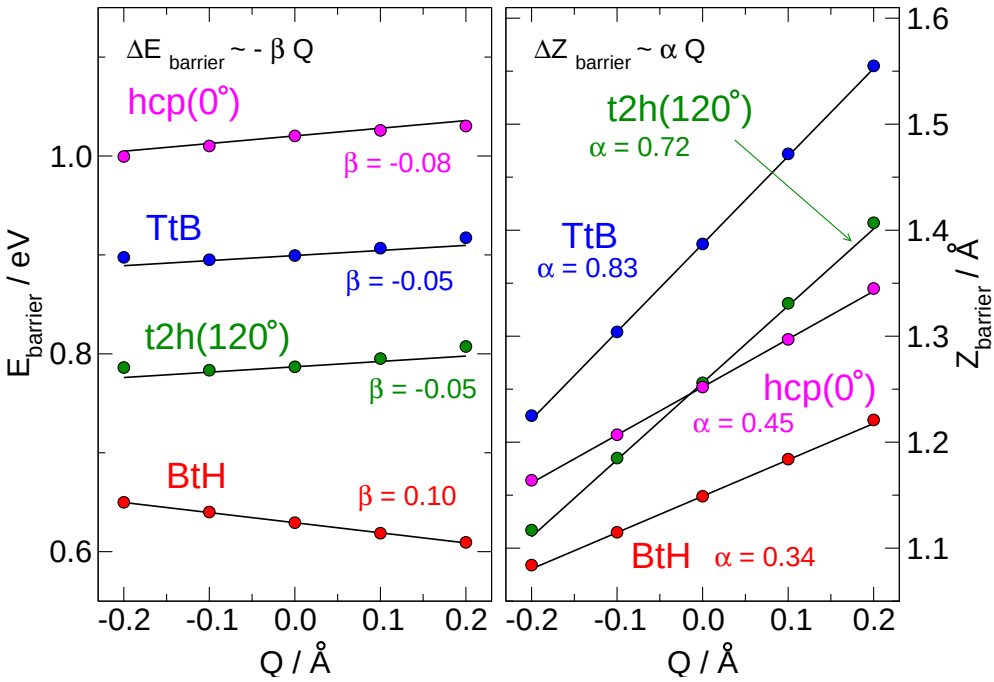

Figure 4.3: Barrier height and Z coordinate of some representative dissociation geometries as a function of the lattice coordinate $Q_1^{\perp}$. The fitting parameters α (dimensionless) and β (in eV Å^{-1}) are reported in the graph.

the dependence of E_b on $Q_1^\perp$ there are deviations from linearity. We adopt a linear model anyway to have an indication of the order of magnitude of the effect.

For $Q_1^\perp \neq 0$ there are large changes in the geometry of the barrier, and consequently large α values. The displacement is for the most part larger as the H_2 center of mass is nearer to the moving copper atom, and is maximum for the TtB configuration.

Since α is considerably lower for the hcp and bridge barriers than for the top one, the movement of the Cu atom changes the position of the barrier in a way that depends on (X, Y). Thus motion in $Q_1^\perp$ results in a change in the geometric corrugation [47] of the surface.

The tilted polar angles for the hcp barrier at $Q_1^\perp \neq 0$ reflects the local curvature of the surface and is mostly a geometrical effect. We cannot see the tilting in other barrier geometries, since in the other configurations the Cu atom motion cannot change in an asymmetric way the interaction between the surface and the individual H atoms.

We can assess the capability of the SO model to reproduce the influence of the $Q_1^\perp$ lattice motion by looking at the α parameter. In the SO model, the barrier height is not affected, but the dissociation geometry is shifted by $Q_1^\perp$ in the Z direction. This means that α = 1.0 and β = 0.0 for any dissociation barrier. From these consideration, the SO model works well for TtB (α = 0.83) and t2h(120°) (α = 0.72). In the hcp(0°) case, β is almost 0 but α = 0.45 is considerably lower than 1. The approximation is even more severe for the BtH site, for which both parameters are different from the SO model parameters (α = 0.34 and β = 0.10 eVÅ^{-1}).

We can make a direct comparison between the DFT-SRP potential and the SO model. We define the coupling potential of the six H_2 coordinates $\mathbf{r} = (r, \vartheta, \varphi)$, $\mathbf{R} = (X, Y, Z)$ and the surface degree of freedom Q as

$$V_{coup}(\mathbf{r}, \mathbf{R}, Q_1^\perp) = V_{7D}(\mathbf{r}, \mathbf{R}, Q_1^\perp) - V_{6D}(\mathbf{r}, \mathbf{R}) - V_{vib}(Q_1^\perp)$$

where V_{6D} is the 6D potential of H_2 interacting with the ideal frozen Cu(111) surface ($Q_1^\perp = 0$) and $V_{vib}(Q_1^\perp)$ is the potential for the $Q_1^\perp$ motion in absence

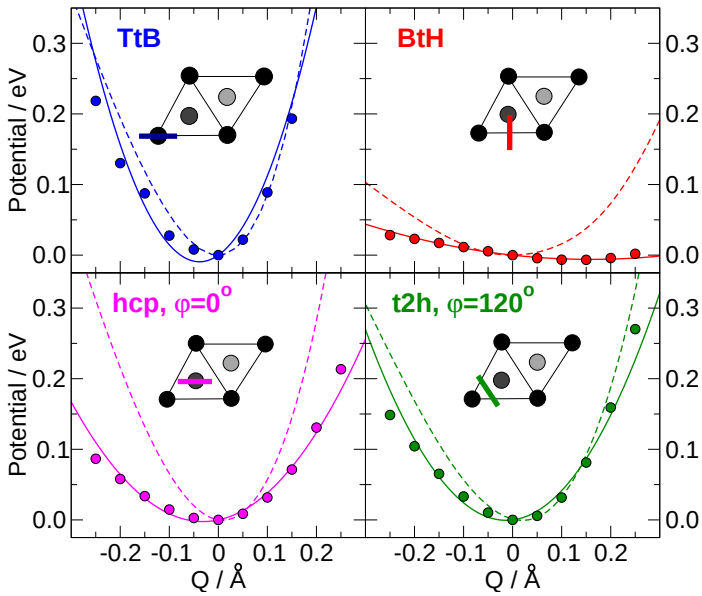

Figure 4.4: The coupling potential between H_2 and the surface degrees of freedom has been plotted as a function of $Q_1^{\perp}$ at some frozen surface barrier geometries. The DFT points (circles) have been fitted with a quadratic model (solid lines). The coupling potential curves for the Surface Oscillator model computed with the Díaz et al. PES [26] are shown with dashed lines.

of the H_2 molecule, i. e.

$$V_{6D}(\mathbf{r},\mathbf{R}) = V_{7D}(\mathbf{r},\mathbf{R},0)$$

$$V_{vib}(Q_1^{\perp}) = V_{7D}(\mathbf{r}_{H_2}^{eq},\mathbf{R}_{\infty},Q_1^{\perp}) - V_{7D}(\mathbf{r}_{H_2}^{eq},\mathbf{R}_{\infty},0)$$

where $\mathbf{r}_{H_2}^{eq}$ is the equilibrium distance of H_2 and $\mathbf{R}_{\infty}$ corresponds to a negligible interaction between the molecule and the surface.

Fixing $(\mathbf{r},\mathbf{R})$ at the four lowest barriers geometries of the ideal frozen surface, we compare the DFT-SRP coupling with the coupling assumed by the SO model (Fig. 4.4). As expected, the SO model works fairly well for the barrier geometries in which the H_2 is near to the moving Cu atom: TtB and t2h(120°). For the hcp(0°) site, the SO model only reproduce qualitatively the quadratic behavior of the coupling, whereas it completely fails for the BtH barrier.

If we displace a 2^{nd} layer Cu atom, the picture is completely different (Table 4.2 and Fig. 4.5). In this case the dissociation geometry does not undergo

Barrier config.	Surface $Q_{2^{nd},\perp}$ (Å)	ϑ (°)	Geometry Δr (Å)	ΔZ (Å)	Barrier Height ΔE (meV)
BtH	- 0.2	90.	-0.03	0.01	-48.
	+ 0.2	90.	0.03	-0.01	69.
t2h	- 0.2	90.	-0.02	0.00	-42.
$\varphi = 120°$	+ 0.2	90.	0.02	0.00	62.
TtH	- 0.2	90.	-0.01	0.00	-1.
	+ 0.2	90.	0.00	0.00	10.
hcp	- 0.2	90.	-0.01	-0.01	-65.
$\varphi = 0°$	+ 0.2	90.	0.00	0.01	85.

Table 4.2: Effects of the perpendicular motion of the 2^{nd} layer Cu atom $Q_2^{\perp}$ on some relevant dissociation geometries and the associated barrier heights.

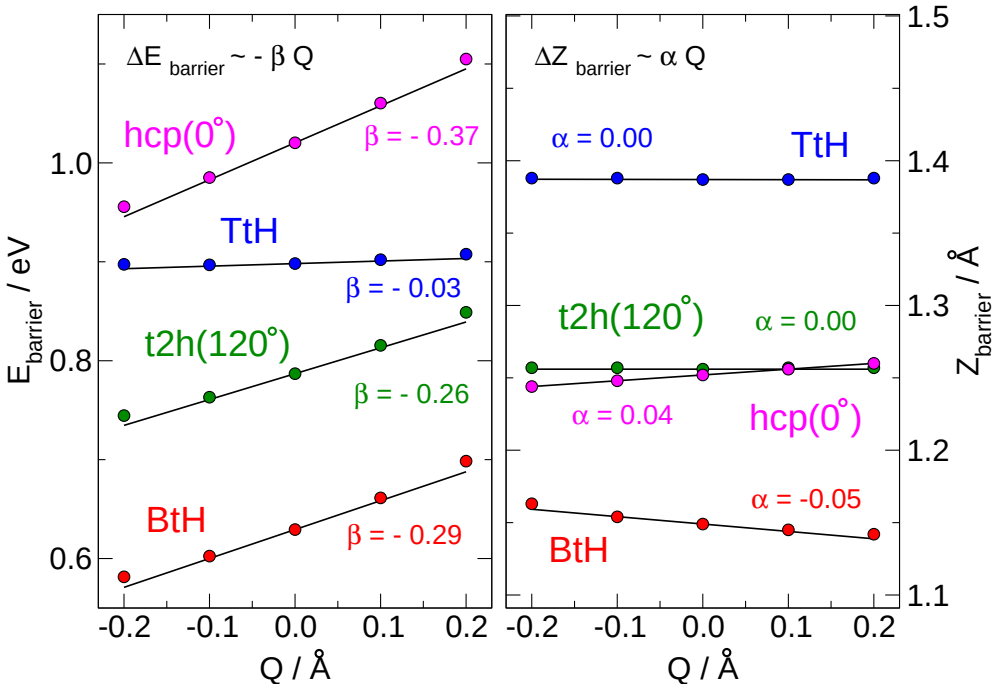

Figure 4.5: Barrier height and Z coordinate of some representative dissociation geometries as a function of the lattice coordinate $Q_2^{\perp}$. The fitting parameters α (dimensionless) and β (in eVÅ^{-1}) are reported in the graph.

large changes and the values of α are very small. Within a few hundredths of Å, we can assume that the dissociation barrier geometries are not dependent on $Q_2^{\perp}$.

In contrast, relevant changes are found in the barrier height. For $Q_2^{\perp} = -0.2$ Å, the BtH, t2h(120°) and hcp(0°) barrier heights are lowered by 48 meV, 42 meV and 65 meV respectively. In all these configurations, the height decreases as the the copper atom moves towards the bulk ($\beta < 0$). Only the TtH barrier height is hardly affected by $Q_2^{\perp}$. In this case the energy is mostly determined by the interaction with the nearest 1^{st} layer Cu atom, and the H_2 on top, which is rather far away from the surface, does not feel the 2^{nd} layer Cu atom displacement.

Unlike the 1^{st} layer atom displacement, the motion of the 2^{nd} layer Cu atom does not change the dissociation geometry much, and it has no consequence for the geometrical corrugation of the PES. However, the motion of a 2^{nd} layer Cu atom does alter the energetic corrugation [47]. For $Q_2^{\perp} \neq 0$ barriers heights are decreased or increased in different ways for the dissociation geometries considered. This causes a marked (X, Y) dependence of the barrier height change with $Q_2^{\perp}$ which could affect the coupling between diffraction states of the incident molecule.

It is clear that the SO Model is completely inappropriate for describing the effect of the 2^{nd} layer Cu atom motion. We therefore compare our results with the MSO model of Dohle and Saalfrank [33]. With this model the height of the barrier along the reaction path can become smaller or larger, whereas the position of the barrier is only slightly affected. The MSO model assumes that the coupling between the molecule and the surface (1) is linear in the surface degree of freedom Q and (2) is an exponentially decaying function of Z and r

$$V_{coup}(r, Z, Q) = A\, Q \exp\left(-\gamma \sqrt{Z^2 + 1/4 r^2}\right)$$

By plotting the $SRP - DFT$ coupling potential at some dissociation geometries as a function of Q (Fig. 4.6, panel (a)), we can see that for small

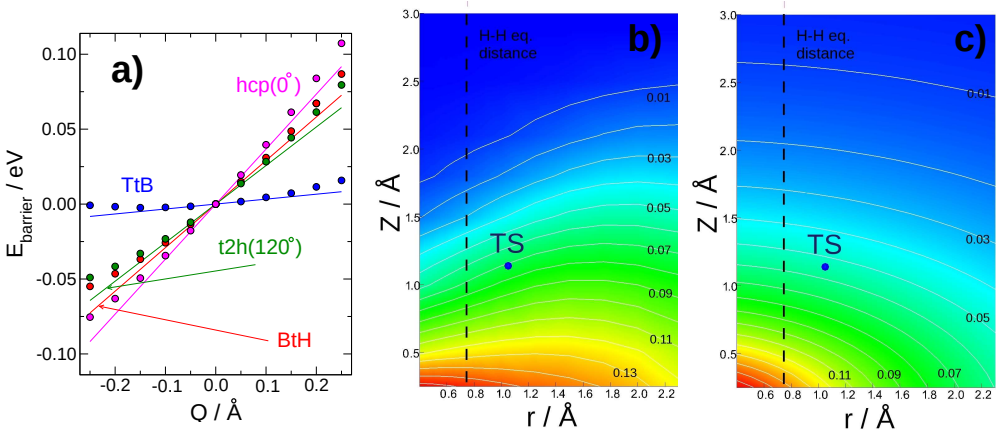

Figure 4.6: Fitting of the DFT-SRP $V_{coupling}$ the MSO Model by Dohle and Saalfrank [33]. Graph (a) shows the coupling potential as a function of $Q_2^{\perp}$ computed at some relevant dissociation geometries. The lines are the best linear curves fitting the data. Graph (b) is the coupling potential at the BtH configuration for $Q_2^{\perp} = 0.2$Å as a function of (r, Z) while (c) is the fitted exponential function $A' e^{(Z^2+1/4r^2)^{1/2}}$. In graphs (b) and (c) the gas phase H_2 equilibrium distance is shown using a dotted line. The transition state geometry for the dissociation is also represented.

values of Q, the coupling is approximately linear. So the first assumption of the model holds quite well.

We also considered the coupling potential for the BtH configuration and $Q_2^{\perp} = 0.2$ Å as a function of r and Z (Fig. 4.6, panel (b)) and we fitted it to the exponential function of r and Z in the MSO model (panel (c)). At a first glance, the comparison is not good. In particular the model seems not to have the right r dependence to reproduce the data. However, the Z dependence seems at least qualitatively correct and is likely to be the most important feature affecting the reacting molecule moving to the dissociation geometry.

Given the completely different dependence of the PES on $Q_1^{\perp}$ and $Q_2^{\perp}$, it is convenient to establish if the two motions can at least approximately be considered independently one from the other. We computed the non additive effects of the two degrees of freedom as:

$$\Delta E_{non\,add}(Q_1^{\perp}, Q_2^{\perp}) = \Delta E_{barrier}(Q_1^{\perp}, Q_2^{\perp}) - \Delta E_{barrier}(Q_1^{\perp}, 0) - \Delta E_{barrier}(0, Q_2^{\perp})$$

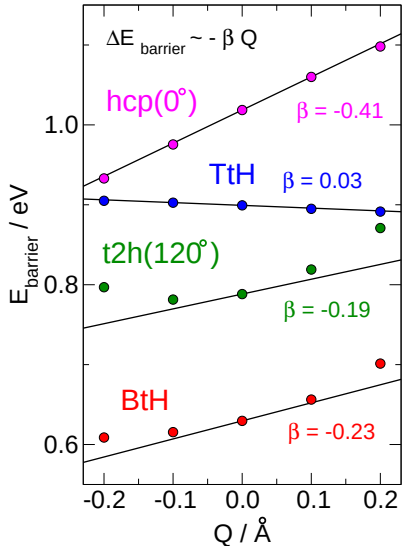

Figure 4.7: Barrier heights of some representative dissociation geometries as a function of the lattice coordinate $Q_1^{\parallel}$. The linear fitting parameters β are reported in the graph in unit of eVÅ^{-1}.

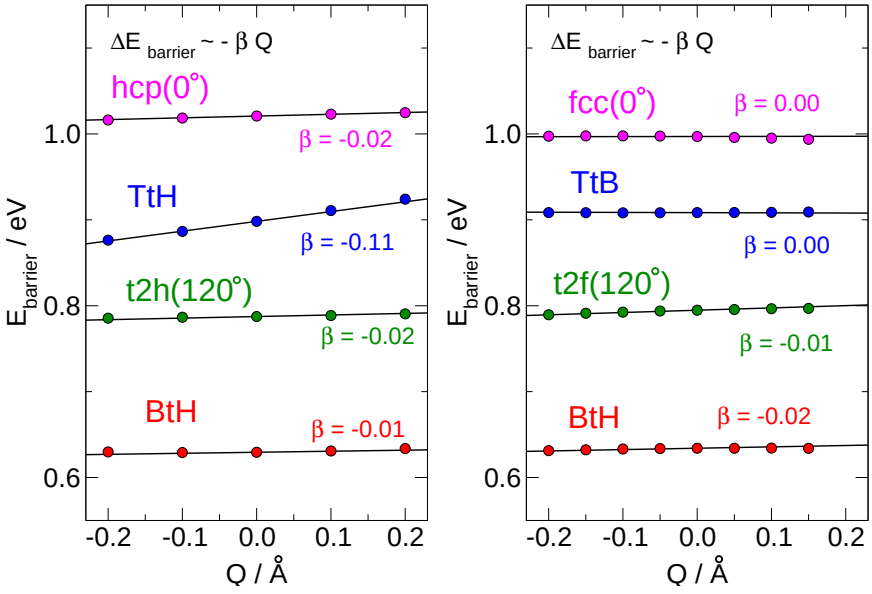

Figure 4.8: Barrier heights of some representative dissociation geometries as a function of the lattice coordinate $Q_2^{\parallel}$ (left) and on $Q_3^{\perp}$ (right). The linear fitting parameters β are reported in the graph in unit of eVÅ^{-1}.

Barrier config.	$Q_{1^{st}}^{\perp}$ (Å)	$Q_2^{\perp}$ (Å)	θ (°)	**Geometry** Δr (Å)	ΔZ (Å)	**Barrier Height** ΔE (meV)
BtH	- 0.2	-0.2	90.	-0.001	-0.003	-8.
	-0.2	+0.2	90.	0.001	0.001	7.
	+0.2	-0.2	90.	0.004	-0.006	8.
	+ 0.2	+0.2	90.	-0.001	0.001	-8.
t2h	- 0.2	-0.2	90.	-0.002	-0.001	-13.
$\varphi = 120°$	-0.2	+0.2	90.	0.000	0.000	14.
	+0.2	-0.2	90.	0.003	-0.001	12.
	+ 0.2	+0.2	90.	-0.002	-0.001	-14.
TtB	- 0.2	-0.2	90.	0.001	-0.001	-10.
	-0.2	+0.2	90.	0.000	0.000	11.
	+0.2	-0.2	90.	0.002	0.000	7.
	+ 0.2	+0.2	90.	-0.001	-0.001	-9.
hcp	- 0.2	-0.2	83.	-0.002	0.000	-9.
$\varphi = 0°$	-0.2	+0.2	83.	0.002	0.001	8.
	+0.2	-0.2	97.	0.003	0.001	10.
	+ 0.2	+0.2	97.	-0.006	-0.002	-10.

Table 4.3: Non additive effects of combined perpendicular motion of $Q_1^{\perp}$ and $Q_2^{\perp}$ coordinates at some relevant dissociation geometries.

and using analogous formulas for $\Delta r_{non\,add}$ and $\Delta Z_{non\,add}$. From the results reported in Table 4.3 we can conclude that the effects of the motion of the two different surface atoms on the reaction barrier are additive to a very good approximation. In the interval $[-0.2\,\text{Å}, +0.2\,\text{Å},]$ of the lattice coordinates, the order of magnitude of the error in the dissociation geometry is just a few mÅ. Similarly, the error in the barrier height is at most 14 meV and is not relevant at our scale. In view of this, we can consider the effects of the two degrees of freedom independently from each other.

Fig. 4.7 shows some preliminary results about the dependence of the barrier heights on $Q_1^{\parallel}$, the parallel displacement of a top layer Cu atom. For each barrier the direction of the Cu atom displacement was chosen to give the biggest change in energy. In these calculations we assumed that the barrier geometry is independent of $Q_1^{\parallel}$. So we did not optimize the transition state but fixed the H_2 molecule in the dissociation geometry for the ideal frozen surface. With this rather crude approximation, we can see that this kind of motion seems to have an effect that closely resembles the effect of $Q_2^{\perp}$: a significant barrier change for the BtH, t2h(120°) and hcp(0°) barriers and a very small difference for the TtH barrier. The BtH and t2h(120°) barrier heights seem to depend quadratically on $Q_1^{\parallel}$ but this may be due to the fixed geometry approximation. This problem, i.e. the systematic description of the barrier geometry change, will be addressed in future work.

For the sake of completeness, we studied the dependence of the barrier height on the displacement of the 2^{nd} layer Cu atom parallel to the surface and the 3^{rd} layer Cu atom perpendicular to the surface. (Fig. 4.8). We assumed that no geometry change occurs for these coordinates as well. Since we found that $Q_2^{\perp}$ does not change the dissociation geometry, we expect this approximation to work well in the case of $Q_2^{\parallel}$ and $Q_3^{\perp}$.

For the parallel displacement of the 2^{nd} layer Cu, we report the change of barrier height in the [1,1,-2] direction (corresponding to $\varphi = 30°$). For this particular direction we expect $Q_2^{\parallel}$ to have the maximum effect on the BtH dissociation barrier. From the SRP-DFT calculations, we found that the [1,1,-2]

parallel motion gives rise to the largest changes for all the dissociation barriers. However, these changes are still small compared to the changes accompanying perpendicular motion of the same Cu atom. Except for the TtH barrier, the β coefficient is one order of magnitude larger for $Q_2^{\perp}$ than for $Q_2^{\parallel}$.

For all the dissociation barriers considered, the 3^{rd} layer vibration of the fcc Cu atom has negligible effect on the barrier height. This suggests that the 3^{rd} layer motion - and reasonably the motion in any lower layer - does not have an important effect on the reaction. These layers can still have a dynamical influence by exchanging energy through their coupling with the upper layers and acting like a thermal bath. However, also considering the mass mismatch and the small forces, we expect a very small exchange of energy between the molecule and the surface atoms in this layer, and this effect is unlikely to play a major role in the dynamics.

Summing up, we have found that the lattice coordinates that cause the largest effect on the H_2 / Cu(111) DFT-SRP barrier heights and locations are the motion of the 1^{st} layer and 2^{nd} layer Cu atoms in the Z direction, $Q_1^{\perp}$ and $Q_2^{\perp}$, and the motion of the 1^{st} layer atom in the parallel direction $Q_1^{\parallel}$. The effects of $Q_1^{\perp}$ and $Q_2^{\perp}$ are additive to a good approximation and are very different from each other. Motion in the first coordinate induces changes in the position of the barrier, which are partially described by the SO model. Motion in the latter coordinate, on the other hand, mostly affects the height of the barrier. As in the MSO model, for small $Q_2^{\perp}$ the coupling is linear in the lattice coordinate. In this case the dissociation geometry change is negligible and the almost linear coupling leads to a linear change of the barrier height with $Q_2^{\perp}$. Further investigation is needed for the parallel motion of the first layer atom, $Q_1^{\parallel}$.

It is interesting to note that the largest changes in barrier location occur for first layer Cu atom motion perpendicular to the surface, with the barrier almost moving with the surface atom, as in the SO-model. The largest changes with barrier location are found for the TtH and t2h dissociation geometries (α = 0.83 and 0.72, respectively), where the molecules centre-of-mass is close

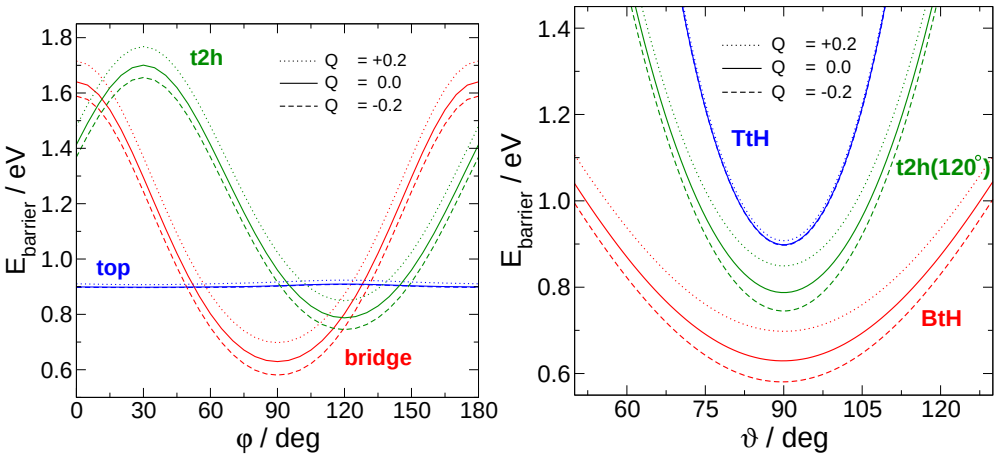

Figure 4.9: Dependence on φ (left) and on ϑ (right) of the the barrier height corresponding to some representative dissociation geometry, when the 2^{nd} layer Cu atom is displaced along the perpendicular direction. Solid lines are barrier energies for the surface in the equilibrium geometry, while dashed lines are for $Q_2^{\perp} = -0.2$ Å and dotted lines for $Q_2^{\perp} = 0.2$ Å. For the φ curves, in the geometries considered H_2 is parallel to the surface ($\vartheta = 90°$).

to the moving atom. This suggests that the barrier location effect mostly results from the Pauli repulsion between the moving first layer atom and the impinging molecule. The changes occurring in the barrier height with perpendicular motion of a second layer Cu atom, or parallel motion of a first layer Cu atom, are more subtle, and probably reflect electronic interactions of a more delocalised nature. We intend to explore these effects in more detail in a subsequent study.

Another feature of a PES we investigated is the anisotropy of the potential in the angles of orientation, i.e. the dependence of the barrier height on the coordinates φ and ϑ of H_2. A dependence of the anisotropy on the surface atom motion could increase the reactivity of the molecule in some particular rotational states, thus resulting in a different quadrupole rotational alignment parameter in associative desorption.

Fig. 4.9 shows how the barrier height depends on the angular coordinates, when the 2^{nd} layer Cu atom is displaced from its equilibrium position. Motion

		α (dimensionless)			β (eV / Å)		
Lattice coord	Barrier	RPBE	SRP	PW91	RPBE	SRP	PW91
$Q_1^\perp$	BtH	0.34	0.34	0.34	0.104	0.102	0.103
	t2h	0.73	0.73	0.73	-0.069	-0.054	-0.034
	TtB	0.83	0.83	0.83	-0.067	-0.051	-0.032
	hcp	0.44	0.45	0.46	-0.065	-0.077	-0.120
$Q_2^\perp$	BtH	-0.03	-0.05	-0.11	-0.297	-0.293	-0.287
	t2h	0.00	0.00	0.00	-0.262	-0.261	-0.262
	TtH	0.00	0.00	0.00	-0.032	-0.032	-0.027
	hcp	0.04	0.04	0.04	-0.372	-0.374	-0.376

Table 4.4: Dependence of the linear coefficients α and β on the SRP mixing coefficient.

in $Q_2^\perp$ has small effects on the angular anisotropy of the PES: the effect both for φ and for ϑ is mostly to shift the curves upwards or downwards. No large dependence of the barrier height change with $Q_2^\perp$ on the angular coordinates is found.

Even without any influence on the angular anisotropy of the potential, a change in the rotational quadrupole alignment parameter is still possible. Assuming normal energy scaling and neglecting the coupling between scattering coordinates and parallel momentum, the reaction probability is the average of the reaction probability at each (X, Y) site of the surface [21]. For each site, our results suggest that $Q_2^\perp$ has little effect on the dependence of the reaction probability on the rotational state, since it does not affect the angular anisotropy. However, the displacement of the Cu atom changes the barrier height by a different value at each (X, Y) geometry. In this way the inclusion of $Q_2^\perp$ could favor the reaction at specific (X, Y) configurations with either lower or higher angular anisotropy, resulting in a different reaction probability for a given rotational state, and consequently a different rotational quadrupole alignment parameter, which might affect the comparison [26] with experiments [9].

To complete the analysis, we now briefly discuss the DFT-SRP method in the context of surface motion. The mixing coefficient in the SRP functional of Díaz et al. [25] was chosen to reproduce the results of an D_2 + Cu(111)

scattering experiment with a low surface temperature ($T_S = 120\,K$). In these conditions, we expect the surface motion influence on the reaction to be small. Nevertheless, it is possible that the inclusion of a surface degree of freedom in the dynamical model could affect the reaction probability somewhat even for a low surface temperature. In this case, a small adjustment of the mixing coefficient could lead to increased agreement with experiment.

Table 4.4 reports the values of the linear parameters α and β computed with RPBE, SRP and PW91 for the lattice coordinate $Q_1^{\perp}$, $Q_2^{\perp}$ and for the usual dissociation geometries. The RPBE and PW91 functionals correspond to the extreme possible values of the SRP mixing coefficient: $x = 1.0$ for RPBE and $x = 0.0$ for PW91. We found that the values of α are mostly unaffected by the change of functional. The differences in the β coefficients, on the other hand, are few hundredths of eV/Å. Considering the order of magnitude of the Cu displacement, these differences determine an energy change which is smaller than 10 meV.

We conclude that a change of PW91-RPBE mixing would not alter the dependence of the barrier on the lattice coordinates much. We can reasonably assume that our present results would not be significantly affected by an adjustment of the coefficient.

4.4 Conclusions

In the work presented here, we have investigated the problem of how the inclusion of lattice motion affects the reaction of $H_2(D_2)$ on Cu(111). With DFT calculations in the SRP approach, we have studied the dependence of the dissociation geometry and the barrier height on some localized surface degrees of freedom. We found that within the temperature range relevant to the experiments on dissociative sticking and associative desorption, these effects are linear to a good approximation. They can be represented by two parameters, α and β, describing respectively the dissociation geometry displacement in Z and the change in the barrier height.

The α and β parameters are highly dependent on the (X, Y) coordinates. When the molecule is over a top site, the largest changes are caused by motion of the nearest 1^{st} layer Cu atom and the effect is essentially a shift of the barrier geometry. The α parameter associated with $Q_1^{\perp}$ is close to 1, whereas β is almost 0. When the molecule is on a bridge or hollow site, both the 1^{st} layer and the 2^{nd} layer should be taken into account. In this case the lattice motion - especially $Q_2^{\perp}$ and $Q_1^{\parallel}$ - can raise or decrease the barrier height and the β parameter for these lattice coordinates differs considerably from 0.

At least for the 2^{nd} layer Cu atoms, the effects of lattice motion seem mostly independent on the angular coordinates (ϑ, φ).

From the dynamical point of view, the α parameter takes into account a simple mechanical recoil effect, which in previous studies has been introduced with the SO model. This effect results in a broadening and a shift of the reaction probability to higher energies. According to previous dynamical simulations [26, 34], recoil plays a minor role in the dissociative chemisorption of hydrogen and deuterium. This fact is well understood in terms of the magnitude of the force acting on the lattice atoms and the mass mismatch between the incident molecule and the metal atoms.

The effect described by β, on the other hand, cannot be included in the PES using the SO model. For this reason its consequences on the dynamics have been investigated in very few theoretical works, either with a model coupling linearly dependent on Q [33] or through the inclusion of a lattice degree of freedom in the PES [40]. The available results show that the introduction of this kind of effect lead to a T_S dependent broadening and a small shift of the sticking probability to lower energies.

In conclusion, both lattice effects - the geometry shift and the barrier height change - probably lead to a broadening of the reaction probability. In the past it has been shown that the SO model alone is not sufficient to reproduce the broadening of the sticking curve with T_S measured in experiments [7, 25, 26]. Our calculations clearly indicate that the combination of the effects induced by both the first and second layer could be responsible for this behavior, and

that it should be necessary to move beyond the SO-model when describing the effect of surface phonons on reaction of H_2 on Cu(111).

Further, we expect that the inclusion of the motion of the 2^{nd} layer Cu atom in the dynamical model would increase the reaction probability for the bridge and t2h reaction sites at low incident energy. On the other hand, we expect a smaller influence on the reaction probability for the top site. Because of the high φ anisotropy at these sites, at the bridge and t2h sites the reaction is not likely to occur in rotationally excited states with high M_J. This could lower the rotational quadrupole alignment parameter at low incident energies, leading to a better agreement with the experimental results for D_2 + Cu(111) [9] than obtained before [26].

As in the dynamical simulations of Tiwari and co-workers [40], the effect parametrized by β could be relevant for the interaction of H_2 on Cu(111) in the absence of energy transfer to the phonons. In our case the reduced mass of the incoming molecule and the magnitude of the force acting on the lattice are even smaller than in the system of Ref. [40]. This makes H_2 on Cu an ideal system for applying vibrational sudden approximations [40, 48, 49], and the validity of these approximations for the phonons should be explored in future studies of H_2 + Cu(111).

The results presented in this chapter are reported in the following publication:

M. Bonfanti, C. Díaz, M. F. Somers and G. J. Kroes,
"Hydrogen dissociation on Cu(111): the influence of lattice motion. Part I"
Phys. Chem. Chem. Phys., **13**, 4552-4561 (2011)

Bibliography

[1] H. F. Berger, M. Leisch, A. Winkler and K. D. Rendulic, *Chem. Phys. Lett.* **175**, 425 (1990).

[2] H. A. Michelsen and D. J. Auerbach, *J. Chem. Phys.* **94**, 7502 (1991).

[3] C. T. Rettner, D. J. Auerbach and H. A. Michelsen, *Phys. Rev. Lett.* **68**, 1164 (1992).

[4] A. Hodgson, J. Moryl, P. Traversaro and H. Zhao, *Nature* **356**, 501 (1992), 10.1038/356501a0.

[5] H. A. Michelsen, C. T. Rettner, D. J. Auerbach and R. N. Zare, *J. Chem. Phys.* **98**, 8294 (1993).

[6] C. T. Rettner, H. A. Michelsen and D. J. Auerbach, *Chem. Phys.* **175**, 157 (1993).

[7] C. T. Rettner, H. A. Michelsen and D. J. Auerbach, *J. Chem. Phys.* **102**, 4625 (1995).

[8] S. J. Gulding, A. M. Wodtke, H. Hou, C. T. Rettner, H. A. Michelsen and D. J. Auerbach, *J. Chem. Phys.* **105**, 9702 (1996).

[9] H. Hou, S. J. Gulding, C. T. Rettner, A. M. Wodtke and D. J. Auerbach, *Science* **277**, 80 (1997).

[10] A. Hodgson, P. Samson, A. Wight and C. Cottrell, *Phys. Rev. Lett.* **78**, 963 (1997).

[11] M. J. Murphy and A. Hodgson, *J. Chem. Phys.* **108**, 4199 (1998).

[12] G. R. Darling and S. Holloway, *J. Chem. Phys.* **97**, 734 (1992).

[13] J. Sheng and J. Z. H. Zhang, *J. Chem. Phys.* **99**, 1373 (1993).

[14] G. R. Darling and S. Holloway, *Surf. Sci.* **307-309**, 153 (1994).

[15] J. Dai and J. Z. H. Zhang, *Surf. Sci.* **319**, 193 (1994).

[16] J. Dai, J. Sheng and J. Z. H. Zhang, *J. Chem. Phys.* **101**, 1555 (1994).

[17] G. R. Darling and S. Holloway, *J. Chem. Phys.* **101**, 3268 (1994).

[18] A. Groß, B. Hammer, M. Scheffler and W. Brenig, *Phys. Rev. Lett.* **73**, 3121 (1994).

[19] J. Dai and J. Z. H. Zhang, *J. Chem. Phys.* **102**, 6280 (1995).

[20] G. J. Kroes, E. J. Baerends and R. C. Mowrey, *Phys. Rev. Lett.* **78**, 3583 (1997).

[21] J. Dai and J. C. Light, *J. Chem. Phys.* **107**, 1676 (1997).

[22] J. Dai and J. C. Light, *J. Chem. Phys.* **108**, 7816 (1998).

[23] M. F. Somers, S. M. Kingma, E. Pijper, G.-J. Kroes and D. Lemoine, *Chem. Phys. Lett.* **360**, 390 (2002).

[24] S. Nave, D. Lemoine, M. F. Somers, S. M. Kingma and G.-J. Kroes, *J. Chem. Phys.* **122**, 214709 (2005).

[25] C. Díaz, E. Pijper, R. A. Olsen, H. F. Busnengo, D. J. Auerbach and G.-J. Kroes, *Science* **326**, 832 (2009).

[26] C. Díaz, R. A. Olsen, D. J. Auerbach and G.-J. Kroes, *Phys. Chem. Chem. Phys.* **12**, 6499 (2010).

[27] C. Díaz, R. A. Olsen, H. F. Busnengo and G. J. Kroes, *J. Phys. Chem. C* **114**, 11192 (2010).

[28] B. Hammer, M. Scheffler, K. W. Jacobsen and J. K. Nørskov, *Phys. Rev. Lett.* **73**, 1400 (1994).

[29] M. Persson, J. Strömquist, L. Bengtsson, B. Jackson, D. V. Shalashilin and B. Hammer, *J. Chem. Phys.* **110**, 2240 (1999).

[30] Y.-Y. Chuang, M. L. Radhakrishnan, P. L. Fast, C. J. Cramer and D. G. Truhlar, *J. Phys. Chem. A* **103**, 4893 (1999).

[31] Z. S. Wang, G. R. Darling and S. Holloway, *Phys. Rev. Lett.* **87**, 226102 (2001).

[32] A. Groß, *Surf. Sci. Lett.* **314**, L843 (1994).

[33] M. Dohle and P. Saalfrank, *Surf. Sci.* **373**, 95 (1997).

[34] M. Hand and J. Harris, *J. Chem. Phys.* **92**, 7610 (1990).

[35] H. F. Busnengo, W. Dong, P. Sautet and A. Salin, *Phys. Rev. Lett.* **87**, 127601 (2001).

[36] H. F. Busnengo, W. Dong and A. Salin, *Phys. Rev. Lett.* **93**, 236103 (2004).

[37] A. C. Luntz and J. Harris, *Surf. Sci.* **258**, 397 (1991).

[38] S. Nave and B. Jackson, *J. Chem. Phys.* **127**, 224702 (2007).

[39] S. Nave and B. Jackson, *J. Chem. Phys.* **130**, 054701 (2009).

[40] A. K. Tiwari, S. Nave and B. Jackson, *J. Chem. Phys.* **132**, 134702 (2010).

[41] G. D. Billing, *Chemical Physics* **70**, 223 (1982).

[42] S. Adhikari and G. D. Billing, *The Journal of Chemical Physics* **112**, 3884 (2000).

[43] G. D. Billing, *The Journal of Physical Chemistry A* **105**, 2340 (2001).

[44] S. R. Bahn and K. W. Jacobsen, *Comput. Sci. Eng.* **4**, 56 (2002).

[45] B. Hammer, L. B. Hansen and J. K. Nørskov, *Phys. Rev. B* **59**, 7413 (1999).

[46] J. P. Perdew, J. A. Chevary, S. H. Vosko, K. A. Jackson, M. R. Pederson, D. J. Singh and C. Fiolhais, *Phys. Rev. B* **46**, 6671 (1992).

[47] G. R. Darling and S. Holloway, *Surf. Sci.* **304**, L461 (1994).

[48] J. M. Bowman, G. Drolshagen and J. P. Toennies, *J. Chem. Phys.* **71**, 2270 (1979).

[49] R. A. Olsen, G.-J. Kroes, O. M. Løvvik and E. J. Baerends, *J. Chem. Phys.* **107**, 10652 (1997).

Chapter 5

Vibrational relaxation and sticking of H on graphite

5.1 Introduction

Many interesting chemical processes can be effectively described in the framework of system-bath dynamics: in such systems the effect of the environment can be modeled as a large set of degrees of freedom in thermal equilibrium coupled to the system of interest. In the specific case of gas-surface dynamics, as an example, the degrees of freedom of the adsorbing species are coupled to the phonons and to the electron-hole pair excitations of the solid.

The presence of the environment plays two main roles on the system dynamics. On one hand, the energy of the system is transferred to the surrounding and dissipated. This effect is crucial, *e.g.*, in vibrational relaxation phenomena or atomic sticking on surfaces, which are made possible by the dissipation of kinetic energy to electrons and phonons. Phenomenologically, this energy transfer is well described by the Generalized Langevin Equation (GLE), in which the system is subjected to a random fluctuating force and to an effective friction force [1].

On the other hand, there is another less obvious effect that is strictly connected to quantum dynamics. The coupling of a quantum system to the surrounding causes the loss of coherence of the wavepacket, hence dramatically

changes the quantum behavior of the system. One of the best studied example is the tunneling probability, which is drastically reduced by the coupling with the environment [2].

The development of dissipative dynamical models is a challenging problem for current quantum techniques. The exponential scaling of these kinds of methods prevents a "brute force" approach, in which a large number of degrees of freedom for the environment is included in the model in an exact way. For this reason simplified approaches are mandatory, and have indeed been developed, trying to include the effect of the environment by means of appropriate approximations.

One approach is based on the theory of open quantum systems and focus on the derivation of a master equation for the system, *i.e.* a modified propagation equation in which the environment is implicitly included in the dynamics [3, 4]. However, the approximation scheme used in the derivation of this kind of methods is rigid and prevents the possibility of including interesting physical properties (such as memory effects in dissipation, or nonlinearity of the coupling).

An alternative more flexible approach is to explicitly couple the system to a bath consisting of a large number of harmonic oscillators [5]. The resulting Caldeira-Leggett Hamiltonian can be used to model either the classical or the quantum dynamics of a system capable of exchanging energy with the surrounding. Since the classical solution of the Caldeira-Leggett Hamiltonian is equivalent to a GLE, a connection can be established between the parameters of the Caldeira-Leggett bath (harmonic frequencies and couplings) and the fluctuation-dissipation properties of the Langevin force. Hence this important result directly relates the microscopic properties of the system and the phenomenological Langevin model [1, 6].

The actual solution of a quantum system-bath model requires approximations on the time-dependent wavepacket dynamics to reduce the computational cost and to make the problem tractable in spite of the large number of degrees of freedom. To this aim, Multi-Configuration Time-Dependent

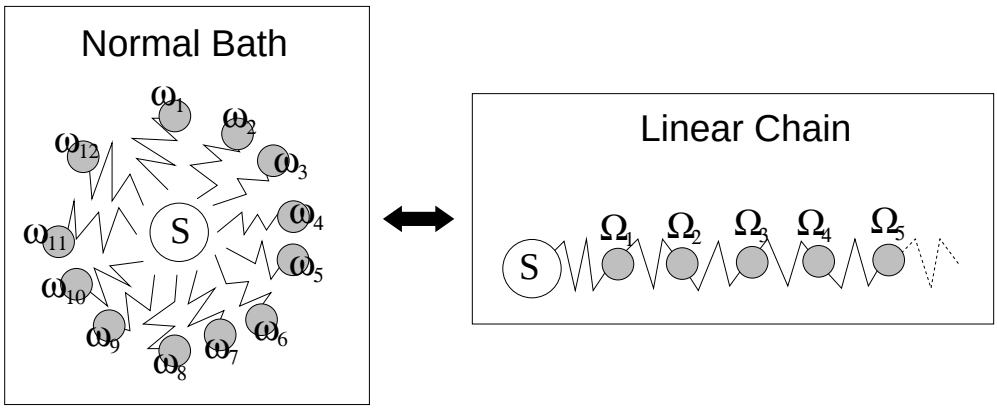

Figure 5.1: Pictorial representation of a normal oscillator bath and the equivalent linear chain, obtained through the effective mode transformation

Hartree (MCTDH) [7–9] and related methods have been shown to be very effective: baths with tens of degrees of freedom coupled to different model systems have been used with success in many recent works [10–15].

Still, the bath models applied so far are still too small to allow the description of a realistic system within the Caldeira-Leggett approach. The main practical problem of a small size bath is the strict limit set on the time of the dynamics which can be accessed without incurring in Poincaré's recurrence. In this sense, a great improvement may be achieved expressing the Caldeira-Leggett bath in an equivalent linear chain form by an effective mode transformation (Fig. 5.1). This transformation was first used in Ref.s [14, 16, 17] and has been recently expressed in an analytical form [18, 19]. The advantage of this equivalent representation lies in the fact that the system is directly coupled only to one oscillator, and not to the whole set of oscillators. In this form, there are oscillators "far" from the system that do not directly influence the system dynamics, but are used only to accommodate the energy flowing along the chain. We expect that a crude approximation on the description of these oscillators may be applied without critical consequences on the system dynamics. In the framework of MCTDH methodologies, this can be easily achieved by using a mean field approximation for the far part of the chain.

α / a.u.	D_e / eV	ω_{HO} / cm^{-1}	N_{bound}
1.238	1.550	2140	11

Table 5.1: Parameters of the Morse potential of the system. ω_{HO} is the harmonic frequency at the minimum, N_{bound} the number of bound states.

In this work, we investigate two typical atom-surface problems - energy relaxation and sticking - that necessarily require the inclusion of dissipation. We consider a hydrogen atom subjected to a Morse potential, with model parameters mimicking the interaction with a graphite surface. The system is coupled with different model baths, ranging from the ideal Ohmic bath to a more realistic bath. Quantum dynamics is performed with MCTDH methods and the performances of the normal and chain bath representations are compared for both problems.

The details of the models considered are reported in section 5.2, whereas the methodology adopted is presented in section 5.3. Then the results are reported and discussed in section 5.4 and some conclusions are drawn in section 5.5.

5.2 Models

In this work we studied energy dissipation and fluctuations by means of the following Hamiltonian, based on the Caldeira-Leggett model [5]

$$\mathcal{H} = \frac{p^2}{2m} + V(x) + \sum_k \left\{ \frac{p_k^2}{2m_k} + \frac{1}{2} m_k \omega_k^2 \left(q_k - \frac{c_k f(x)}{m_k \omega_k^2} \right)^2 \right\} \tag{5.1}$$

This Hamiltonian is composed of a system of mass m subjected to the potential $V(x)$ and a variable number of harmonic oscillators, of frequency ω_k and mass m_k. It should be noted that in this Hamiltonian, the N harmonic oscillators effectively reproduce the fluctuation and dissipation properties of the environment, rather than be realistic description of the interacting medium in which the system is placed [1].

The system - in our case an atom colliding or adsorbed to graphite - is described with a single degree of freedom, the distance between the atom and the surface. To model the system interaction, we choose a Morse potential

$$V(x) = D_e \left(e^{-2\alpha x} - 2\, e^{-\alpha x} \right) \tag{5.2}$$

with parameters that best reproduce the adsorption of a hydrogen atom to the top site of graphite (see Tab. 5.1).

The coupling $V_{coupl} = \sum_k c_k q_k f(x)$ between the system and each oscillator is linear in the bath coordinates and depends on a set of coefficients c_k. The function $f(x)$ has been introduced to switch the coupling off when the atom is far from the surface. In particular, our choice for $f(x)$ is

$$f(x) = \frac{1 - e^{-\alpha x}}{\alpha} \tag{5.3}$$

where α is the same parameter of the Morse potential [13–15, 20]. This functional form for the coupling is almost linear around the equilibrium position of the adsorbate ($f(x) \to x$ for $x \to 0$). At the same time, at large distances the coupling tends to a finite value, which is subtracted from the whole potential to set the right asymptotic limits.

In addition to the harmonic potential of the oscillators, namely $\sum_k \frac{1}{2} m_k \omega_k^2 q_k^2$, and the coupling V_{coupl}, a third term appears by expanding the square in Eq. 5.1. This contribution $V_{dist} = \frac{1}{2} f(x)^2 \sum_k \left[c_k^2 / (m_k \omega_k^2) \right]$ depends only on x and introduce a potential correction, that balances the distortion of the dynamics due to the effect of the coupling on the system.

We choose the frequencies ω_k and the couplings c_k of the bath so that the function

$$\tilde{J}(\omega) = \frac{\pi}{2} \sum_k \frac{c_k^2}{m_k \omega_k} \delta(\omega - \omega_k) \tag{5.4}$$

is a proper discretization of a given continuous spectral density $J(\omega)$. This function, in fact, fully characterizes the fluctuation and dissipation properties of an infinite bath, through the relation that can be established between

the Caldeira-Leggett Hamiltonian and a Langevin dynamics. The GLE corresponding to Eq. 5.1 can be written as

$$m\ddot{x} = -V'(x) + f'(x)\left(\xi(t) - \int_{t_0}^{\infty} \gamma(t-\tau) f'(x(\tau))\dot{x}(\tau) d\tau\right) \tag{5.5}$$

where $\gamma(t)$ is a memory-kernel entering in the dissipation term and $\xi(t)$ is a random force that induces energy fluctuations in the system.

Both the random noise and the memory-kernel are fully determined by the choice of the spectral density [19]. The function $J(\omega)$ is defined in terms of the Fourier transform of $\gamma(t)$

$$J(\omega) = m\omega\Re \int_{-\infty}^{+\infty} \gamma(t)\, e^{\imath\omega t} \tag{5.6}$$

and this relation can be inverted by exploiting the analytical properties of the memory-kernel (in particular by means of Kramers-Kronig relations). Furthermore, when the bath is in thermal equilibrium, $\xi(t)$ is a stationary Gaussian noise of vanishing mean, and its correlation function obeys the fluctuation-dissipation theorem

$$\left\langle \xi(t)\xi(t') \right\rangle = m k_B T \gamma(|t-t'|) \tag{5.7}$$

For further details the interested reader should refer to Ref. [21].

A particularly simple case of spectral density is the Ohmic case, $J(\omega) = m\gamma\omega$ with γ constant. In this special condition, it can be seen from Eq. 5.6 that $\gamma(t)$ is a Dirac delta and the dissipation term in Eq. 5.5 depends only in the velocity at present time. In other words, the system evolution is a Markovian process: dissipation and fluctuations have no memory of the past dynamics of the system.

In the present work, we adopted different spectral densities, which are reported in Fig. 5.2 along with the corresponding memory-kernel $\gamma(t)$. In detail, they are:

1. Three truncated Ohmic spectral densities, *i.e.* $J(\omega) = m\gamma\omega$ for $\omega \leq \omega_c$ and $J(\omega) = 0$ for $\omega > \omega_c$. This bath corresponds to a Markovian

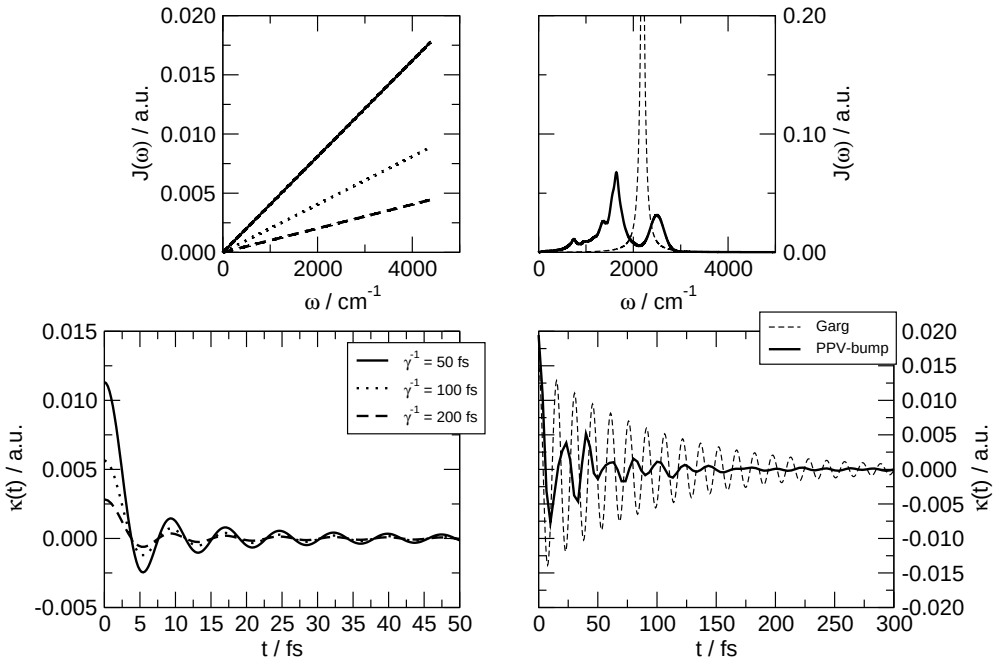

Figure 5.2: Spectral density (top panels) and memory kernels (lower panels) of the bath models adopted in this work. Left: truncated Ohmic baths with $\gamma^{-1} = 50\,fs$ (solid), $\gamma^{-1} = 100\,fs$ (dotted) and $\gamma^{-1} = 200\,fs$ (dashed). Right: non Ohmic baths with the Garg spectral density (dashed) and the PPV-Bump spectral density (solid).

dynamics on a time scale $t \gg \omega_c^{-1}$. We considered different values of the dissipation strength, which in turn determine different relaxation times: $\gamma^{-1} = 50$ fs (**OHMIC-50**), $\gamma^{-1} = 100$ fs (**OHMIC-100**) and $\gamma^{-1} = 200$ fs (**OHMIC-200**). In all the cases the cutoff frequency has been set to $\omega_c = 0.02$ au.

2. A Lorentzian spectral density

$$J(\omega) = \frac{d_0^2}{m_0} \frac{\gamma\omega}{(\omega_0^2 - \omega^2)^2 + \gamma^2\omega^2}$$

with a cutoff frequency $\omega_c = 0.02$ au (**GARG-50**). This is the spectral density felt by a particle interacting with a harmonic oscillator of frequency ω_0 and mass m_0, which in turn is coupled to a Ohmic bath with

γ^{-1} relaxation time. This model has been first introduced by A. Garg and other authors [22]. We set $\omega_0 = 0.1$ au and $\gamma^{-1} = 50$ fs. The parameter $d_0^2/m_0 = 1.497 \cdot 10^{-6}$ au is chosen so that $D_0^2 = m_{bath}\frac{2}{\pi}\int_0^\infty \omega\, J(\omega)\, d\omega$ is equal for the GARG-50 and the OHMIC-50 model.

3. A realistic spectral density (see Fig. 5.2) adapted from Ref. [23], which was obtained for the effect of environment on the exciton energy transfer in semiconducting polymers (**PPV-BUMP**). A Gaussian feature was added at high frequencies to make the spectral density more structured [19]. For this spectral density, we set ω_{cutoff} =5000 cm^{-1} =0.02278 au.

Note that in Fig. 5.2 the memory-kernels of the Ohmic baths have small oscillations, in contrast with an ideal Ohmic bath for which $\gamma(t) = 0$ for any $t \neq 0$. However, these oscillations, due to the Fourier transform of the cutoff, are on a time scale of $\omega_c^{-1} \approx 1$ fs and have an almost negligible effect on the relaxation phenomena we are interested in, that take place in a period 50 to 200 times larger.

The benchmark calculations reported in this chapter have been obtained with the normal representation of the bath, *i.e.* the bath Hamiltonian of Eq. 5.1, properly discretized to reproduce the various spectral densities considered. The same simulations were realized also with the linear chain representation of the bath:

$$\mathcal{H} = \mathcal{H}_{sys} + V_{dist} - D_0 f(x)\, X_1 + \frac{1}{2}\sum_{n=1}^{N}\left\{P_n^2 + \Omega_n^2 X_n^2\right\} - \sum_{n=1}^{N-1} D_n X_n X_{n+1}$$

This Hamiltonian is obtained by virtue of a normal-mode transformation of the Caldeira-Leggett model (Eq. 5.1). In this form the bath is represented by a set of N harmonic oscillators of unitary mass, with position X_n and momentum P_n. The frequencies Ω_n and the couplings D_n can be obtained with a suitable transformation (described in Ref. [18, 19]).

The advantage of the linear chain representation lies in the possibility to make a stronger approximation, suggested by a simple consideration: in the normal bath, all the oscillators are directly coupled to system, whereas in the

linear chain this is no longer true. This suggests that in the linear chain it is not necessary to reproduce the precise dynamics of those degrees of freedom which are less directly coupled to the system. Instead, a large part of the chain may be treated in a mean field approximation, thereby allowing a huge reduction of the wavefunction and consequently of the computational cost of the simulation.

5.3 Methodology

Time propagation was performed with Heidelberg MCTDH package [24], by expanding the wavefunction on a set of mode-combined single-particle functions. The single-particle functions, in turn, are expanded on a Discrete Variable Representation (DVR) basis set, chosen in accord to the degree of freedom considered.

5.3.1 Bath representation

In the case of the calculations with a bath in the normal representation (as in Eq. 5.1), we used a 50 oscillators bath, combined in modes of 5 degrees of freedom each. We tested the number of single particle functions in order to check the convergence of the relevant results for the problem considered (the chosen correlation schemes are reported in Tab. 5.2). In the following we will describe data obtained with this model as "normal bath" results.

In the case of the linear chain, on the other hand, we used chains of different length and tested different correlation schemes. In most calculations we used a 100 oscillators long linear chain, but calculations were also done with 200 and 300 degrees of freedom. We fully correlated just a small part of this chain (typically $N_{corr} = 5$, 10 or 15 degrees of freedom) and described the remaining part at a Time-Dependent Self-Consistent-Field (TD-SCF) level. As discussed above, with this scheme we accurately describe those degrees of freedom that mostly affect the dynamical behavior of the system, and we

Degrees of freedom	**Relaxation** *Ohmic and Garg*	**Relaxation** *PPV-Bump*	**Sticking** *Ohmic*	**Sticking** *Garg*	**Sticking** *PPV-Bump*
x	5	5	9	13	14
$q_1 \cdots q_5$	4	4	5	4	5
$q_6 \cdots q_{10}$	4	5	5	5	8
$q_{11} \cdots q_{15}$	4	5	5	10	10
$q_{16} \cdots q_{20}$	5	6	5	14	11
$q_{21} \cdots q_{25}$	5	5	5	7	8
$q_{26} \cdots q_{30}$	3	3	4	4	5
$q_{31} \cdots q_{35}$	3	3	4	3	3
$q_{36} \cdots q_{40}$	3	2	4	2	2
$q_{41} \cdots q_{45}$	3	2	4	1	1
$q_{46} \cdots q_{50}$	3	2	4	1	1

Table 5.2: Single particle scheme adopted in the MCTDH calculation with the bath in normal form.

treat the remaining with a mean field approximation. In the following sections, we will label these correlation schemes as "partially correlated chains" (abbreviated as PCC-M-N, where M is the total length of the chain and N is the number of correlated degrees of freedom).

In some case we also performed calculations in which we used a fully correlated small chain of few (5, 10 or 15) degrees of freedom. These results are reported to highlight the effect of the addition of a TD-SCF chain in the partially correlated chains. These model baths will be addressed as "truncated chains" (TC-N, where N is the number of degrees of freedom).

In both the partially correlated chains and the truncated chains, we adopted the same single particle scheme for the correlated degrees of freedom. The schemes for each number of correlated degrees of freedom and for all the model baths adopted are reported in Tab. 5.3 (relaxation calculations) and Tab. 5.4 (sticking calculations). Note that correlation schemes of the sticking calculations include a much larger number of single-particle functions. This is due to two different reasons. On one hand, in the sticking problems it is necessary to describe a stronger degree of correlation, as can be analogously seen for the normal bath models in Tab. 5.2. On the other hand, a higher number of single-particle functions is required since the system degrees of freedom x has to be treated as a single mode, due to a technical problems connected to the calculation of sticking probability with MCTDH package. However, last problem could be solved in future with the adoption of a different methodology for sticking simulations and hence a further reduction of the computational cost of these calculations could be achieved.

5.3.2 Relaxation and sticking models

To study energy relaxation, we considered an initial out-of-equilibrium bound state with an average position at a distance of 0.159 Å from the minimum of the potential well. Evolving the system in time, the wavepacket oscillates around the minimum and transfers energy to the the bath. During the propagation, we computed the total energy of the oscillating hydrogen as the sum

5 Correlated degrees of freedom

	All models
x, q_1, q_2	3
q_3, q_4, q_5	3

10 Correlated degrees of freedom

	All models
x, q_1, q_2	5
q_3, q_4, q_5	6
q_6, q_7, q_8	6
q_9, q_{10}	4

15 Correlated degrees of freedom

	Ohmic-50 and Garg	*Ohmic-100 and Ohmic-200*
$x, q_1 ... q_3$	8	11
$q_4 ... q_7$	10	12
$q_8 ... q_{11}$	10	10
$q_{12} ... q_{15}$	7	8

	PPV-Bump
x, q_1, q_2	5
$q_3 ... q_5$	6
$q_6 ... q_8$	6
$q_9 ... q_{11}$	6
$q_{12} ... q_{15}$	7

Table 5.3: Single particle scheme of the correlated degrees of freedom in the chain models for the relaxation calculations.

5 Correlated degrees of freedom

	Ohmic-100	*Ohmic-200 and PPV-Bump*	*Garg*
x	12	14	16
q_1, q_2, q_3	11	12	14
q_4, q_5	10	10	12

10 Correlated degrees of freedom

	Ohmic and PPV-Bump	*Garg*
x	14	18
q_1, q_2, q_3	12	14
q_4, q_5, q_6	10	10
$q_7 ... q_{10}$	9	9

15 Correlated degrees of freedom

	Ohmic and PPV-Bump	*Garg*
x	14	18
q_1, q_2, q_3	12	14
q_4, q_5, q_6	10	10
$q_7 ... q_{10}$	9	9
$q_{11} ... q_{15}$	8	8

Table 5.4: Single particle scheme of the correlated degrees of freedom in the chain models for the sticking calculations.

average momentum $\langle p \rangle$ / au	length L_{abs} / au	strength η / au
4	5.5	0.00008
6	5.5	0.00035
8	5.5	0.00070
10	5.5	0.00095
12	5.5	0.00120

Table 5.5: Parameters of the absorbing potential employed in the sticking simulations.

of the kinetic and the (non distorted) potential energy of the system plus half the coupling between the system and the bath:

$$E_{sys} = \langle \mathcal{H}_{sys} \rangle + \frac{1}{2} \langle V_{coupl} \rangle \tag{5.8}$$

We followed the relaxation dynamics until recurrence time was reached and the energy flowed back from the bath to the system.

For the same relaxation process, we also considered a quantity that may be expected to be more sensitive to approximations. We computed the quantum correlation of the position, defined as

$$C_x(t) = \langle x(t)x(0) \rangle \tag{5.9}$$

where $x(t)$ is the position operator in the Heisenberg picture. This correlation function can be computed by combining the results of different wavepacket propagations. In fact, $C_x(t)$ can be expressed as the matrix element

$$C_x(t) = \langle \psi_0 | e^{\imath Ht}\, x\, e^{-\imath Ht}\, x | \psi_0 \rangle = \langle \psi_t |\, x\, | \phi_t \rangle$$

which is just a matrix element between two independently evolving wavepacket: $|\psi_t\rangle = e^{-\imath Ht}\ |\psi_0\rangle$ is the normal wavefunction, while $|\phi_t\rangle = e^{-\imath Ht}\, x\, |\psi_0\rangle$ can be obtained by propagating a different initial wavefunction $|\phi_0\rangle = x\, |\psi_0\rangle$.

In the case of sticking simulations, the initial wavepacket for the system was placed far from the equilibrium position (precisely at 6.35 Å), in the asymptotic region of the potential. Different simulations were performed with var-

ious values of the incoming momentum: 4, 6, 8, 10 and 12 au, corresponding to hydrogen kinetic energy of 0.12, 0.27, 0.47, 0.74 and 1.07 eV respectively. We chose a wavepacket with a narrow momentum distribution, so that we can approximately assume that the wavefunction represents a particle with a definite kinetic energy corresponding to the average momentum of the wavepacket. Evolving in time, the H atom reaches the interaction well and a part of the energy is transferred to the bath. Consequently, a fraction of the wavepacket is trapped in the well, while the remaining is reflected by the repulsion wall and goes back to the asymptote, where is absorbed by a quadratic optical potential. Tab. 5.5 reports the length L_{abs} and the strength η of the absorbing potentials we adopted for each value of the average wavepacket momentum.

We followed the wavepacket evolution computing the projection of the wavepacket onto the bound states of the Morse potential

$$P_{bound} = \sum_{n=1}^{N_{bound}} |\langle n \mid \psi_t \rangle|^2 \tag{5.10}$$

As a function of time, the resulting bound state probability has the behavior shown in Fig. 5.3, reported here as an example. This probability is initially equal to zero since the wavepacket is far from the potential well. When the wavepacket reaches the potential well the probability increases until at long time a plateau is reached. The value of this plateau equals the fraction of the wavepacket which has been trapped in the adsorption potential, *i.e.* the sticking probability.

5.4 Results and Discussion

5.4.1 Energy relaxation

Fig.s 5.4, 5.5 and 5.6 show the results of the vibrational relaxation calculations. In each graph, the system energy is plotted as a function of time, for the simulations performed with the normal baths, the partially correlated chains and (where available) the truncated chains.

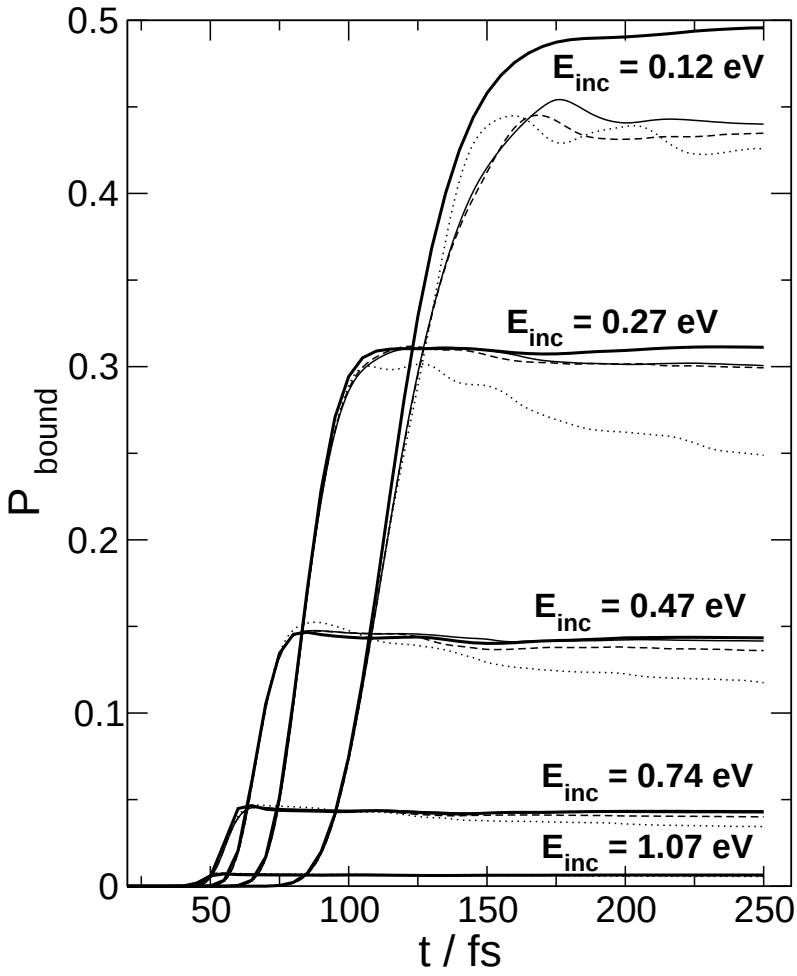

Figure 5.3: Bound state projection (Eq.5.10) as a function of time for the simulation of the OHMIC-100 sticking models. Results corresponding to different kinetic energies of the hydrogen atom are reported. The thick lines are the results obtained with a normal bath, while the other lines are the results with partially correlated chains: PCC-100-5 (dotted lines) PCC-100-10 (dashed lines) and PCC-100-15 (solid lines).

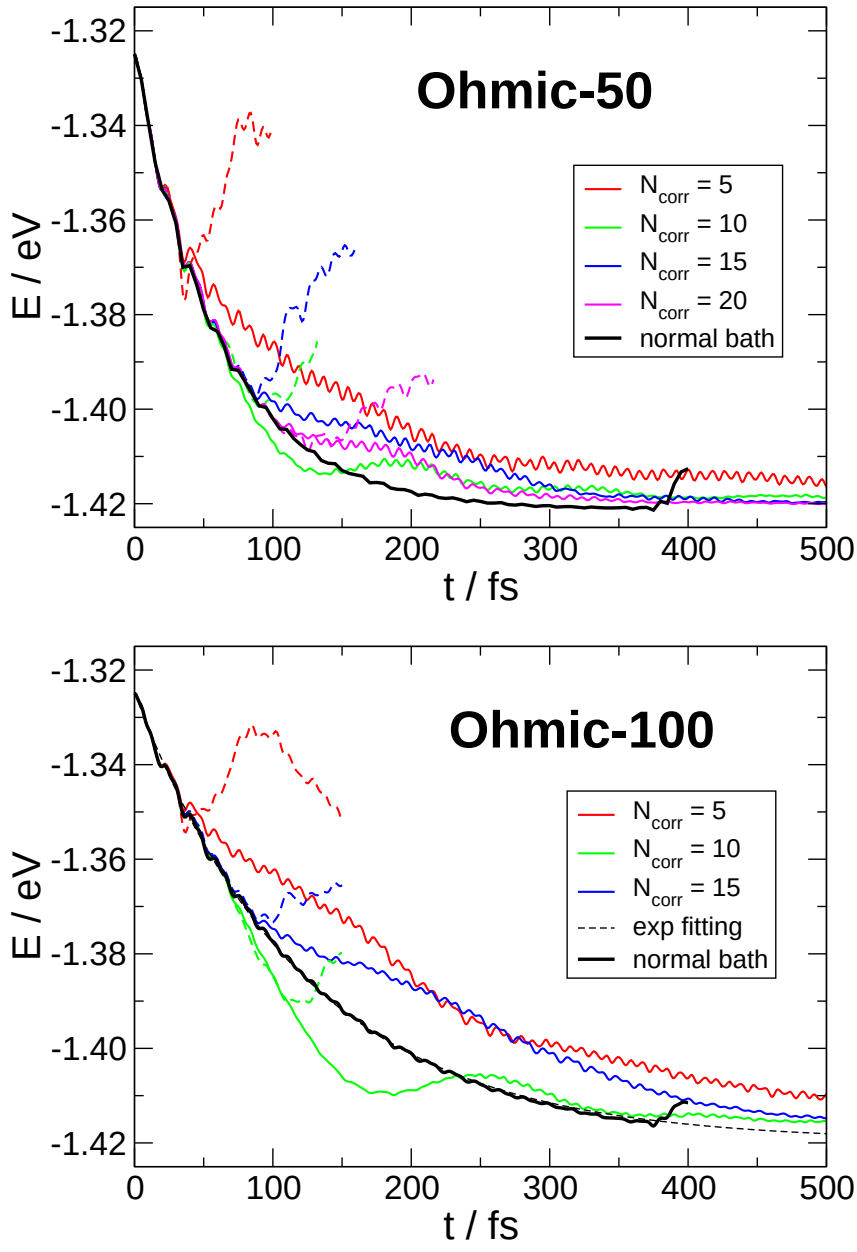

Figure 5.4: System energy (defined as in Eq.5.8) as a function of time for the relaxation calculations with the OHMIC-50 (top panel) and OHMIC-100 (lower panel) bath models. Each graphs show the results obtained with a normal bath (thick black line), partially correlated chains of 100 oscillators with variable number of correlated degrees of freedom (solid lines) and the corresponding truncated chains (dashed lines).

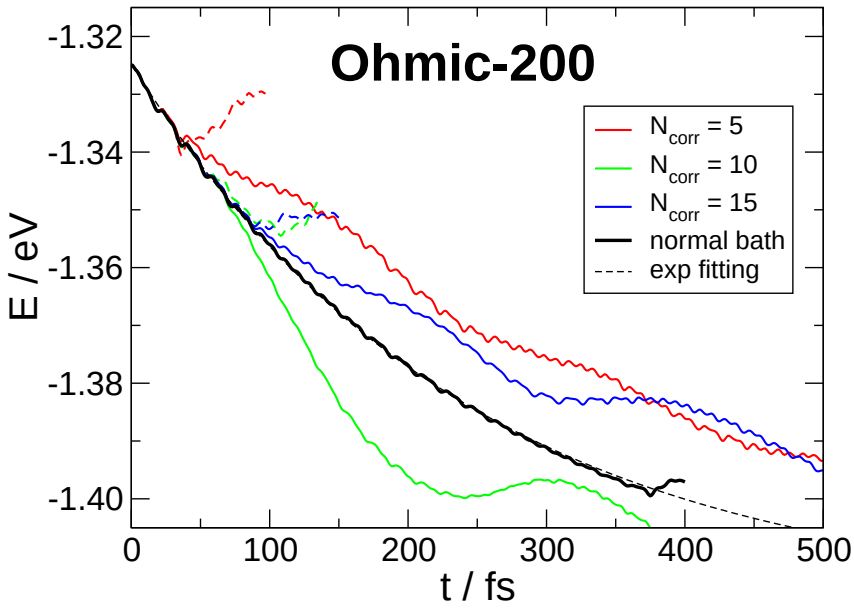

Figure 5.5: System energy (defined as in Eq.5.8) as a function of time for the relaxation calculations with the OHMIC-200 bath model. The graph shows the results obtained with a normal bath (thick black line), partially correlated chains of 100 oscillators with variable number of correlated degrees of freedom (solid lines) and the corresponding truncated chains (dashed lines).

Normal bath calculations predict that the energy relaxation curve in presence of an Ohmic bath is an exponentially decaying function, in agreement with what is expected for the corresponding Langevin dynamics. In fact, in this case energy dissipation has no memory effects, and Langevin equation at 0 K is essentially a damped oscillator, for which the classical relaxation is expected to follow an exponential decay. When memory effects are included, as in the two non Markovian cases considered in our work, the energy profile shows oscillations superimposed to the decay.

As evident from the graph, the normal calculations have the correct behavior until recurrence time is reached (between 350 fs and 400 fs). To describe the relaxation at longer times, it is necessary to increase the number of bath oscillators. This is extremely expensive for the bath in normal form, since all the new degrees of freedom needs to be correlated to the system itself. For

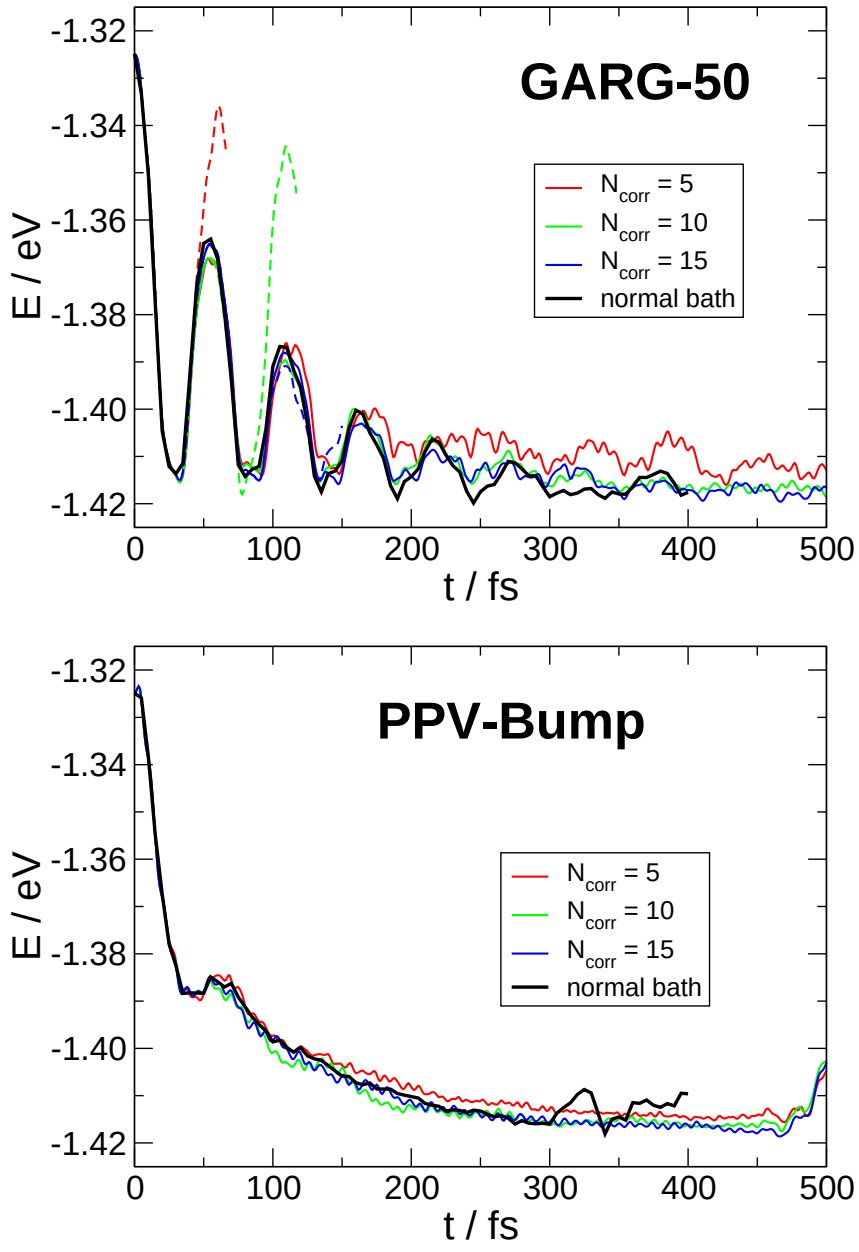

Figure 5.6: System energy (defined as in Eq.5.8) as a function of time for the relaxation calculations with the GARG-50 (top panel) and PPV-BUMP (lower panel) bath models. Each graphs show the results obtained with a normal bath (thick black line), partially correlated chains of 100 oscillators with variable number of correlated degrees of freedom (solid lines) and the corresponding truncated chains (dashed lines).

the calculations reported here, we are slightly below the limit of the computational resources available in our group.

The truncated chain results show that the linear chain and the normal bath are indeed equivalent. As long as the energy flows along the first degree of the chains and the dynamics of these oscillators is exactly described, the results are almost identical. When the recurrence time of the small chains is reached (approximately 5 fs per 5 correlated oscillators, regardless of the spectral properties of the bath), the energy gets back to the system and interfere with the relaxation dynamics.

Concerning the partially correlated chains, we see that when the energy flows along the first oscillators, the dynamics is again exactly reproduced. The length of this time regime is the very same as in the truncated chains. Then, the energy reaches the TD-SCF part of the chain and the dynamics is no longer exact. However the relaxation of the system proceed, and at long time reach a minimum which is in good agreement with the asymptote of the benchmark calculation.

The relaxation dynamics with the partially correlated chains differ from the normal bath benchmark in a way that is not easy to understand, sometimes underestimating and sometimes overestimating the exact value of energy. For the ohmic baths, the relaxation curves present an oscillatory behavior, which is reduced by increasing the number of correlated degrees of freedom. Comparing the results obtained for different values of the relaxation time, we see that for greater γ^{-1} we get worse results since a longer relaxation dynamics needs to be described. An excellent agreement is achieved for non-Ohmic baths: even with N_{corr} =10 we obtain almost exact results. This suggests that the partially correlated chain representation could be especially suitable for a realistic bath including memory effects.

For PPV-BUMP bath relaxation, we performed some tests to check the long time performances of the linear chain representation. The results are reported in Fig. 5.7 for chains of 100, 200 and 300 oscillators, with 10 or 15 fully correlated degrees of freedom. As can be seen, by increasing the length of the

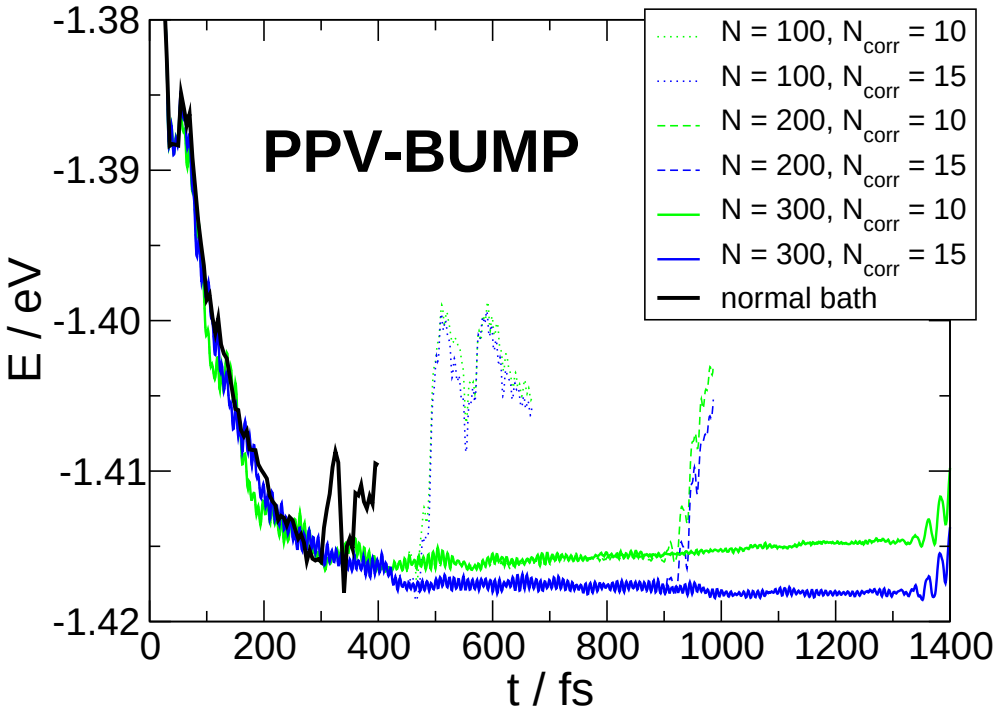

Figure 5.7: System energy (defined as in Eq.5.8) as a function of time for the long time relaxation calculations with the PPV-BUMP bath model. The graph reports the results obtained with a normal bath (black line) and partially correlated chains of 100 oscillators (dotted lines), 200 oscillators (dashed lines) and 300 oscillators (solid lines), each with 10 (green) or 15 (blue) correlated degrees of freedom.

chain, we manage to reach long recurrence time: approximately 460 fs for 100 oscillators, 905 fs for 200 oscillators, 1320 fs for 300 oscillators.

With 10 correlated degrees of freedom we get good results at short time, approximately up to 400 fs. On a large time scale, however, we see that before recurrence time is reached, a small amount of energy ($\sim 5\,meV$) is reflected back to the system and the energy slightly increases. As shown by the PCC-300-15 simulation this problem is solved by increasing the number of correlated degrees of freedom.

We remark that with $N_{corr} = 15$ we managed to properly describe the relaxation process for one picosecond with a calculation that lasted slightly

chain length	$N_{corr} = 10$	$N_{corr} = 15$
100	615.63 s	1,746.30 s
200	818.04 s	3,033.85 s
300	1,078.71 s	3,984.57 s

Table 5.6: CPU times of the PPV-Bump long chain calculations, for a 1 ps long dynamical simulation.

more than one hour. For a normal bath, a simulation with a similar recurrence time is far beyond the computational limits.

5.4.2 Computational performances

From a computational point of view, the calculations with the partially correlated chains reported here are considerably less time-consuming than the normal bath benchmarks. Table 5.6 reports the timings of the PPV-BUMP chain calculations, for which the results have already been reported and discussed (Fig. 5.7). Those values should be compared with a 400 fs propagation of the corresponding normal bath, which required a CPU time of 11,561.98 s.

Apart from the absolute amount of time, which is clearly much smaller for the linear chains, the most promising feature of linear chain calculation is the scaling with the length of the TD-SCF chain, that is approximately linear. In turn the length of the chain scales linearly with the recurrence time. Hence, as shown in Fig. 5.8, the recurrence time of the bath can be increased at a reasonable computational cost. On the contrary, as discussed above, the increase of the bath dimension in the case of a normal bath is extremely expensive and the computational limit is rapidly reached with less than 100 degrees of freedom.

5.4.3 Position correlation function

To check the performances of our methodology with a quantity which might be more sensitive to the approximation of the bath dynamics, we also considered the position quantum correlation function. The results for the OHMIC-50, GARG-50 and PPV-BUMP bath are reported in Fig. 5.9.

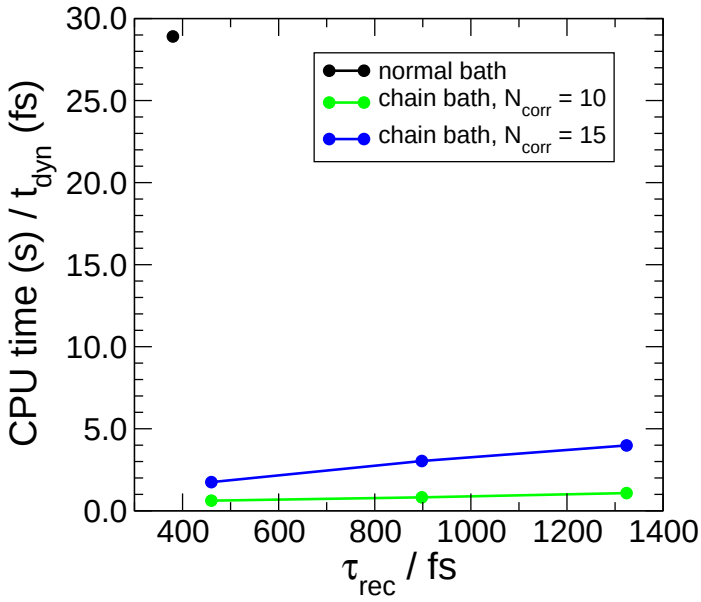

Figure 5.8: Timings of the PPV-BUMP relaxation calculation. On the horizontal axis, the recurrence time of the bath, estimated from the system energy behavior reported in Fig. 5.7. On the vertical axis, the ratio between the CPU time of the calculation (in s) and the final time of the simulation (in fs).

Also for this property, the results are very good: the chains almost exactly reproduce the normal bath behavior in a range of time which depends on the length of the correlated part. After this time, the correlation functions gradually differ in both phase and magnitude. Note that again the agreement is much better for non Markovian dynamics.

5.4.4 Sticking probability

With the technique described in section 5.3, we used the relaxation model to compute the sticking probability as a function of the incident energy. We obtained the curves that are shown in Fig. 5.10.

Focusing on the exact normal bath results, we see that in all the cases considered the sticking probability is higher when the incoming particle is slower, since relaxation is more efficient. Hence sticking probability monotonically decreases, as it is expected for a potential without any barrier to adsorption,

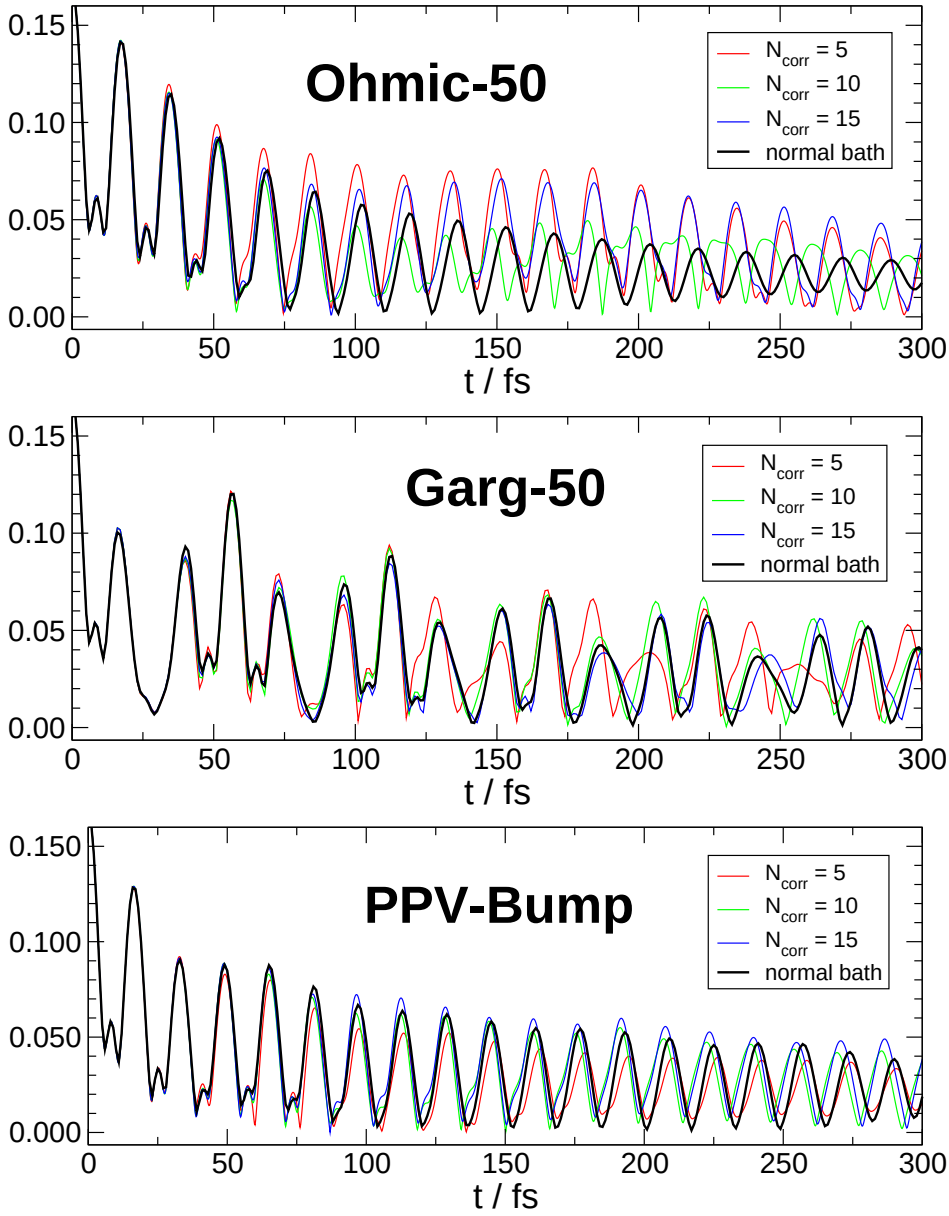

Figure 5.9: Position correlation function (defined as in Eq.5.9) as a function of time for the relaxation calculations with the OHMIC-50, GARG-50 and PPV-BUMP bath models (from top to bottom). Each graphs show the results obtained with a normal bath (thick black line) and partially correlated chains of 100 oscillators with variable number of correlated degrees of freedom (red, green and blue solid lines).

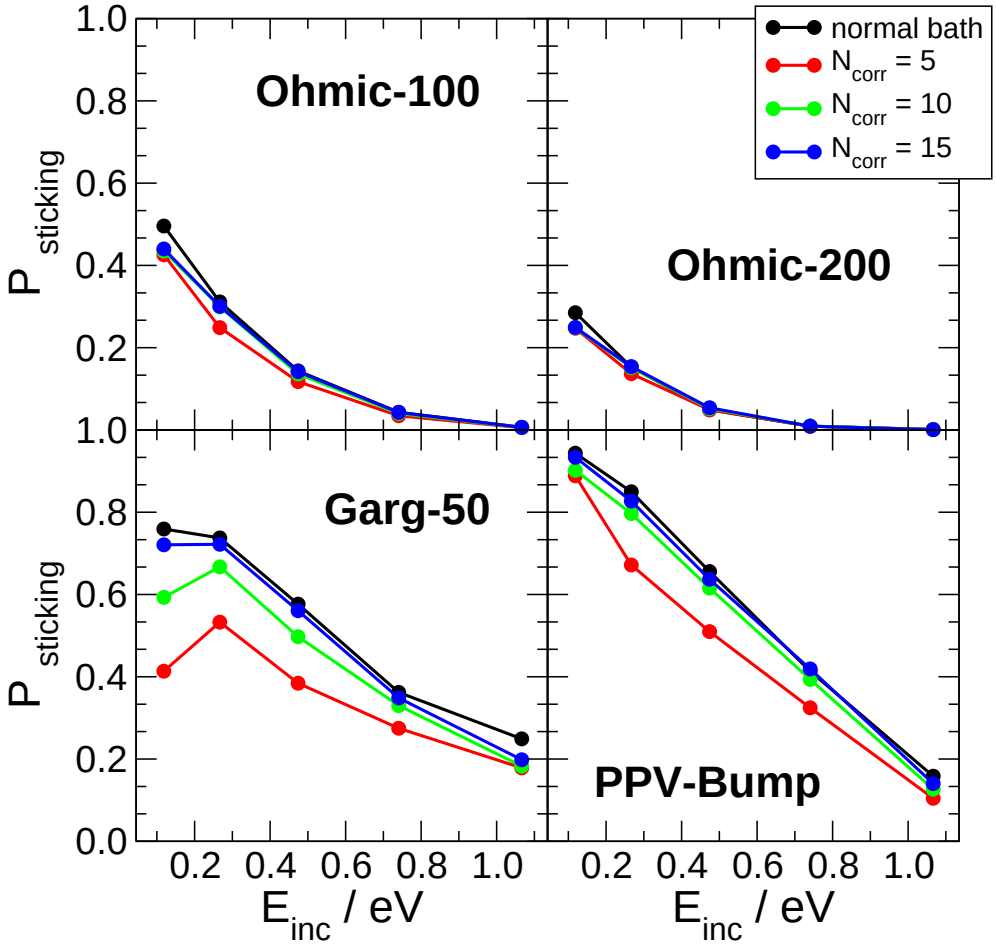

Figure 5.10: Sticking probability as a function of the incident energy, for the OHMIC-100, OHMIC-200, GARG-50 and PPV-BUMP bath models (as reported in the figure). In each panel, we report the results obtained with a normal bath (in black) and those obtained with a partially correlated chain of 100 oscillators with variable number of correlated degrees of freedom ($N_{corr} = 5$ in red, $N_{corr} = 10$ in green and $N_{corr} = 15$ in blue).

such as the Morse function. For the Ohmic baths, the sticking probability has an exponential behavior, in agreement with previous results obtained for similar models [20]. On the contrary, it is interesting to note that when a non Ohmic bath is considered, the shape of the sticking curve is different, linear in a wide range. This suggests that even when the relaxation dynamics is only indirectly considered, Markovian approximations might not be adequate and memory effects should be properly taken into account.

With respect to the partially correlated chains, the results are in excellent agreement with the benchmark calculations. When we adopt 5 correlated degrees of freedom, the shape of the sticking curve is already reasonably reproduced (at a very low computational cost). The points obtained with 15 degrees of freedom are almost indistinguishable from the exact results. This fact is well understood if we consider that in the scattering event, relaxation needs to be described only as long as the wavepacket is in the interaction region. Two property of the bath model are essential: (1) the short time relaxation dynamics needs to be exactly described and (2) the recurrence time should be long enough to prevent the trapped fraction of the wavepacket to get out of the potential well. As shown by the relaxation tests reported above, these are indeed the properties ensured by the partially correlated chains approximation. In agreement with this point, for E_{inc} = 0.12 eV a small discrepancy is always observed, since in this case the scattering wavepacket spends a long time in the adsorption well and a longer relaxation dynamics needs to be described.

5.5 Conclusions

In this work, we considered the vibrational relaxation and sticking processes for a Morse potential coupled to a thermal bath with different spectral densities, in accordance with the well known Caldeira-Leggett model of dissipative dynamics. By means of MCTDH, we studied these dynamical phenomena comparing the usual representation of the bath degrees of freedom with

a novel effective mode representation [14, 16–19]. This equivalent formulation of the Caldeira-Leggett Hamiltonian allows an approximation scheme in which a large number of oscillators is included and only a small number of them is fully described, while the others are treated at a mean-field level. Within MCTDH framework, this approximate description is conveniently applied with a TD-SCF *ansatz* for the mean-field part of the chain.

For the relaxation problems considered, we computed the energy of the system and the position correlation function as a function of time. We observed that with our approximation the dynamics is exactly reproduced at short time. For longer time some discrepancies appear, even if a reasonable agreement is always observed, in particular for non Markovian relaxation models. In addition to the reduced computational cost, we showed that this approach has a very important advantage: the CPU time of the calculation scales linearly with the number of bath oscillators. This property allows us to enlarge the bath (and hence increase the recurrence time) without incurring in the severe limit on the number of degrees of freedom which is typical of (both exact and approximate) quantum dynamics.

Furthermore, we showed that the two properties remarked - the exact short time dynamics and the possibility to increase the recurrence time - are the essential characteristics that are needed to simulate processes like sticking, in which the energy relaxation is only indirectly taken into account. The tests we performed with our bath models showed that an excellent agreement can be achieved at a very low computational cost.

In conclusion, in this work we have presented and applied a very promising approximate methodology, which can be applied within Caldeira-Leggett dissipative models to reduce the computational costs of the simulations and avoid recurrence problems related to the finite size of the bath. A future development of this work will be the application of this technique to a realistic sticking problem, in which both the system potential and the spectral density of the bath are chosen to describe the dynamical properties of a gas-surface problem.

Bibliography

[1] G. W. Ford, J. T. Lewis and R. F. O'Connell, *Phys. Rev. A* **37**, 4419 (1988).

[2] A. O. Caldeira and A. J. Leggett, *Phys. Rev. Lett.* **46**, 211 (1981).

[3] K. Blum, *Density matrix theory and applications*, Physics of atoms and molecules, Plenum Press (1996).

[4] H. Breuer and F. Petruccione, *The Theory of Open Quantum Systems*, Oxford University Press (2007).

[5] A. O. Caldeira and A. J. Leggett, *Phys. Rev. A* **31**, 1059 (1985).

[6] R. Zwanzig, *J. Stat. Phys.* **9**, 215 (1973), 10.1007/BF01008729.

[7] H.-D. Meyer, U. Manthe and L. S. Cederbaum, *Chem. Phys. Lett.* **165**, 73 (1990).

[8] M. H. Beck, A. Jäckle, G. A. Worth and H.-D. Meyer, *Phys. Rep.* **324**, 1 (2000).

[9] H.-D. Meyer, F. Gatti and G. A. Worth, editors, *Multidimensional Quantum Dynamics: MCTDH Theory and Applications*, Wiley-VCH, Weinheim (2009).

[10] G. A. Worth, H.-D. Meyer and L. S. Cederbaum, *J. Chem. Phys.* **109**, 3518 (1998).

[11] M. Nest and H.-D. Meyer, *J. Chem. Phys.* **119**, 24 (2003).

[12] I. Burghardt, M. Nest and G. A. Worth, *J. Chem. Phys.* **119**, 5364 (2003).

[13] R. Martinazzo, M. Nest, P. Saalfrank and G. F. Tantardini, *J. Chem. Phys.* **125**, 194102 (2006).

[14] K. H. Hughes, C. D. Christ and I. Burghardt, *J. Chem. Phys.* **131**, 024109 (2009).

[15] S. López-López and M. Nest, *J. Chem. Phys.* **132**, 104103 (2010).

[16] L. S. Cederbaum, E. Gindensperger and I. Burghardt, *Phys. Rev. Lett.* **94**, 113003 (2005).

[17] K. H. Hughes, C. D. Christ and I. Burghardt, *J. Chem. Phys.* **131**, 124108 (2009).

[18] R. Martinazzo, B. Vacchini, K. H. Hughes and I. Burghardt, *J. Chem. Phys.* **134**, 011101 (2011).

[19] R. Martinazzo, K. H. Hughes and I. Burghardt, *Phys. Rev. E* **84**, 030102 (2011).

[20] S. López-López, M. Nest and R. Martinazzo, *J. Chem. Phys.* **134**, 014102 (2011).

[21] N. Pottier, *Nonequilibrium statistical physics: linear irreversible processes*, Oxford Graduate Texts, Oxford University Press (2010).

[22] A. Garg, J. N. Onuchic and V. Ambegaokar, *J. Chem. Phys.* **83**, 4491 (1985).

[23] F. Sterpone, R. Martinazzo, A. N. Panda and I. Burghardt, *Z. Phys. Chem.* **225**, 541 (2011).

[24] G. A. Worth, M. H. Beck, A. Jäckle and H.-D. Meyer, The MCTDH Package, Version 8.4 (2007). See http://mctdh.uni-hd.de.

Appendix A

Quantum Scattering Theory

In this appendix some key concepts and some applications of quantum scattering theory will be presented. This approach is the natural theoretical background of experiments in which a beam of incoming particle is scattered by the interaction with something else (other particles, a surface, a crystal, *etc.*).

The starting point is splitting the system Hamiltonian in two terms

$$H = H_0 + V \tag{A.1}$$

a *free Hamiltonian* H_0 and an *interaction Hamiltonian* V. For $t \to \pm\infty$ we assume that the system is described by an asymptotic state, that evolves according to H_0. For finite times, the system feels also the interaction and evolves according to the total Hamiltonian H.

As an example, two colliding particles[1] interacting with a potential V will be described by the Hamiltonian

$$H = T_1 + T_2 + V_{12}$$

where T_i is the kinetic energy operator of the i^{th} particle. In this case the obvious choice is to set the free Hamiltonian $H_0 = T_1 + T_2$, *i.e.* the evolution of the non interacting particles.

[1] in this example we assume no internal degrees of freedom, e.g. we can consider two atoms from a "chemical" point of view

As further example, we consider the full Hamiltonian of a diatomic molecule in an external potential, such as the interaction of the molecule with a surface, which can be written as

$$H = T_{trasl}(\mathbf{R}) + T_{rot+vib}(\mathbf{r}) + V_{internal}(\mathbf{r}) + V_{ext}(\mathbf{R}, \mathbf{r})$$

where $\mathbf{R}$ and $\mathbf{r}$ are respectively the coordinates of the center of mass and the vector distance between the two atoms (in spherical coordinates the bond length r and the orientation angles φ, ϑ). If we assume that in the scattering process the molecule does not dissociate, we can set $H_0 = T_{trasl}(\mathbf{R}) + T_{rot+vib}(\mathbf{r}) + V_{internal}(\mathbf{r})$. In this way the free evolution will describe the translation and the rotation of the molecule.

In a scattering experiment, the information that are accessible are the state in which the system is prepared (which we will call the *incoming asymptote*) and the properties measured after the scattering (the *outcoming asymptote*). On the other hand, theoretical methods let us describe how the system evolves according to the full potential, and the link between the actual state and the asymptotic states may not be trivial. One of the goal of scattering theory is to relate the interaction potential to the transition probabilities between the asymptotic states.

In the following we will very often make use the free Hamiltonian eigenstates. Before going on, a comment on the notation is needed. In general free Hamiltonian eigenstates are a combination of two parts: a plane wave for the scattering coordinate (*e.g.* the relative distance of two colliding particle, or the center of mass of the molecule experiencing the external potential) and another part for the other degrees of freedom. In the following we will generally write the free Hamiltonian eigenstates as

$$|\mathbf{p}\alpha\rangle\,,\ |\mathbf{p}'\beta\rangle\,,\ |\mathbf{p}''\gamma\rangle\,,\ \ldots$$

where the the letter $\mathbf{p}$ is the momentum associated to the plane wave and the Greek letter is a collective index labelling the quantum state for the other coordinates. For the sake of convenience, we will assume α to be discrete. This is

not always true, *e.g.* the vibrational states of the molecule become continuous in the dissociation limit. Anyway, the generalization of the equations in this sense is usually straightforward and implies the substitution of the sum over α with an integral.

I will just discuss the main definitions and those aspects which are more related to the problems of scattering of molecules on surfaces. For a more comprehensive and thorough discussion of scattering theory, we refer to the books by J.R.Taylor [1] and by R.G. Newton [2].

A.1 Time dependent formalism

A.1.1 Time evolution operator

According to Quantum Mechanics postulates, time evolution of a state is described by *time dependent Schrödinger equation*:

$$H\,|\psi\rangle = \imath\hbar\frac{\partial\,|\psi\rangle}{\partial t} \tag{A.2}$$

The first step in the development of a quantum description of an evolving system is expressing this differential equation with a continuous group of operators describing the time dependence of the system, the *time evolution operators*. We briefly recall some useful properties of such operator group (for an exhaustive discussion see Ref. [3]).

Schrödinger equation is a first-order linear differential equation: given an initial condition, the solution is uniquely determined at any time. Hence we can define the time evolution of a system with a *time evolution operator* $U(t)$, such that

$$|\psi_{\tau+t}\rangle = U(t)\ |\psi_\tau\rangle \tag{A.3}$$

where $|\psi_{\tau+t}\rangle$ is the wave-function at time $\tau + t$ and $|\psi_\tau\rangle$ is the wave-function at time τ. Time evolution operators are linear unitary operators satisfying the composition relation

$$U_{t_1+t_2} = U_{t_1}U_{t_2}$$

From the unitarity and the composition relation we can relate the evolution for positive times and negative times

$$U_t^\dagger = U_{-t}$$

Substituting Eq. (A.3) in Schrödinger equation we get

$$HU(t)\ |\psi\rangle = \imath\hbar \frac{\partial\left(U(t)\ |\psi\rangle\right)}{\partial t}$$

which can be rewritten as an operator equivalence:

$$\frac{\partial}{\partial t}U(t) = -\frac{\imath}{\hbar}H\,U(t)$$

In our case, H does not have an explicit dependence on time and the equation can be formally integrated, giving a very simple and useful expression for the time evolution operator

$$U(t) = \exp\left(-\frac{\imath}{\hbar}Ht\right) \tag{A.4}$$

As for the full Hamiltonian, we can build a time evolution operator corresponding to the free Hamiltonian H_0, which is solution of Schrödinger equation for the non-interacting system and can be written as

$$U_0(t) = \exp\left(-\frac{\imath}{\hbar}H_0t\right) \tag{A.5}$$

when the free Hamiltonian does not depend explicitly on time, as in our case.

A.1.2 Møller operators and S matrix

A scattering experiment can be idealized in the following way. The system is initially prepared in a state which is a combination of free eigenstates $|\mathbf{p}\alpha\rangle$. For the results to be as detailed as possible, we want this incoming asymptote to be prepared in a well defined quantum state α, or at least to be characterized by a very narrow distribution. Long time before the interaction takes place, the system evolves according to $U_0(t)$, since in this asymptotic regime $V(\mathbf{x}_{asym}) = 0$. When the interaction is "switched on" (*e.g.* the particles collide,

or the molecule reach the surface) the evolution of the system is given by the full Hamiltonian $U(t)$, whose effect is usually to couple degrees of freedom which are uncoupled in the free evolution. Long time after the interaction, the state will be a superposition of free eigenstates $|\mathbf{p}\alpha\rangle$ possibly different from the initial one and evolving according to $U_0(t)$ again.

The relevant information that can be extracted from this experiment, is the probability for the system to go from the initial state $|\mathbf{p}\alpha\rangle$ to one other free state $|\mathbf{p}'\beta\rangle$

$$w(\mathbf{p}\alpha \leftarrow \mathbf{p}'\beta)$$

For this purpose, we need some tools to relate the incoming and outcoming asymptotes to the interacting system. These tools are *Møller operators*, defined as

$$\Omega_{\pm} = \lim_{t \to \mp\infty} U(t)^{\dagger} U_0(t) \tag{A.6}$$

For a detailed discussion of the conditions under which the definition makes sense and a review of the mathematical properties of Møller operators, the reader should refer to Ref. [1].

In the present discussion, we will just give a heuristic justification of this definition. The operator Ω_+ can be viewed as the product $U(-\infty)^{\dagger} U_0(-\infty)$, *i.e.* an operator that evolves a state vector from $t = 0$ to $t = -\infty$ as a free state and then from $t = -\infty$ to $t = 0$ as an interacting state. The idea is that Ω_+ maps a free state evolving from the incoming asymptote in absence of the interaction to the state that would evolve from the same asymptote in the presence of the interaction potential. The same holds for Ω_- and the outcoming asymptote. Schematically,

$$\begin{array}{ccccc} \text{in asymptote} & & \text{actual state} & & \text{out asymptote} \\ |\Psi\rangle & \xrightarrow{\Omega_+} & |\Psi+\rangle & & \\ & & |\Psi-\rangle & \xleftarrow{\Omega_-} & |\Psi\rangle \end{array}$$

We aim at finding an expression of the probability $w(\mathbf{p}\alpha \leftarrow \mathbf{p}'\beta)$. This transition probability will be the overlap between $|\mathbf{p}\alpha-\rangle$ (the actual state evolving

to the asymptote $|\mathbf{p}\alpha\rangle$) and $|\mathbf{p}'\beta+\rangle$ (the actual state evolving from the asymptote $|\mathbf{p}'\beta\rangle$)

$$w(\mathbf{p}\alpha \leftarrow \mathbf{p}'\beta) = \left|\langle \mathbf{p}\alpha- \,|\, \mathbf{p}'\beta+\rangle\right|^2$$

With Møller operators we have a way to write the unknown actual states in terms of the free states

$$|\mathbf{p}'\beta+\rangle = \Omega_+ \, |\mathbf{p}'\beta\rangle \qquad |\mathbf{p}\alpha-\rangle = \Omega_- \, |\mathbf{p}\alpha\rangle$$

and the transition probability is conveniently expressed as

$$w(\mathbf{p}\alpha \leftarrow \mathbf{p}'\beta) = \left|\left\langle \mathbf{p}\alpha \,\middle|\, \Omega_+^\dagger \Omega_- |\mathbf{p}'\beta+\right\rangle\right|^2 \tag{A.7}$$

This is the main idea of scattering theory: we have expressed the transition probability between asymptotic states as the squared modulus of the matrix element of a *scattering operator S*, defined as

$$S = \Omega_+^\dagger \Omega_- \tag{A.8}$$

I just mention two interesting properties involving the operators introduced so far:

1. Møller operators satisfy the so-called *intertwining relation*

$$H\Omega_\pm = \Omega_\pm H_0 \tag{A.9}$$

2. The S operator commutes with the free Hamiltonian H_0

$$[H_0; S] = 0 \tag{A.10}$$

hence, as expected on a physical basis, scattering is possible only between asymptotic states with the same total energy.

3. For later convenience, by projecting the S operator on the free Hamiltonian eigenstates, we decompose it in an elastic term (satisfying momentum conservation) and an inelastic term (still subjected to energy conservation), according to the formula

$$\langle \mathbf{p}\alpha \,|\, S|\mathbf{p}'\beta\rangle = \delta_{\alpha\beta}\delta(\mathbf{p}-\mathbf{p}') + 2\imath\pi\,\delta(E_{\alpha\mathbf{p}} - E_{\beta\mathbf{p}'})t(\mathbf{p}\alpha \leftarrow \mathbf{p}'\beta) \tag{A.11}$$

where $t(\mathbf{p}\alpha \leftarrow \mathbf{p}'\beta)$ - defined by the last expression - is called *on-shell t matrix*.

A.2 Time independent formalism

In the previous section, we have defined the main tools of scattering theory in terms of the evolution operators, hence from a time dependent point of view. The same theoretical scheme can be built in a time independent fashion, starting from the transformation of the dynamical operator from the time to the energy domain. In this section we will introduce the main object of time independent scattering theory, the T operator, and then we will show how it can be related to the scattering operator.

A.2.1 Green operator

We introduce the *Green operator*, defined as

$$G(z) = \begin{cases} -\imath \int_{-\infty}^{0} dt \, \exp\left(-\imath(z-H)t\right) = G^{+}(z) & Im\, z > 0 \\ +\imath \int_{0}^{+\infty} dt \, \exp\left(-\imath(z-H)t\right) = G^{-}(z) & Im\, z < 0 \end{cases} \tag{A.12}$$

where the superscript $\pm$ indicates the restriction of $G(z)$ to the upper or lower complex half-plane.

When $Re\, z$ does not belong to the spectrum of H

$$\lim_{\varepsilon \to 0^{+}} G^{+}(x + \imath\varepsilon) = \lim_{\varepsilon \to 0^{+}} G^{-}(x - \imath\varepsilon) = G(x)$$

Otherwise $G(x)$ is not defined, and

$$\lim_{\varepsilon \to 0^{+}} G^{+}(x + \imath\varepsilon) \neq \lim_{\varepsilon \to 0^{+}} G^{-}(x - \imath\varepsilon)$$

Basically, $G^{+}(z)$ and $G^{-}(z)$ are a complex extension of the Fourier transform of the $t > 0$ and $t < 0$ restriction of the time evolution operator. In this sense it should be reasonably accepted that they are an alternative time-independent way of describing the dynamics of the system.

The necessity to let $z \in \mathbb{C}$ (and not just a physical meaningful real energy) comes from the fact that the operator is not defined for z in the spectrum of H. Hence in the manipulation of the equations involving the green operator is often convenient to take $Im\, z \neq 0$ and then let $Im\, z \to 0$ after integration.

This is equivalent to introduce a dumping factor $e^{-\varepsilon t}$ in the integrals (*e.g.* in Eq. A.12, putting $z = x + i\varepsilon$) and then to let $\varepsilon \to 0$ (and $e^{-\varepsilon t} \to 1$).

Formally, if z is not in the spectrum of H, we can integrate Eq. A.12

$$G(z) = \frac{1}{z - H} \tag{A.13}$$

This representation is a very common definition of $G(z)$, and is indeed a convenient form to compute its matrix element (as long as z is not in the spectrum of H).

In the following we will make use of both the green operator corresponding to the full Hamiltonian H and the free Hamiltonian H_0. As usual we will distinguish them with a 0 subscript:

$$G_0(z) = \frac{1}{z - H_0}$$

Useful formulas relating $G(z)$ and $G_0(z)$ are

$$G(z) = G_0(z) + G_0(z)VG(z) \tag{A.14}$$

$$G(z) = G_0(z) + G(z)VG_0(z) \tag{A.15}$$

which can be directly proved by substituting $V = (H + z) - (H_0 - z)$.

A.2.2 The operator T

We define the *operator* $T(z)$ ($z \in \mathbb{C}$) as

$$T(z) = V + V\,G(z)\,V \tag{A.16}$$

As a function of z, the T operator has the same analytical properties of the Green operator. As we already mentioned, and as we shall see later, our interest in T lies in the fact that it can be directly related to the scattering probability.

From equations A.14 and A.15 and the definition of $T(z)$, we can find other useful relations concerning $T(z)$

$$T(z)\,G_0(z) = V\,G(z) \tag{A.17}$$

$$G_0(z)\,T(z) = G(z)\,V \tag{A.18}$$

With the first relation, we can substitute the operator $G(z)$ from the definition of $T(z)$ and get

$$T(z) = V + V\,G_0(z)\,T(z) \tag{A.19}$$

which is known as *Lippmann-Schwinger equation* for $T(z)$. This equation is the cornerstone of the perturbative approach to scattering problems, but we will not develop further this topic (the interested reader should refer to Chapter 9 of Taylor's book).

A.2.3 S matrix and T matrix

As we mentioned before, the $T(z)$ operator can be directly related to the S operator. First we need to obtain an integral representation of the S.

From its definition in terms of Møller operators

$$S = \Omega_-^\dagger\,\Omega_+ = \lim_{t\to+\infty}\lim_{t'\to-\infty} U_0^\dagger(t)\,U(t)\,U^\dagger(t')\,U_0(t')$$

If both limits exists, they can be taken simultaneously

$$S = \lim_{t\to-\infty} U_0^\dagger(-t)\,U(-t)\,U^\dagger(t)\,U_0(t) = \lim_{t\to-\infty} U_0(t)\,U^\dagger(2t)\,U_0(t)$$

Differentiating the expression,

$$\frac{d}{dt}U_0(t)\,U^\dagger(2t)\,U_0(t) = +\imath U_0(t)\left[VU^\dagger(2t) + U^\dagger(2t)V\right]U_0(t)$$

Introducing a dumping factor that will be necessary for further manipulations, we can develop the following integral equation for S

$$S = \mathbb{I} + \imath\lim_{\varepsilon\to0^+}\int_{-\infty}^{0} dt\,e^{+\varepsilon t}e^{-\imath H_0 t}\left[V\,e^{2\imath H t} + e^{2\imath H t}V\right]e^{-\imath H_0 t} \tag{A.20}$$

Now we can compute the S matrix element for two free Hamiltonian eigenstates $|\beta\mathbf{p}'\rangle$ and $|\alpha\mathbf{p}\rangle$

$$\langle\beta\mathbf{p}'\,|\,S|\alpha\mathbf{p}\rangle = \langle\beta\mathbf{p}'\,|\,\alpha\mathbf{p}\rangle +$$

$$-\frac{1}{2}\lim_{\varepsilon\to0^+}\left\langle\beta\mathbf{p}'\right|VG\left(\frac{E_{\alpha\mathbf{p}}+E_{\beta\mathbf{p}'}}{2}+\imath\frac{\varepsilon}{2}\right)+G\left(\frac{E_{\alpha\mathbf{p}}+E_{\beta\mathbf{p}'}}{2}+\imath\frac{\varepsilon}{2}\right)V\left|\alpha\mathbf{p}\right\rangle$$

where we have recognized the definition of Green operator

$$\imath \int_{-\infty}^{0} dt\, \exp\left(-\imath \left(E_{\alpha\mathbf{p}} + E_{\beta\mathbf{p}'} + \imath\varepsilon - 2H\right) t\right) = -\frac{1}{2} G\left(\frac{E_{\alpha\mathbf{p}} + E_{\beta\mathbf{p}'}}{2} + \imath\frac{\varepsilon}{2}\right)$$

Employing Eq. A.17 and A.18, the second term of the equation becomes

$$\lim_{\varepsilon\to 0^+} \left\langle \beta\mathbf{p}' \,\middle|\, T(\tilde{E} + \imath\frac{\varepsilon}{2}) G_0(\tilde{E} + \imath\frac{\varepsilon}{2}) + G_0(\tilde{E} + \imath\frac{\varepsilon}{2}) T(\tilde{E} + \imath\frac{\varepsilon}{2}) |\alpha\mathbf{p}\right\rangle$$

with $\tilde{E} = (E_{\alpha\mathbf{p}} + E_{\beta\mathbf{p}'})/2$. Now we can let G_0 act on the ket obtaining

$$\lim_{\varepsilon\to 0^+} \left(\frac{1}{\tilde{E} + \imath\frac{\varepsilon}{2} - E_{\beta\mathbf{p}'}} + \frac{1}{\tilde{E} + \imath\frac{\varepsilon}{2} - E_{\alpha\mathbf{p}}}\right) \left\langle \beta\mathbf{p}' \,\middle|\, T(\tilde{E}) |\alpha\mathbf{p}\right\rangle$$

With some simple manipulations, we can recognize in this expression one of the standard representation of Dirac delta as limit of a Lorentzian distribution

$$\lim_{\varepsilon\to 0^+} \left(\frac{2}{E_{\alpha\mathbf{p}} - E_{\beta\mathbf{p}'} + \imath\varepsilon} - \frac{2}{E_{\alpha\mathbf{p}} - E_{\beta\mathbf{p}'} - \imath\varepsilon}\right) = -4\imath\pi \lim_{\varepsilon\to 0^+} \frac{1}{\pi} \frac{\varepsilon}{(E_{\alpha\mathbf{p}} - E_{\beta\mathbf{p}'})^2 + \varepsilon^2} =$$

$$= -4\imath\pi\delta(E_{\alpha\mathbf{p}} - E_{\beta\mathbf{p}'})$$

In conclusion, the S matrix element is related to T matrix element by

$$\left\langle \alpha p \,\middle|\, S|\beta p'\right\rangle = \delta_{\alpha\beta}\delta(\mathbf{p} - \mathbf{p}') + 2\imath\pi\, \delta(E_{\alpha\mathbf{p}} - E_{\beta\mathbf{p}'})\, \left\langle \beta\mathbf{p}' \,\middle|\, T(E_{\alpha\mathbf{p}} + \imath 0^+) |\alpha\mathbf{p}\right\rangle \tag{A.21}$$

Comparing last expression with Eq. A.11 we see that the already introduced on-shell t matrix coincides with the matrix element of the T operator:

$$\left\langle \beta\mathbf{p}' \,\middle|\, T(E_{\alpha\mathbf{p}} + \imath 0^+) |\alpha\mathbf{p}\right\rangle = t(\mathbf{p}\alpha \leftarrow \mathbf{p}'\beta) \tag{A.22}$$

A.3 Scattering states

A.3.1 Definition

The *scattering states* $|\mathbf{p}\pm\rangle$ are improper H eigenvectors, that can be used to describe the scattering event from a time independent perspective. In the applications, they can be employed in two alternative approaches: 1) they are solution of an integral equation which is the analogous of Lippmann-Schwinger

equation for the operator T, 2) they are stationary solutions of Schrödinger equation, with appropriate boundary conditions.

Scattering states arise in a natural way, as those time independent interacting states corresponding to the asymptotic free states. We assume that the scattering system that at $t \to -\infty$ or $t \to +\infty$ can be expressed as the superposition of free states

$$|\phi\rangle = \int \phi(\mathbf{p}) \, |\mathbf{p}\rangle$$

In analogy with this expression, we introduce two sets of improper eigenstates $|\mathbf{p}\pm\rangle$, the scattering states, such that

$$|\phi\pm\rangle = \int \phi(\mathbf{p}) \, |\mathbf{p}\pm\rangle$$

Substituting the two expressions above in the equation relating the asymptote to the actual state, namely $|\phi\pm\rangle = \Omega_\pm \, |\phi\rangle$, we find that the scattering states have to satisfy the relation

$$\int \phi(\mathbf{p}) \, |\mathbf{p}\pm\rangle = \Omega_\pm \int \phi(\mathbf{p}) \, |\mathbf{p}\rangle \tag{A.23}$$

The last expression is the rigorous definition of asymptotic states. For the sake of brevity, we will write:

$$|\mathbf{p}\pm\rangle = \Omega_\pm \, |\mathbf{p}\rangle \tag{A.24}$$

We just mention two properties of the scattering states:

- The scattering states are (improper) eigenfunctions of the full Hamiltonian with the same eigenvalue as their corresponding free states

  $$\text{if } H_0 \, |\mathbf{p}\rangle = E^0 \, |\mathbf{p}\rangle \;\Rightarrow\; H \, |\mathbf{p}\pm\rangle = E^0 \, |\mathbf{p}\pm\rangle \tag{A.25}$$

  as can be proved by means of the intertwining relation.

- The scattering states satisfy the following relation

  $$T(E_\mathbf{p} \pm \imath 0^+) \; |\mathbf{p}\rangle = V \; |\mathbf{p}\pm\rangle \tag{A.26}$$

We want to remark that the definition of scattering eigenstates (Eq. A.24) does not hold in a strict sense. As an example, from that expression we could conclude that the scattering states evolve asymptotically as free states

$$U(t)\,|\mathbf{p}\pm\rangle \overset{t\to\mp\infty}{\longrightarrow} U_0(t)\,|\mathbf{p}\rangle$$

which is clearly false, since the scattering states are eigenvectors of the full Hamiltonian H and hence are stationary states. Last example shows that a particular care must be paid when dealing with improper states. As long as this fact is kept in mind, it is however convenient to think to the scattering states $|\mathbf{p}\pm\rangle$ as the actual states evolving from/to the free particle state $|\mathbf{p}\rangle$.

A.3.2 Lippmann-Schwinger equation for scattering states

In an analogous way as we did before, we want to express the definition of scattering state as an integral equation. With the same procedure adopted to derive the expression of the S operator in terms of the T operator (see Section A.2.3), we can write Ω_+ in the integral form

$$\Omega_+ = \mathbb{I} - \imath \lim_{\varepsilon\to 0^+} \int_{-\infty}^{0} d\tau\, \exp(\varepsilon\tau)\, U(\tau)^\dagger V\, U_0(\tau) \tag{A.27}$$

Introducing this formula in Eq. A.24, we let the free evolution operator act on the free state and we get

$$|\mathbf{p}+\rangle = |\mathbf{p}\rangle - \imath \lim_{\varepsilon\to 0^+} \int_{-\infty}^{0} d\tau \exp\left(-\imath(\imath\varepsilon - H + E_{\mathbf{p}})\tau\right) V\ |\mathbf{p}\rangle$$

In last expression, we can formally integrate and recognize Green's operator $G(E_{\mathbf{p}} + \imath 0^+)$

$$|\mathbf{p}+\rangle = |\mathbf{p}\alpha\rangle + G(E_{\mathbf{p}} + \imath 0^+)V\ |\mathbf{p}\rangle$$

that, by means of relations A.18 and A.26, becomes the Lippmann-Schwinger (LS) relation for the scattering states

$$|\mathbf{p}+\rangle = |\mathbf{p}\rangle + G_0(E_{\mathbf{p}} + \imath 0^+)V\ |\mathbf{p}+\rangle \tag{A.28}$$

We remark that the definition of the scattering states (and the corresponding LS equation) do not introduce any original element in the theory presented in previous sections. However, we can think the Lippmann-Schwinger equation as the representation of the operator equation in the most suitable basis, *i.e.* the free Hamiltonian eigenfunctions. In this sense, scattering states are a very convenient way to express a scattering problem.

A.4 Time dependent and time independent approach

The actual methodologies to study the time evolution of a system fall into two categories: time independent and time dependent methods.

The main idea of the *time independent* approach is to look for the scattering states $|p\alpha+\rangle$. As seen in previous section, scattering states are eigenfunctions of the complete Hamiltonian H and so they are solution of the time independent Schrödinger equation, with appropriate boundary conditions. These conditions are usually introduced by fixing the asymptotic behaviour of the scattering states, that can be computed from LS equation for the scattering states

$$\lim_{R\to\infty} \langle \mathbf{R} \,|\, p\alpha+\rangle = \langle \mathbf{R} \,|\, p\alpha\rangle + \lim_{R\to\infty} \langle \mathbf{R}| \, G_0(E_{p\alpha} + \imath 0^+) V \, |p\alpha+\rangle \tag{A.29}$$

In the *time dependent* approach, on the other hand, the actual time evolution of the system is considered by solving the time dependent Schrödinger equation with given initial conditions. In detail we take an initial wavepacket

$$|\Psi\rangle = \int d\mathbf{p}\psi(\mathbf{p}) \, |\mathbf{p}\alpha\rangle \tag{A.30}$$

By representing both the wavepacket and the evolution operator on a suitable basis, we evolve the wavepacket in time and then we analyse the results.

These two approaches are equivalent, as can be reasonably expected. Later we will prove this fact in a particular case, showing that with a the time-energy Fourier transform we can go from one description to the other.

A.5 Scattering of molecules on surfaces

In this section, we want to specify our consideration to a diatomic molecule scattering from a surface. The system can conveniently described by the 3D position of the center of mass of the particle $\mathbf{R} = (X, Y, Z)$ and by another nD coordinate $\mathbf{r} = (r, \theta, \phi, Q_1 \ldots)$, such that the Hamiltonian in $\mathbf{r}$ has only discrete eigenfunctions. In particular, $\mathbf{r}$ represents both the internal coordinate of the diatomic molecule and the phonon coordinates of the surface. Since we are assuming that the molecule cannot dissociate, the molecule Hamiltonian has just discrete states.

In particular, the Hamiltonian for the system will be

$$H = T(\mathbf{R}) + T(\mathbf{r}) + V_{asymp}(\mathbf{r}) + V_{coup}(\mathbf{r}, \mathbf{R}) \tag{A.31}$$

where we have conveniently split the potential in two terms. $V_{asymp}(\mathbf{r})$, which is the limit of the full potential as the molecule-surface distance becomes infinite, depends just on $\mathbf{r}$ and describe the vibrations of the free molecule and the phonon degrees of freedom. $V_{coup}(\mathbf{r}, \mathbf{R})$, the difference between the full potential and the asymptotic potential, describe the interaction of the molecule with the surface and the correlations between surface and molecule degrees of freedom. In the following, our free Hamiltonian will be $H^0 = T(\mathbf{R}) + T(\mathbf{r}) + V_{asymp}(\mathbf{r})$ and consequently $V = V_{coup}(\mathbf{r}, \mathbf{R})$.

A.5.1 Asymptotic limit of the scattering states

From LS equation (Eq. A.34), we can write the asymptotic state as

$$\langle \mathbf{R}\mathbf{r} \,|\, \mathbf{p}\alpha+ \rangle = \langle \mathbf{R}\mathbf{r} \,|\, \mathbf{p}\alpha \rangle + \langle \mathbf{R}\mathbf{r}| \, G_0(E_{\mathbf{p}\alpha} + \imath 0^+) V \, |\mathbf{p}\alpha+ \rangle \tag{A.32}$$

where $\mathbf{p} = (p_X, p_Y, -p_Z)$ is the momentum along $\mathbf{R}$ while $\alpha = (n, j, m_j, \nu_1 \ldots)$ is a collective discrete index labelling the bound state for the $\mathbf{r}$ wavefunction (*i.e.* the rovibrational state of the molecule and the phonon state of the surface). For future convenience, we choose the Z component of the momentum

to be $-p_Z$, so that p_Z is by definition a positive quantity when the incoming molecule approaches the surface. The free state energy $E_{\mathbf{p}\alpha}$ is

$$E_{\mathbf{p}\alpha} = \frac{p^2}{2M} + \epsilon_\alpha$$

with ϵ^α collecting all the energy term depending on the quantum numbers α.

We insert in LS equation the resolution of the identity on the free states

$$\langle \mathbf{R}\mathbf{r} \,|\, \mathbf{p}\alpha+\rangle = \langle \mathbf{R}\mathbf{r} \,|\, \mathbf{p}\alpha\rangle + \sum_\beta \int d\mathbf{p}' \, \langle \mathbf{R}\mathbf{r}| \, G_0(E_{\mathbf{p}\alpha} + \imath 0^+) \, |\mathbf{p}'\beta\rangle \, \langle \mathbf{p}'\beta| \, V \, |\mathbf{p}\alpha+\rangle$$

The periodicity of the the surface implies the invariance of the interaction potential V with respect to translations of $\rho = (X, Y)$. Both the free state $\langle \mathbf{p}\alpha|$ and the scattering states $\langle \mathbf{p}\alpha+|$ span the representation

$$exp(\imath \mathbf{p}^{\parallel} \cdot \tau_{ij})$$

of the lattice translations group $\{\tau_{ij}\}$ ($\mathbf{p}^{\parallel} = (p_X, p_Y)$ is the momentum component parallel to the surface). This implies that

$$\langle \mathbf{p}'\beta| \, V \, |\mathbf{p}\alpha+\rangle = 0$$

unless $p'_x - p_x = mk_1$ and $p'_y - p_y = nk_2$ (see Section 1.2.1). This allows us to convert the integration on ρ in a sum on m, n

$$\int d\mathbf{p}' \ldots \langle \mathbf{p}'\beta \,|\, V|\mathbf{p}\alpha+\rangle = \sum_{mn} \int dp'_z \ldots \left\langle p'_Z \mathbf{p}^{\parallel}_{mn}\beta \,\middle|\, V|\mathbf{p}\alpha+\right\rangle \tag{A.33}$$

where the vector $\mathbf{p}^{\parallel}_{mn}$ is the momentum $(p_X + nk_1,\, p_X + mk_2)$ parallel to the surface.

We can now evaluate the action of the free Green operator $G_0(E_{\mathbf{p}\alpha} + \imath 0^+)$ on the following free state using Eq. A.13

$$\langle \mathbf{R}\mathbf{r} \,|\, \mathbf{p}\alpha+\rangle = \langle \mathbf{R}\mathbf{r} \,|\, \mathbf{p}\alpha\rangle + \sum_{mn\beta} \lim_{\varepsilon\to 0^+} \int dp'_Z \frac{\left\langle \mathbf{R}\mathbf{r} \,\middle|\, p'_Z \mathbf{p}^{\parallel}_{mn}\beta\right\rangle \left\langle p'_Z \mathbf{p}^{\parallel}_{mn}\beta \,\middle|\, V|\mathbf{p}\alpha+\right\rangle}{E_{\mathbf{p}\alpha} - E_{\mathbf{p}'\beta} + \imath\varepsilon} \tag{A.34}$$

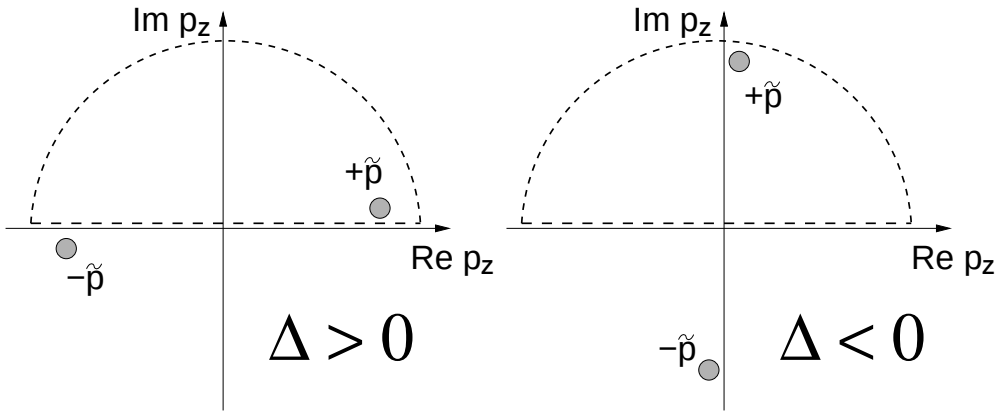

Figure A.1: Poles of the integrating function and path of integration

We want to evaluate the integral in p'_Z with the methods of complex analysis. The denominator of the fraction can be written as

$$E_{\mathbf{p}\alpha} - E_{\mathbf{p}'\beta} = E_{\mathbf{p}\alpha} - \frac{p_Z'^2 + p_{mn}^{\parallel 2}}{2M} - \epsilon^\beta = \frac{1}{2M}\left[\underbrace{2M\left(E_{\mathbf{p}\alpha} - \epsilon^\beta - \frac{p_{mn}^{\parallel 2}}{2M}\right)}_{\Delta} - p_Z'^2\right]$$

So we can factorize the denominator as

$$E_{\mathbf{p}\alpha} - E_{\mathbf{p}'\beta} + \imath\varepsilon = \frac{1}{2M}\left(\tilde{p} - p'_Z\right)\left(\tilde{p} + p'_Z\right)$$

where $\tilde{p}$ is one of the complex roots of $\Delta + \imath\varepsilon$ (for later convenience, we choose $\tilde{p}$ to be the root with $Im\,\tilde{p} > 0$).

To evaluate the integral, we extend the function in the complex plane, by taking $p'_Z \in \mathbb{C}$ and we consider the integration along the path schematically represented in Fig. A.1. In detail, the integration path is a line between $-R$ and $+R$ on the real axis, and half circumference of radius R in the upper complex half-plane. As $R \to +\infty$, the integral on the real axis becomes the integral we want to compute while the integral along the half circumference tends to 0. To prove that

$$\left|\frac{\left\langle \mathbf{Rr}\left| p'_Z\mathbf{p}_{mn}^{\parallel}\beta\right\rangle\left\langle p'_Z\mathbf{p}_{mn}^{\parallel}\beta\right| V|\mathbf{p}\alpha+\right\rangle}{\tilde{p}^2 - p_Z'^2}\right| \to 0 \quad \text{for } |p'_Z| \to +\infty$$

we have to show that for $p'_Z \in \mathbb{C}$ the modulus of the numerator is bounded. The absolute value of the first factor can be explicitly computed

$$\left|\left\langle \mathbf{R}\mathbf{r} \,\middle|\, p'_Z \mathbf{p}^{\parallel}_{mn}\beta \right\rangle\right| = \left|\frac{1}{\sqrt{2\pi A}}\phi_\beta(r)\right| e^{-\frac{1}{\hbar}(Im\, p'_Z)Z}$$

and is bounded if $Im\, p'_Z \geq 0$. The second factor can more conveniently considered in coordinate representation. If we again assume $Im\, p'_Z \geq 0$

$$\left|\left\langle p'_Z \mathbf{p}^{\parallel}_{mn}\beta \,\middle|\, V|\mathbf{p}\alpha+\right\rangle\right| = \left|\int d\mathbf{r}' \int d\mathbf{R}' \left\langle p'_Z \mathbf{p}^{\parallel}_{mn}\beta \,\middle|\, \mathbf{R}'\mathbf{r}'\right\rangle V(\mathbf{R}'\mathbf{r}') \left\langle \mathbf{R}'\mathbf{r}' \,\middle|\, \mathbf{p}\alpha+\right\rangle\right| \leq$$

$$\leq \left(\sup_{\mathbf{R}'\mathbf{r}'} V(\mathbf{R}'\mathbf{r}')\right) \left|\left\langle (Re\, p'_Z)\, \mathbf{p}^{\parallel}_{mn}\beta \,\middle|\, \mathbf{p}\alpha+\right\rangle\right|$$

Any reasonable potential can be assumed to be bounded except for some repulsive regions. Anyway the scattering eigenstates are eigenstates of the full Hamiltonian, and we can reasonably assume that in the repulsive regions they go to 0 faster than the potential itself.

From this analysis it becomes clear why we choose an integration path in the upper complex half-plane. If we chose the symmetric path in the lower half-plane, we couldn't assume $Im\, p'_Z \geq 0$ and the numerator of the integrand would no longer be bounded.

From the well known Cauchy's theorem of complex analysis, the integral along the closed path is $2\pi\imath$ times the sum of the residues of the integrand in the area contained in the integration path. In our case the integrand has just one simple pole in the upper half plane, namely $+\tilde{p}$. So

$$\int dp'_z \frac{f(p'_Z)}{(\tilde{p} - p'_Z)\,(\tilde{p} + p'_Z)} = 2\pi\imath \lim_{p'_z \to \tilde{p}} \frac{f(p'_Z)}{-(\tilde{p} + p'_Z)} = -\frac{\pi\imath f(\tilde{p})}{\tilde{p}}$$

In conclusion, Eq. A.34 becomes

$$\langle \mathbf{R}\mathbf{r} \,|\, \mathbf{p}\alpha+\rangle = \langle \mathbf{R}\mathbf{r} \,|\, \mathbf{p}\alpha\rangle - 2\imath\pi \sum_{mn\beta} \lim_{\varepsilon \to 0^+} \frac{M}{\tilde{p}} \left\langle \mathbf{R}\mathbf{r} \,\middle|\, \tilde{p}\mathbf{p}^{\parallel}_{mn}\beta \right\rangle \left\langle \tilde{p}\mathbf{p}^{\parallel}_{mn}\beta \,\middle|\, V|\mathbf{p}\alpha+\right\rangle \tag{A.35}$$

Next step is to take the limit $\varepsilon \to 0^+$. Now two possibilities arise, corresponding to the possible sign of Δ. For $\Delta < 0$ we have scattering channels

for which the energy $\epsilon^\beta + \frac{p_{mn}^{\parallel 2}}{2M}$ is greater than the initial energy (for reason that will become evident later, we call these *closed channels*). In this case the limit of $\tilde{p}$ for $\varepsilon \to 0^+$ is a purely imaginary momentum $\imath\bar{p}$ and the free eigenstates $\left\langle \mathbf{R}\mathbf{r} \,\middle|\, \tilde{p}\mathbf{p}_{mn}^{\parallel}\beta \right\rangle$ becomes

$$\left\langle \mathbf{R}\mathbf{r} \,\middle|\, \tilde{p}\mathbf{p}_{mn}^{\parallel}\beta \right\rangle = \frac{1}{\sqrt{2\pi A}} e^{-\frac{1}{\hbar}\bar{p}Z} e^{\frac{\imath}{\hbar}\mathbf{p}_{mn}^{\parallel}\cdot\rho}$$

This term contains a exponentially decaying function of Z. So, if we let $Z \to +\infty$, the closed channels do not contribute to the sum on Eq. A.35.

For the other channels $\Delta > 0$ and for $\varepsilon \to 0^+$, $\tilde{p}$ becomes a real positive momentum p'_Z and the free states survive in the limit $Z \to +\infty$. From a physical point of view, since $\bar{p}$ is the square root of $2M\left(E_{\mathbf{p}\alpha} - \epsilon^\beta - \frac{p_{mn}^{\parallel 2}}{2M}\right)$, p'_Z is the momentum along Z determined imposing energy conservation when the system goes from the state $|\mathbf{p}\alpha\rangle$ to a state with parallel momentum $p_{mn}^{\parallel}$ and quantum numbers β. The positive sign of p'_Z (meaning that the scattered molecules move far from the surface) is set by the choice of the integration path which in turn is connected to the presence of a repulsive wall for negative values of Z.

From Eq. A.26 we can recognize the matrix element of the T matrix

$$\left\langle \tilde{p}\mathbf{p}_{mn}^{\parallel}\beta \,\middle|\, V|\mathbf{p}\alpha+\right\rangle = \left\langle \tilde{p}\mathbf{p}_{mn}^{\parallel}\beta \,\middle|\, T|\mathbf{p}\alpha\right\rangle = t(\tilde{p}\mathbf{p}_{mn}^{\parallel}\beta \leftarrow \mathbf{p}\alpha)$$

In conclusion, the limit of the scattering states as $Z \to +\infty$

$$\langle \mathbf{R}\mathbf{r} \,|\, \mathbf{p}\alpha+\rangle \to \frac{1}{\sqrt{2\pi A}}\left[e^{\frac{\imath}{\hbar}\mathbf{p}\cdot\mathbf{R}}\phi_\alpha(\mathbf{r}) - 2\pi\imath\sum_{mn\beta}\frac{M}{p'_Z}e^{\frac{\imath}{\hbar}\mathbf{p}'\cdot\mathbf{R}}\phi_\beta(\mathbf{r})\, t(\mathbf{p}'\beta \leftarrow \mathbf{p}\alpha)\right] \tag{A.36}$$

where the components of the momentum $\mathbf{p}'$ parallel to the surface are constrained by symmetry

$$\begin{aligned} p'_X &= p_X + mk_1 \\ p'_Y &= p_Y + nk_2 \end{aligned} \tag{A.37}$$

and the component along Z is given from energy conservation

$$p'_Z = \left[2M\left(E_{\mathbf{p}\alpha} - \epsilon^\beta\right) - p_X'^2 - p_Y'^2\right]^{1/2} \tag{A.38}$$

A.5.2 Asymptotic flux and Cross Section

Now we will use the asymptotic expression of the scattering states to compute the cross section for the relevant events: elastic and inelastic scattering. The approach that we will follow is to compute the Z component of the flux along an analysis surface far from the interaction region. In such conditions, we can assume that the scattering states are equal to their asymptotic limit. We will find that the flux is a sum of different terms, each corresponding to a specific event.

The flux along a surface S can be computed as

$$\Phi = \frac{\hbar}{\mu} \int_S Im \left[\Psi^* \vec{\nabla} \Psi \right] \vec{\delta n} \tag{A.39}$$

where $\vec{\delta n}$ is the direction perpendicular to the surface [3]. In our case we compute the flux on a hyperplane $Z = Z_\infty$, that is located in the asymptotic region. The direction that is perpendicular to the surface lies along the $+Z$ direction. We allow X and Y to vary in one unit cell of the surface. The expression of the flux hence becomes

$$\Phi = \frac{\hbar}{\mu} \int d\mathbf{r} \int_0^{L_X} dX \int_0^{L_Y} dY \; Im \left(\Psi^* \partial_Z \Psi \right)|_{Z=Z_\infty}$$

By derivation and by taking the complex conjugate of the expression of the asymptotic limit of the scattering wavefunction (remember that $\mathbf{p} = (p_X, p_Y, -p_Z)$), we get

$$\langle \mathbf{Rr} \,|\, \partial_Z |\mathbf{p}\alpha+\rangle \rightarrow \frac{1}{\sqrt{2\pi A}} \left[\underbrace{-\frac{\imath}{\hbar} p_Z e^{\frac{\imath}{\hbar}\mathbf{p}\cdot\mathbf{R}} \phi_\alpha(\mathbf{r})}_{A1} + \underbrace{\frac{2\pi M}{\hbar} \sum_{mn\beta} e^{\frac{\imath}{\hbar}\mathbf{p}'\cdot\mathbf{R}} \phi_\beta(\mathbf{r}) \, t(\mathbf{p}'\beta \leftarrow \mathbf{p}\alpha)}_{A2} \right]$$

$$\langle \mathbf{Rr} \,|\, \mathbf{p}\alpha+\rangle^\star \rightarrow \frac{1}{\sqrt{2\pi A}} \left[\underbrace{e^{-\frac{\imath}{\hbar}\mathbf{p}\cdot\mathbf{R}} \phi^\star_\alpha(\mathbf{r})}_{B1} + \underbrace{2\pi\imath M \sum_{mn\beta} \frac{1}{p'_z} e^{-\frac{\imath}{\hbar}\mathbf{p}'\cdot\mathbf{R}} \phi^\star_\beta(\mathbf{r}) \, t^\star(\mathbf{p}'\beta \leftarrow \mathbf{p}\alpha)}_{B2} \right]$$

From the multiplication of these two expression, four terms arise. One term comes from the incident part of the scattering state ($A1 \times B1$), another term from the scattering part ($A2 \times B2$) while the other two ($A1 \times B2$ and $A2 \times B1$) represent the interference between the two waves. We take into account these three parts separately.

Incident Flux The first term $A1 \times B1$ is

$$-\frac{1}{2\pi A}\frac{\imath}{\hbar}p_Z e^{\imath \mathbf{p}\cdot\mathbf{R}}\phi_\alpha(\mathbf{r})e^{-\imath \mathbf{p}\cdot\mathbf{R}}\phi_\alpha^\star(\mathbf{r}) = -\frac{\imath p_Z}{2\pi\hbar A}\left|\phi_\alpha(\mathbf{r})\right|^2$$

and the flux coming from this term is

$$\Phi_{inc} = -\frac{1}{2\pi}\frac{p_Z}{M} \tag{A.40}$$

which can evidently be associated with an incident beam of particle with velocity $\frac{p_Z}{M}$ approaching the surface (p_Z is positive by definition so the flux is negative)

Scattering flux The term $A2 \times B2$ is

$$\frac{2\pi\imath}{\hbar}\sum_{kl\gamma}\sum_{mn\beta}\frac{M^2}{Ap'_Z}e^{\frac{\imath}{\hbar}(\mathbf{p}''-\mathbf{p}')\cdot\mathbf{R}}\phi_\gamma(\mathbf{r})\phi_\beta^\star(\mathbf{r})\, t(\mathbf{p}''\gamma \leftarrow \mathbf{p}\alpha)t^\star(\mathbf{p}'\beta \leftarrow \mathbf{p}\alpha)$$

The symmetry condition on $\mathbf{p}'$ (Eq. A.37) implies that

$$\frac{1}{A}\int_0^{L_X} dX \int_0^{L_Y} dY\, e^{\frac{\imath}{\hbar}(\mathbf{p}''-\mathbf{p}')\cdot\mathbf{R}} = e^{\frac{\imath}{\hbar}(p''_Z-p'_Z)Z}\delta_{mk}\delta_{nl}$$

while the orthonormality of the discrete states implies

$$\int d\mathbf{r}\,\phi_\gamma(\mathbf{r})\phi_\beta^\star(\mathbf{r}) = \delta_{\gamma\beta}$$

Hence the integration gives

$$\frac{2\pi\imath}{\hbar}\sum_{kl\gamma}\sum_{mn\beta}\delta_{mk}\delta_{nl}\delta_{\gamma\beta}\frac{M^2}{p'_Z}e^{\frac{\imath}{\hbar}(p''_Z-p'_Z)Z}\, t(\mathbf{p}''\gamma \leftarrow \mathbf{p}\alpha)t^\star(\mathbf{p}'\beta \leftarrow \mathbf{p}\alpha) =$$

$$= \frac{2\pi\imath}{\hbar}\sum_{mn\beta}\frac{M^2}{p'_Z}\left|t(\mathbf{p}'\beta \leftarrow \mathbf{p}\alpha)\right|^2$$

recognizing that if $m = k$, $n = l$ and $\gamma = \beta$ then $p''_Z = p'_Z$ (since both values are constrained by conservation of energy).

In conclusion the flux is

$$\Phi_{scattering} = 2\pi \sum_{mn\beta} \frac{M}{p'_Z} \left| t(\mathbf{p}'\beta \leftarrow \mathbf{p}\alpha) \right|^2 \tag{A.41}$$

which represents the scattering of particles in all the channels that are consistent with energy conservation. Each scattering event has a probability which is given by the square of the on shell T matrix, as expected from the theory.

Interference flux The term $A1 \times B2$ is

$$+\frac{M}{\hbar} \sum_{mn\beta} \frac{p_Z}{p'_Z} \frac{1}{A} e^{\frac{i}{\hbar}(\mathbf{p}-\mathbf{p}')\cdot\mathbf{R}} \left(\phi^\star_\beta(\mathbf{r}) \phi_\alpha(\mathbf{r}) \right) \; t^\star(\mathbf{p}'\beta \leftarrow \mathbf{p}\alpha)$$

while the term $A2 \times B1$

$$+\frac{M}{\hbar} \sum_{mn\beta} \frac{1}{A} e^{\frac{i}{\hbar}(\mathbf{p}'-\mathbf{p})\cdot\mathbf{R}} \left(\phi^\star_\alpha(\mathbf{r}) \phi_\beta(\mathbf{r}) \right) \; t(\mathbf{p}'\beta \leftarrow \mathbf{p}\alpha)$$

By integration we find that

$$\Phi_{interf} = \frac{M}{\hbar} Im \left(t^\star(-p_Z \mathbf{p}^\parallel \alpha \leftarrow \mathbf{p}\alpha) + t(-p_Z \mathbf{p}^\parallel \alpha \leftarrow \mathbf{p}\alpha) \right) = 0 \tag{A.42}$$

the interference term is equal to zero[2].

[2]For the reader who is familiar with scattering theory, some comments are appropriate. The method that we have applied here is often used to derive results that may seems to be in disagreement with our discussion. In particular, in other context the interference is different from zero and applying flux conservation this term depending on the forward scattering T matrix element can be shown to be related to total scattering cross section (the well known *optical theorem*).

In our case, even if the flux method is the same, some crucial assumptions of the derivation mentioned above do not hold. In detail:

- our asymptotic expansion of the scattering states does not contain a forward scattering term interfering with the incoming wave. The boundary conditions of the problem forced us to choose the specular channel $(-p_Z \mathbf{p}^\parallel \alpha \leftarrow \mathbf{p}\alpha)$ rather than the forward channel $(p_Z \mathbf{p}^\parallel \alpha \leftarrow \mathbf{p}\alpha)$ in the integration of the interference term
- as a consequence of Gauss theorem, flux conservation holds for closed surface in the coordinate space. The choice of the hypersurface S that is convenient for the symmetry of our system does not allow to apply flux conservation

Scattering cross sections In conclusion, the total flux is

$$\Phi_{total} = \Phi_{incident} + \sum_{mn\beta} \Phi^{mn\beta}_{scattering} \tag{A.43}$$

We can calculate the cross section for the scattering in each open channel as

$$\frac{\partial \sigma}{\partial \rho}(\mathbf{p}'\beta \leftarrow \mathbf{p}\alpha) = \frac{\Phi^{mn\beta}_{scattering}}{\Phi_{incident}}$$

which gives

$$\frac{\partial \sigma}{\partial \rho}(\mathbf{p}'\beta \leftarrow \mathbf{p}\alpha) = 4\pi^2 \frac{M^2}{p_Z p'_Z} \left| t(\mathbf{p}'\beta \leftarrow \mathbf{p}\alpha) \right|^2 \tag{A.44}$$

In light of this result, we can define a new scattering matrix element - which is more convenient for the boundary condition of our specific problem. In terms of the on-shell T matrix, the new $\tilde{S}$ is defined as

$$\tilde{S}(\mathbf{p}'\beta \leftarrow \mathbf{p}\alpha) = 2\pi\imath \frac{M}{\sqrt{p_Z p'_Z}}\, t(\mathbf{p}'\beta \leftarrow \mathbf{p}\alpha) \tag{A.45}$$

so that the square of its matrix element is the cross section for the specific scattering event considered.

With these definition the asymptotic formula for the scattering states becomes

$$\langle \mathbf{R}\mathbf{r} \,|\, \mathbf{p}\alpha + \rangle \rightarrow \frac{1}{\sqrt{2\pi A}} \left[e^{\frac{\imath}{\hbar}\mathbf{p}\cdot\mathbf{R}} \phi_\alpha(\mathbf{r}) - \sum_{mn\beta} \sqrt{\frac{p_Z}{p'_Z}} e^{\frac{\imath}{\hbar}\mathbf{p}'\cdot\mathbf{R}} \phi_\beta(\mathbf{r})\, \tilde{S}(\mathbf{p}'\beta \leftarrow \mathbf{p}\alpha) \right] \tag{A.46}$$

A.5.3 Time-Energy Fourier Transform of a wavepacket

In section A.4 we have briefly mentioned that time dependent and time independent pictures can be related by a time-energy Fourier transform. We will show now for the scattering of molecules on surfaces how this can be done, by extracting information about the scattering states from the actual evolution of the system.

Let's consider a wavepacket, with definite α, $\mathbf{p}_{||}$ and a distribution $\psi(p_Z)$ on p_Z. Its free evolution, in absence of the molecule-surface interaction, will be given by

$$|\Psi\rangle = e^{-\imath H_0 t} \int dp_Z \psi(p_Z) \, |\mathbf{p}\alpha\rangle = \int dp_Z \psi(p_Z) e^{-\imath H_0 t} \, |\mathbf{p}\alpha\rangle \tag{A.47}$$

where H_0 is the Hamiltonian including the internal degrees of freedom of both the molecule and the surface. On the other hand, the actual evolution of the wavepacket will be given by

$$|\Psi+\rangle = \Omega_+ \int dp_Z \psi(p_Z) e^{-\imath H_0 t} \, |\mathbf{p}\alpha\rangle = \int dp_Z \psi(p_Z) e^{-\imath H t} \, |\mathbf{p}\alpha+\rangle \tag{A.48}$$

where we have used the intertwining relation Eq. A.9.

Fourier transforming the wavepacket for fixed E, we get

$$\int_{-\infty}^{+\infty} dt \, e^{\imath E t} \, |\Psi+\rangle = \int dp_Z \psi(p_Z) \int_{-\infty}^{+\infty} dt \, e^{\imath (E-H) t} \, |\mathbf{p}\alpha+\rangle \tag{A.49}$$

Since the scattering states are stationary, we can integrate on time

$$\int_{-\infty}^{+\infty} dt \, e^{\imath (E-H) t} = 2\pi \delta(E - H)$$

where $\delta(E-H)$ is the projector on the energy shell. If we let the projector act on the scattering state $|\mathbf{p}\alpha+\rangle$ we have the Dirac delta

$$\delta\left(E - \frac{p_{\|}^2}{2M} - \epsilon_\alpha - \frac{p_Z^2}{2M}\right) = 2M\delta\left(\Delta - p_Z^2\right)$$

where $\mathbf{p}_{||}$ and ϵ_α are respectively the parallel momentum and the internal energy of the initial wavepacket, and Δ is equal to $2M\left(E - \epsilon_\alpha - \frac{p_{\|}^2}{2M}\right)$. Now we have to possibilities. If the energy E we are considering is lower than than $\epsilon_\alpha + \frac{p_{\|}^2}{2M}$, Δ is a negative number, and the integral on p_Z is zero. On the other hand, for $\Delta > 0$ we set $\bar{p} = \sqrt{\Delta}$ and we can transform the Dirac delta as

$$2M\delta\left(\bar{p}^2 - p_Z^2\right) = \frac{M}{\bar{p}}\left[\delta\left(p_z - \bar{p}\right) + \delta\left(p_z + \bar{p}\right)\right]$$

Eq. A.49 becomes

$$\int_{-\infty}^{+\infty} dt\, e^{\imath Et} \left|\Psi+\right\rangle = \frac{2\pi M}{\bar{p}} \left[\psi(\bar{p}) \left|\bar{p}\mathbf{p}_{\|}\alpha+\right\rangle + \psi(-\bar{p}) \left|(-\bar{p})\,\mathbf{p}_{\|}\alpha+\right\rangle\right]$$

$$\text{with } \bar{p} = \sqrt{2M\left(E-\epsilon_{\alpha}\right) - p_{\|}^2}$$

If we choose an initial momentum distribution $\psi(p_Z)$ which is narrow and centered in negative p_Z values (the particle is moving towards the surface), we can assume $\psi(\bar{p}) \approx 0$ and

$$\int_{-\infty}^{+\infty} dt\, e^{\imath Et} \left|\Psi+\right\rangle = \frac{2\pi M}{\bar{p}} \psi(-\bar{p}) \left|(-\bar{p})\,\mathbf{p}_{\|}\alpha+\right\rangle$$

In conclusion, by computing the Fourier transform for different values of E, we can selectively extract from the evolving wavepacket information on $\left|\mathbf{p}\alpha+\right\rangle$

$$\left|\mathbf{p}\alpha+\right\rangle = \frac{|p_Z|}{2\pi M\psi(p_Z)} \int_{-\infty}^{+\infty} dt\, \exp(\frac{\imath}{\hbar}Et) \left|\Psi+\right\rangle \qquad E = \epsilon_{\alpha} + \frac{p_{\|}^2}{2M} + \frac{p_Z^2}{2M} \tag{A.50}$$

As evident from this formula, we can get information on the scattering event just for the internal state α, the parallel momentum $\mathbf{p}_{||}$ and the values of incident momentum p_Z included in the initial wavepacket.

Bibliography

[1] J. Taylor, *Scattering Theory: The Quantum Theory of Nonrelativistic Collisions*, Dover Books on Engineering Series, Dover Publications (2006).

[2] R. Newton, *Scattering theory of waves and particles*, Dover books on physics, Dover Publications (2002).

[3] A. Messiah, *Quantum mechanics*, Dover books on physics, Dover Publications (1999).

Appendix B

Vibrational Sudden Approximation

The Vibrational Sudden Approximation (VSA) is a particular sudden approximation that has been developed in gas-phase scattering dynamics by Bowman [1, 2]. For those problems that present a high mass mismatch between the scattering molecule and the surface atoms (such as H_2 on Cu surfaces), we expect this approximation to be particularly suitable. Indeed, similar approaches have been followed successfully in scattering systems such as H_2 on Pd(111) [3] or methane in Ni(111) and Pt(111) [4, 5].

In this appendix, the VSA approach is presented and discussed for a simple model system, and then generalized to a gas-surface scattering problem.

B.1 A simple model in time-independent picture

Following the approach of Ref. [2], we consider a very simple two dimensional model: the linear collision of an atom and a diatomic molecule.

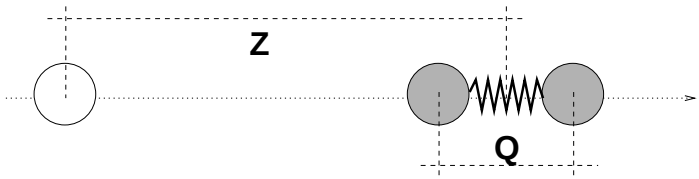

With a simple linear transformation of the coordinate Z (the distance between the incident atom and the center of mass of the molecule) and of the coordinate Q (the internal degree of freedom of the molecule) we can define the dimensionless mass scaled coordinates z and q such that the Hamiltonian of the system is

$$H(z,q) = -\frac{1}{2}\partial_z^2 - \frac{1}{2}\partial_q^2 + V_{vibr}(q) + V_{scatt}(z,q) \tag{B.1}$$

where V_{vibr} is the potential for the vibrations of the diatomic molecule and V_{scatt} is the atom-molecule interaction.

When the atom is far from the molecule ($z \to \infty$), V_{scatt} is negligible and a convenient set of eigenstates for this system is made of the product functions

$$\langle zq \,|\, np\rangle = \chi_n(q)\,\vartheta_p(z) \qquad\qquad n = 0, 1... \quad p \in [-\infty; +\infty] \tag{B.2}$$

where $\vartheta_p(z) = e^{ipz}$ is a plane wave of momentum p and $\chi_n(q)$ is the n-th eigenfunction of the one dimensional molecular Hamiltonian

$$\left(-\frac{1}{2}\partial_q^2 + V_{vibr}(q)\right)\chi_n(q) = E_n\,\chi_n(q) \tag{B.3}$$

Let's consider the scattering states for our model system

$$|np\pm\rangle = \Omega_\pm\,|np\rangle \tag{B.4}$$

These states represent an atom with momentum p that collide with a molecule in the n-th vibrational state. Without any approximation, we can write the scattering states as the product

$$\langle zq \,|\, np\pm\rangle = \chi_n(q)\varphi^\pm_{np}(z,q) \tag{B.5}$$

Since the scattering event couples different vibrational states of the target molecule, $\langle zq \,|\, np\pm\rangle$ is not a simple product state, and the function φ_{np} still depends on q.

The Vibrational Sudden Approximation consists in assuming that the function $\varphi_{np}(z,q)$ is a slowly varying function of the vibrational coordinate q, *i.e.*

$$\frac{\partial^2}{\partial q^2}\left[\chi_n(q)\varphi^\pm_{np}(z,q)\right] \approx \varphi^\pm_{np}(z,q)\,\partial_q^2\chi_n(q) \tag{B.6}$$

The physical meaning of this assumption will be discussed later, from a time dependent point of view. Now we want to derive an equation to compute $\varphi^{\pm}_{np}(z,q)$. The scattering states are eigenfunctions of the Hamiltonian operator

$$\left(-\frac{1}{2}\partial_z^2 - \frac{1}{2}\partial_q^2 + V_{vibr}(q) + V_{scatt}(z,q) - \left(E_n + \frac{p^2}{2}\right)\right)\chi_n(q)\varphi^{\pm}_{np}(z,q) = 0 \tag{B.7}$$

Applying the VSA approximation we get

$$\left(-\frac{1}{2}\partial_z^2 + E_n + V_{scatt}(z,q) - \left(E_n + \frac{p^2}{2}\right)\right)\varphi^{\pm}_{np}(z,q) = 0$$

$$\left(-\frac{1}{2}\partial_z^2 + V_{scatt}(z,q) - \frac{p^2}{2}\right)\varphi^{\pm}_{np}(z,q) = 0 \tag{B.8}$$

This part of the scattering wavefunction is just a solution of a simpler one dimensional problem, in which the scattering potential depends parametrically on q. We define the VSA Hamiltonian as the the Hamiltonian of this lower dimensional system

$$H_{\mathrm{VSA}}(q,z) = -\frac{1}{2}\partial_z^2 + V_{scatt}(z,q) \tag{B.9}$$

The VSA Hamiltonian is a family of one dimensional system, in which the solution is parametrically dependent of the coordinate q. Hence, instead of dealing with a single two dimensional problem, we now can solve an infinite number of simpler one dimensional problems with potential $V^q(z) = V_{scatt}(z,q)$.

In the following we will use the semicolon to point out that the dependence on q is parametric. From the same equation, we can see that the solution is independent on the vibrational state n. From now on we will drop the n label from the wavefunction. In conclusion, the scattering state in the VSA is

$$\langle zq \,|\, np\pm\rangle = \chi_n(q)\varphi^{\pm}_p(z;q) \tag{B.10}$$

Consequently, the scattering matrix can be written as

$$S(pn \leftarrow p'm) = \langle pn- \,|\, mp'+\rangle =$$

$$= \int dq \int dz \left(\chi_n(q)\varphi_p^-(z;q)\right)^\star \left(\chi_m(q)\varphi_{p'}^+(z;q)\right) =$$
$$= \int dq\, \chi_n^\star(q) \left[\int dz \left(\varphi_p^-(z;q)\right)^\star \varphi_{p'}^+(z;q)\right] \chi_m(q)$$

In square parentheses, we can recognize the q dependent S matrix for the scattering problem corresponding to the VSA Hamiltonian

$$S(pn \leftarrow p'm) = \int dq\, \chi_n^\star(q)\, S^{\mathrm{VSA}}(p \leftarrow p'; q)\, \chi_m(q) \tag{B.11}$$

B.2 Validity of VSA

To understand what are the implications of the VSA from a dynamical point of view, let's analyze the assumption of Eq. (B.6) from a different point of view.

Let's consider a wavefunction $\chi_n(q)\varphi(z)$ that evolves in time according to the full Hamiltonian of Eq. (B.1)

$$\psi(q,z,t) = U_t\, \chi_i(q)\varphi(z) \tag{B.12}$$

The VSA consists in assuming that the coupling potential commutes with the vibrational Hamiltonian $H_q = -\frac{1}{2}\frac{\partial^2}{\partial q^2} + V_{vibr}(q)$

$$\left[H_q\,,\, V_{scatt}\right] \approx 0 \tag{B.13}$$

Under such assumption the vibrational Hamiltonian commutes with the VSA Hamiltonian and the evolution operator can be split according to

$$U_t = \exp(-\imath H t) \approx \exp(-\imath H_{\mathrm{VSA}} t)\exp(-\imath H_q t) \tag{B.14}$$

Hence the evolving state becomes

$$\psi(q,z,t) = \exp\left(-\imath E_{vib}^i t\right)\left[\exp\left(-\imath H_{\mathrm{VSA}} t\right)\varphi(z)\,\chi_i(q)\right] \tag{B.15}$$

Except for the phase factor $\exp\left(-\imath E_{vib}^i t\right)$, Eq. B.15 represents a state evolving according to the VSA Hamiltonian. Note that this is different from assuming that the scattering and the vibrational coordinates are decoupled. In fact,

the final evolved state of Eq. (B.15) is not separable in two functions, because the propagator $\exp(-\imath H_{\mathrm{VSA}} t)$ still depends on q.

Now we can examine the assumption of Eq. (B.13) with greater detail. The part of H_q which does not commute with the coupling potential is the kinetic energy part, since multiplicative operators always commute. Explicitly, the commutation relation can be written as

$$\partial_q^2 V_{scatt}(z,q)\,\psi(q,z) \approx V_{scatt}(z,q)\,\partial_q^2\psi(q,z) \tag{B.16}$$

which means that the coupling potential is a slowly varying function of q with respect to the vibrational eigenstates. By applying the derivation rule, we find that the commutator is proportional to

$$\left[H_q\,,\,V_{scatt}\right]\psi(q,z) \sim \left(\partial_q^2 V_{scatt}(z,q)\right)\,\psi(q,z) + 2\left(\partial_q V_{scatt}(z,q)\right)\,\left(\partial_q\psi(q,z)\right)$$

For small displacement of the vibrational coordinate, we can further assume the coupling potential to be a linear function of q

$$V_{scatt} = \kappa q\, f(z)$$

The commutator then becomes

$$\left[H_q\,,\,V_{scatt}\right]\psi(q,z) \sim 2\kappa\, f(z)\,\left(\partial_q\psi(q,z)\right) \tag{B.17}$$

In conclusion, for each (q,z) point, the Vibrational Sudden Approximation is satisfied if

1. the "local" velocity of the oscillator is small (compared to the momentum on the scattering degree of freedom)

$$\partial_q\psi(q,z) \approx 0 \tag{B.18}$$

2. the coupling coefficient is small (compared to the total potential of the system)

$$\kappa\, f(z) \approx 0 \tag{B.19}$$

B.3 VSA in molecular scattering

Now we can turn our attention to the scattering of molecules on surface. If we consider the six degree of freedom of a diatomic molecule and one additional vibrational degree of freedom for the surface, the Hamiltonian can be written as

$$H = -\frac{1}{2M}\nabla^2_{\mathbf{R}} - \frac{1}{2M}\nabla^2_{\mathbf{r}} - \frac{1}{2\mu}\partial^2_Q + V_{6D}(\mathbf{R},\mathbf{r}) + V_{coupling}(\mathbf{R},\mathbf{r},Q) + V_{vib}(Q) \tag{B.20}$$

We have split the total 7D potential in three terms: V_{6D} is the interaction of the molecule with the static equilibrium surface, V_{vibr} is the vibrational potential for the surface degree of freedom and $V_{coupling}$ is the coupling between the molecule and the surface degrees of freedom.

We can apply the Vibrational Sudden Approximation to the vibrational degree of freedom of the surface:

$$\left[-\frac{1}{2\mu}\partial^2_Q + V_{vib}\,,\, V_{coupling}\right] \approx 0 \tag{B.21}$$

The VSA Hamiltonian will be

$$H_{\mathrm{VSA}}(\mathbf{R},\mathbf{r};Q) = -\frac{1}{2M}\nabla^2_{\mathbf{R}} - \frac{1}{2M}\nabla^2_{\mathbf{r}} + V_{6D}(\mathbf{R},\mathbf{r}) + V_{coupling}(\mathbf{R},\mathbf{r},Q) \tag{B.22}$$

As in the case of the simple two dimensional problem, this Hamiltonian is a scattering problem with one less degree of freedom and parametrically dependent on the vibrational coordinate Q. The VSA scattering matrix will be

$$S^{\mathrm{VSA}}(\mathbf{f} \leftarrow \mathbf{i}; Q)$$

where the indices i and f labels the initial and final state of the scattered molecule[1]. Labelling the initial and final vibrational state of the surface with μ and μ', the 7D scattering matrix in the VSA is given by

$$S(\mathbf{f}\,\mu' \leftarrow \mathbf{i}\,\mu) = \int dQ\, \chi^\star_{\mu'}(Q)\, S^{\mathrm{VSA}}(\mathbf{f} \leftarrow \mathbf{i}; Q)\, \chi_\mu(Q) \tag{B.23}$$

[1]In detail, $\mathbf{i}$ will identify the initial momentum $\mathbf{p}$ and the initial rovibrational state of the molecule $v\, j\, m_j$. The final index $\mathbf{f}$ will specify the quantum numbers of the diffraction channel $n_X\, n_Y$ and the rovibrational state of scattered molecule $v'\, j'\, m'_j$. The final momentum along Z is fixed by energy conservation.

where $\chi_\mu(Q)$ and $\chi_{\mu'}(Q)$ are two eigenfunctions of the vibrational Hamiltonian

$$H_{vib} = -\frac{1}{2\mu}\partial_Q^2 + V_{vib}(Q) \tag{B.24}$$

The scattering probability, summed over the final vibrational state of the surface is

$$P_{scatter}(\mathbf{f} \leftarrow \mathbf{i}\,\mu) = \sum_{\mu'} \left|S(\mathbf{f}\,\mu' \leftarrow \mathbf{i}\,\mu)\right|^2$$

In this formula, we can substitute the expression of the scattering matrix in the VSA, Eq. B.23, and get

$$\sum_{\mu'} \left|S(\mathbf{f}\,\mu' \leftarrow \mathbf{i}\,\mu)\right|^2 = \sum_{\mu'} S^\star(\mathbf{f}\,\mu' \leftarrow \mathbf{i}\,\mu) S(\mathbf{f}\,\mu' \leftarrow \mathbf{i}\,\mu) =$$

$$\int dQ \int dQ' \sum_{\mu'} \chi_{\mu'}(Q)\chi^\star_{\mu'}(Q') \left(S^{\mathrm{VSA}}(\mathbf{f} \leftarrow \mathbf{i}; Q)\right)^\star S^{\mathrm{VSA}}(\mathbf{f} \leftarrow \mathbf{i}; Q')\, \chi^\star_\mu(Q)\chi_\mu(Q')$$

From the completeness of the vibrational states $\chi_{\mu'}$

$$\sum_{\mu'} \chi_{\mu'}(Q)\chi^\star_{\mu'}(Q') = \delta(Q - Q')$$

In conclusion, the (molecule) state resolved reaction probability is given by the average of the VSA scattering probability, with a weight which is given by the square of the initial vibrational eigenfunction

$$P_{scatter}(\mathbf{f}\,\mu' \leftarrow \mathbf{i}\,\mu) = \int dQ \left|S^{\mathrm{VSA}}(\mathbf{f} \leftarrow \mathbf{i}; Q)\chi_\mu(Q)\right|^2 \tag{B.25}$$

Note that with a knowledge of $S^{\mathrm{VSA}}(\mathbf{f} \leftarrow \mathbf{i}; Q)$, the scattering probability can be computed for any initial state just by changing the vibrational eigenstate in the integral. From a practical point of view, we can use this equation by computing the VSA scattering matrix on a suitable grid $\{Q_n\}$ and by performing the integration with

$$P_{scatter}(\mathbf{f} \leftarrow \mathbf{i}\,\mu) = \sum_n \left|S^{\mathrm{VSA}}(\mathbf{f} \leftarrow \mathbf{i}; Q_n)\chi_\mu(Q_n)\right|^2 w_n \tag{B.26}$$

where the coefficients w_n are the weights of the quadrature rule.

From the state resolved scattering probability, the dissociative adsorption probability can be computed by

$$P_{react}(\mathbf{i}, \mu) = 1 - \sum_{\mathbf{f}} P_{scatter}(\mathbf{f} \leftarrow \mathbf{i}\, \mu)$$

The reaction probability then becomes

$$P_{react}(\mathbf{i}, \mu) = 1 - \int dQ \left|\chi_\mu(Q)\right|^2 \sum_{\mathbf{f}} \left|S^{\mathrm{VSA}}(\mathbf{f} \leftarrow \mathbf{i}; Q)\right|^2 =$$

$$= 1 - \int dQ \left|\chi_\mu(Q)\right|^2 \left(1 - P^{VSA}_{react}(\mathbf{i}, Q)\right) = \int dQ \left|\chi_\mu(Q)\right|^2 P^{VSA}_{react}(\mathbf{i}, Q)$$

As for the scattering probability, the reaction probability can be computed simply averaging the reaction probability with weights equal to the square of the initial vibrational eigenfunction. In the last formula the reaction probability depends on the vibrational state of the surface. If we assume the surface to be in thermal equilibrium at temperature T, we can average the reaction probability with a Boltzmann distribution

$$P_{react}(\mathbf{i}, T) = \sum_{\mu} \exp(\frac{E_\mu}{kT})\, P_{react}(\mathbf{i}\, \mu) = \sum_{\mu} \int dQ\, \exp(\frac{E_\mu}{kT}) \left|\chi_\mu(Q)\right|^2 P^{VSA}_{react}(\mathbf{i}, Q) \tag{B.27}$$

Bibliography

[1] J. M. Bowman, *International Journal of Quantum Chemistry* **16**, 487 (1979).

[2] J. M. Bowman, G. Drolshagen and J. P. Toennies, *J. Chem. Phys.* **71**, 2270 (1979).

[3] R. A. Olsen, G.-J. Kroes, O. M. Løvvik and E. J. Baerends, *J. Chem. Phys.* **107**, 10652 (1997).

[4] A. K. Tiwari, S. Nave and B. Jackson, *Phys. Rev. Lett.* **103**, 253201 (2009).

[5] A. K. Tiwari, S. Nave and B. Jackson, *J. Chem. Phys.* **132**, 134702 (2010).